Analysis of Performance Limiting Factors in H_2-O_2 Alkaline Membrane Fuel Cell

Von der Fakultät für Maschinenbau der Technischen Universität Braunschweig

zur Erlangung der Würde

eines Doktor-Ingenieurs (Dr.-Ing.)

genehmigte Dissertation

von: Prashant Subhas Khadke
geb. am 04. Februar 1984 in Sriganganagar, Rajasthan, Indien

eingereicht am: 12.11. 2015
mündliche Prüfung am: 25.02.2016

Gutachter: Prof. Dr.-Ing. Ulrike Krewer

Prof. Dario R. Dekel

2016

Acknowledgement

Sincere thanks to my supervisor Prof. Dr. Ulrike Krewer for giving me the opportunity to carry out PhD work in her group. Her valuable suggestions, guidance and support for completion of my thesis are greatly appreciated. I would also like to thank her for painstakingly reviewing my work from time to time and for being honest and critical which has substantially improved my quality of work over a course of PhD. I would also like to thank her for strengthening my personal skills by creating opportunities to work on other projects with several co-operation partners from other institutes.

I would like to thank Christine Weinzierl, Youngseung Na, Dr. Daniel Schröder, Dr. Maik Kraus and Dr. Qing Mao for creating a very friendly atmosphere and for the interesting scientific and non-scientific discussions. It was a great pleasure to work with you all guys. I would like to thank my Indian friends at Max Planck Institute Magdeburg who were always very friendly and helpful to answer my questions about life in Germany.

I take this opportunity to thank the mechanical workshop team, the electrical workshop team, Markus Ikert and Bianka Stein for their help during my work at Max Planck Institute Magdeburg.

I would like to thank Madhu Singh, Gazi Abul Mansur Ahamed, Irshad Rana Muhammad, Robert Miersch and Miguel MoIina Garcia for their assistance in carrying out some of the experiments.

At Institute of Energy and Process Systems Engineering, TU Braunschweig, I would like to thank Nina Böge for providing assistance in carrying out some experiments and promptly procuring materials that I required for the experiments. I thank Wilfried Janßen and Uwe Herrmann for building many experimental set-ups which enabled me to finish my work on time. I would like to thank Ina Schunke and Dr. Horst Müller for their help in the administrative tasks. I extend my thanks to other colleagues and staff members of Institute of Energy and Process Systems Engineering, TU Braunschweig.

I would like to thank my co-operation partners Dr, Martin Müller, Dr. Andreas Glüsen and Nicola Kimiaie from Forschungszentrum Jülich; Prof. Dr. Michael Bron and Dr. Abu Bakr Ahmed Amine Nassr from Martin Luther University, Halle-Wittenberg; Dr. Tobias Arlt from Helmholtz Zentrum Berlin; and Prof. Dr. Markus Antonietti and Servann Hérou from Max Planck Institute Potsdam. It was a good experience to work with you all.

Finally and most importantly I would like to thank my wife for her love, kindness and support for my emotional well-being throughout the duration of PhD. I would also like to thank her for many scientific discussions and invaluable suggestions during thesis writing.

Prashant Subhas Khadke
Braunschweig, 12.11.2015

Contents

List of Symbols & Abbreviations

Abbreviations

AEI	Anion exchange ionomer
AEM	Anion exchange membrane
AFCs	Alkaline fuel cells
AMFC	Alkaline membrane fuel cell
CE	Counter electrode
CL	Catalyst layer
cs	Chemical step
cts	Charge transfer step
CV	Cyclic voltammetry
ECSA	Electrochemical surface area
GC	Glassy carbon
GDL	Gas diffusion layer
HOR	Hydrogen oxidation reaction
IL-MEA	Inert layer – Membrane electrode assembly
LSV	Linear sweep voltammetry
MEA	Membrane electrode assembly
MMO	Mercury mercury oxide
OCP	Open circuit potential
ORR	Oxygen reduction reaction
PEMFC	Proton exchange membrane fuel cell
RDE	Rotating disk electrode
rds	Rate determining step
RE	Reference electrode
Ref-MEA	Reference – Membrane electrode assembly
RH	Relative humidity
rpm	Rotations per minute
SHE	Standard hydrogen electrode
WE	Working electrode

Symbols

A	Geometric area
A'	Effective diffusion area
a_i	Activity of species i at the electrode surface
C_B	Bulk concentration / solubility of the reactant in the electrolyte
C_d	Charge double layer capacitance
C_f	Concentration of reactant/O_2 inside the film at film-liquid interface
C_{g,O_2}	Concentration of O_2 in the gaseous phase
C_{H_2}	Concentration of hydrogen
C_{H_2O}	Concentration of water
C_i	Concentration of reactant/O_2 in liquid side at film-liquid interface
C_O	Surface concentration of oxidant
C_{O_2}	Concentration of O_2
C_{l,O_2}	Concentration of O_2 in the liquid phase
C_R	Surface concentration of reductant
C_0	Concentration at x = 0 from electrode

D	Diffusion coefficient of the reactant in the electrolyte
D_f	Diffusion coefficient of the reactant through film
D_{A-B}	Diffusion coefficient of A in medium B
D_{GDL,H_2}	Diffusion coefficient of H_2 through GDL
D_{GDL,H_2O}	Diffusion coefficient of H_2O through GDL
D_{GDL,O_2}	Diffusion coefficient of O_2 through GDL
D_{H_2}	Diffusion coefficient of H_2
D_{m,H_2O}	Diffusion coefficient of H_2O through membrane
D_{O_2}	Diffusion coefficient of O_2
e^-	Electron
E	Electrode potential
E^o_{Eq}	Equilibrium potential at standard conditions at zero current
$E^{o\prime}$	Formal potential
E^o_a	Standard anode potential
E^o_c	Standard cathode potential
$E°_{cell}$	Standard cell potential
E_{eq}	Equilibrium potential at zero current
E_{OCP}	Open circuit potential
$E^{o\prime}_r$	Formal potential of rate determining step
F	Faraday constant
f	F/RT
ΔG	Gibbs free energy
$\Delta G°$	Standard Gibbs free energy
H	Henry's constant
H^+	Hydrogen ion
H_2	Hydrogen
H_{ad}	Adsorbed hydrogen
HCl	Hydrochloric acid
HCO_3^-	Bicarbonate ion
H_2O	Water
H_2O_{ad}	Adsorbed H_2O
H_2SO_4	Sulphuric acid
H_3PO_4	Phosphoric acid
i	current
i_0	Exchange current
i_c	Charging current
i_f	Film current
i_k	Kinetic current
$\vec{i}_k$	Kinetic current for forward reaction
i_L	Limiting current
$i_{L,a}$	Anodic limiting current
$i_{L,C}$	Limiting current corresponding to carbon in Pt/C
$i_{L,c}$	Cathodic limiting current
i_{L,H_2}	Limiting current arising from resistance to mass transfer of H_2
i_{L,H_2O}	Limiting current arising from resistance to mass transfer of H_2O
i_{L,O_2}	Limiting current arising from resistance to mass transfer of O_2
$i_{L,Pt}$	Limiting current corresponding to Pt in Pt/C
$i_{L,Pt\ disk}$	Limiting current from Pt disk

K	Equilibrium constant
k	Rate constant
k_b	Rate constant for backward reaction
k_f	Rate constant for forward reaction
$\vec{k}$	Rate constant for forward reaction
KOH	Potassium hydroxide
L	Film thickness
L_{GDL}	Thickness of GDL
L_m	Thickness of membrane
L_{Pt}	Pt loading
l_{IL}	Thickness of the catalyst layer plus inert layer of IL-MEA
l_{Ref}	Thickness of the catalyst layer of Ref-MEA
m	Slope
n	Number of electrons
n'	Number of electron when geometric area is equal to effective diffusion area
$\dot{n}_{in,O_2}$	Molar flow rate of O_2 at inlet
$\dot{n}_{out,H_2O}$	Molar flow rate of H_2O at outlet
$\dot{n}_{out,O_2}$	Molar flow rate of O_2 at outlet
N_2	Nitrogen
O	Oxidant
O_2	Oxygen
O_{2ad}	Adsorbed O_2
OH^-	Hydroxyl ion
p_{g,O_2}	Partial pressure of O_2 in gaseous phase
p_{H_2}	Partial pressure of H_2
p_{H_2O}	Partial pressure of H_2O
p_{l,O_2}	Partial pressure of O_2 in liquid phase
p_{N_2}	Partial pressure of N_2
p_{O_2}	Partial pressure of O_2
Pt	Platinum
Pt/C	Platinum supported on carbon
Q_C	Charge
R	Universal gas constant
R	Reductant or Resistance
R_u	Uncompensated resistance
r_0	Radius of the electrode
s_i	Stoichiometric coefficient of species i
T	Temperature
T_d	Dew point temperature
$\dot{V}$	Volumetric flow rate
v_r	Velocity in radial direction
v_y	Velocity in axial direction
y_H	Hydrodynamic boundary layer

Greek symbol and related expressions

α	Charge transfer co-efficient
α_f	Charge transfer co-efficient of forward reaction
α_b	Charge transfer co-efficient of backward reaction
β	Symmetry factor
Γ_i	Surface excess of species i
Γ_s	Surface excess of species i at saturation
$\gamma + 1$	Step number of $rate\ determining\ step$ in a multistep reaction
γ_O	Activity coefficient of oxidant O
γ_R	Activity coefficient of reductant R
δ	Diffusion layer thickness
ε	Porosity
η	Overpotential
$\eta^A_{CL,iR}$	Overpotential due to ohmic loss in anode catalyst layer
$\eta^C_{CL,iR}$	Overpotential due to ohmic loss in cathode catalyst layer
$\eta^A_{H_2,mt}$	Overpotential due to H_2 mass transfer loss at anode
$\eta^A_{H_2O,mt}$	Overpotential due to H_2O mass transfer loss at anode
η_{IL}	Overall overpotential of IL-MEA
$\eta_{iR,AMFC}$	Overpotential due to ohmic losses in AMFC
$\eta_{iR,IL}$	Overpotential due to ohmic losses in IL-MEA
$\eta_{iR,Ref}$	Overpotential due to ohmic losses in Ref-MEA
η^{mem}_{iR}	Overpotential due to ohmic losses in membrane
$\eta_{k,AMFC}$	Overpotential due to kinetic losses in AMFC
$\eta_{k,PEMFC}$	Overpotential due to kinetic losses in PEMFC
η^A_k	Overpotential due to kinetic losses at anode
η^C_k	Overpotential due to kinetic losses at cathode
η_{mt}	Overpotential due to mass transfer losses
$\eta_{mt,AMFC}$	Overpotential due to mass transfer losses in AMFC
$\eta_{mt,IL}$	Overpotential due to mass transfer losses in IL-MEA
$\eta_{mt,Ref}$	Overpotential due to mass transfer losses in Ref-MEA
$\eta_{Overall,AMFC}$	Overpotential due to kinetic, ohmic, mass transfer losses in AMFC
$\eta^C_{O_2,mt}$	Overpotential due to O_2 mass transfer losses at cathode

η_{Ref}	Overpotential due to kinetic, ohmic, mass transfer losses in Ref-MEA
θ	Fractional coverage of the adsorbed species on the catalyst surface
θ_{O_2}	Fractional coverage of adsorbed O_2 on the catalyst surface
θ_{e,H_2O}	Fractional coverage of adsorbed water at equilibrium
θ_{e,O_2}	Fractional coverage of adsorbed O_2 at equilibrium
λ	Number of times the $rate\ determining\ step$ is repeated
ν	Viscosity of the electrolyte
ρ	Density
σ	Conductivity
τ	Touristy factor
υ	Scan rate
ω	Angular velocity of rotating disk electrode

Kurzfassung

Jüngste Fortschritte in der Entwicklung von Anionen-Austausch-Membranen und deren Ionomer haben es ermöglicht, dass alkalische Brennstoffzellen auch ohne Flüssigelektrolyt betrieben werden können. Alkalische-Membran-Brennstoffzellen (AMFCs) sind daher eine vielversprechenden Alternative zu Polymer-Elektrolyt-Membran-Brennstoffzellen (PEMFCs). Sie brauchen beispielsweise keine Edelmetall Katalysatoren für die Sauerstoff-Reduktion und die Wasserstoff-Oxidation. Obwohl die Leistungsdichte von AMFCs in den letzten Jahrzehnten um eine Größenordnung verbessert werden konnte, sind sie derzeit ungefähr halb so leistungsfähig wie herkömmliche PEMFCs, wenn Sie Platin/Kohlenstoff (Pt/C) als Katalysator an Anode und Kathode einsetzen und bei vergleichbaren Betriebsbedienungen genutzt werden. Es gibt zahlreiche Untersuchungen zu den Ursachen dieser geringen Leistungsfähigkeit von AMFCs. Dabei sind jedoch experimentelle Nachweise rar und eine systematische Analyse sämtlicher Einflussfaktoren auf die Verluste der Leistungsfähigkeit auf Brennstoffzellen-Ebene existiert bisher nicht. Gegenstand der bisherigen Untersuchungen sind vor allem die Beiträge des Stoffübergangs, der Kinetik und der ohmschen Verluste zum Gesamtverlust der Leistungsfähigkeit.

In dieser Arbeit wird die Überspannung durch Verluste im Stoffübergang über die Grenzstromdichte für die gesamte Zelle abgeschätzt. Die Grenzstromdichte hängt dabei von den einzelne Reaktion und Konzentrationen ab. Im Wesentlichen wird sie, Grenzstromdichte aus den Transportwiderständen des Wassers von Strömungskanal zur Katalysator-Schicht und der Rücktransport von wasser von Anode zu Kathode durch die Membran bestimmt. Darauffolgend wird der Rücktransport von Wasser von Anode zu Kathode über den Fluss von Wasser durch die Membran bestimmt. Darüber hinaus, werden Diffusionskoeffizient, Löslichkeit und Permeabilität von Sauerstoff im Ionomer mittels Messungen an Rotierenden Scheibenelektrode (RDE) bestimmt. Die kinetischen Verluste werden identifiziert uber die abhängigkeit der kinetik parameter von Katalysator-Beladung, Diffusions-kontrollierter Grenzstromdichte und Sauerstoff-Konzentration. Dabei wird eine Methode vorgestellt und verwendet, mit der man die Grenzstromdichte im Bezug auf Platin bei geringen Beladungen mit Pt/C bestimmen und der Einfluss der Kohlenstoff-Beladung subtrahieren kann.

Für AMFCs werden Polarisationskurven für verschiedene Beladungen an Anode und Kathode gemessen, um den jeweiligen Anteil von Anoden- und Kathoden-Überspannung am Gesamtverlust der Leistungsfähigkeit zu analysieren. Durch das Einsetzen einer modifizierten Membran-Elektroden-Einheit (MEA) kann der ionische Widerstand durch eine zusätzliche Katalysator-Schicht in der MEA bestimmt werden, was letztlich dazu dient, den Gesamtanteil an ohmschen Verlusten zu bestimmen. Abschließend werden Stoffübergangs-, ohmsche und kinetische Verluste in AMFCs mit denen von PEMFCs verglichen. Die erzielten Resultate ergeben damit und erfolgreichen gezielte optimierung einen detaillierten Einblick in die derzeitigen Limitierungen der Leistungsfähigkeit von AMFCs.

Abstract

Recent advances in development of the anion exchange membrane and ionomer have opened up the possibilities of constructing Alkaline Fuel Cells which operate without liquid electrolyte. Alkaline Membrane Fuel Cells (AMFCs) are promising alternative over Proton Exchange Membrane Fuel Cells (PEMFCs) as they allow the use of non-precious metal catalyst for oxygen reduction reaction and hydrogen oxidation reaction. Even though the power obtained by AMFC in the last decade has impressively improved by one order, the present best performance is about half that of PEMFC using Pt/C as anode and cathode catalyst at similar operating conditions. There are several suggestions in the literature for potential cause of losses in AMFC performance, however towards this the experimental evidence is rare and the systematic quantification of all these losses at the fuel cell level is scarce. In this thesis, AMFC performance is systematically evaluated to find the performance limiting factors. The contribution of mass transfer, kinetic and ohmic loss to overall loss is quantitatively determined.

The overpotential loss caused by mass transfer losses in AMFC is estimated by determining the overall limiting current. In order to determine overall limiting current, the individual limiting currents are estimated. Primarily, the limiting current arising from transport of H_2O from flow channels to catalyst layer is estimated and then the back transport of H_2O from anode to cathode is determined by measuring the flux of H_2O through membrane. In addition, diffusion coefficient, solubility and permeability of O_2 in ionomer are determined using Rotating Disk Electrode (RDE) technique to evaluate the mass transfer losses associated with O_2 transport through ionomer. The kinetic loss is identified by determining the dependency of kinetic parameters on catalyst loading, diffusion controlled limiting current and O_2 concentration by RDE technique. A procedure for determining the limiting current with respect to Pt at low loadings of Pt/C is exposed by subtracting the influence of carbon activity. In AMFC, measurements of performance curves with various anode and cathode loadings allowed to determine the contribution of anode and cathode over potential to the overall loss. Preparing a modified Membrane Electrode Assembly (MEA) and measuring the ionic resistance offered by the catalyst layer in modified MEA aided in identifying the overall ohmic loss. Finally the mass transfer, ohmic and kinetic losses in AMFC is compared with PEMFC and these results give an in-depth view of bottlenecks in the performance of AMFC and as such enable knowledge driven optimization.

Chapter 1
Introduction[1]

1.1 *Introduction to fuel cells*

Environmental concerns about increase in pollutant gases in the atmosphere due to burning of fossils and limited cache of fossil fuels have led to urgent need of clean and energy efficient technologies. Among the possible technologies, fuel cell technology is a promising alternative due to it's high efficiency, low emissions, silent operation and modularity. Although fuel cell was invented by Sir William Groove in 1839, the first practical fuel cell stack was constructed only in 1959 by Francis T. Bacon [1] to be used for NASA space shuttle. The earliest fuel cells which were developed rigorously and made generation of electricity from hydrogen feasible using concentrated liquid KOH as electrolyte, were Alkaline Fuel Cells (AFCs) [2]. AFCs are promising as it allows the use of non-precious metal catalyst for Oxygen Reduction Reaction (ORR) [3] [4] and Hydrogen Oxidation Reaction (HOR). However, the design of AFC was complicated due to corrosive nature of liquid electrolyte leading to leakage problem in the fuel cell system. Moreover when operated with air the ionic conductivity of liquid electrolyte slowly decreases due to carbonation over a period of time leading to reduced performance and replacement of liquid electrolyte in due course [5]. With the development of solid polymer proton exchange membrane and ionomer in 1970s, the design issues and maintenance of fuel cells have been greatly simplified with improvement in power densities. Since last three decades Proton Exchange Membrane Fuel Cell (PEMFC) technology is preferred

[1] Part of the results of this chapter published in P.S. Khadke, U. Krewer, *Electrochem. Comm*. 51 (2015) 117–120.

over AFC technology [5]. Research activities by companies to name few like Siemens, Ballard, Smart fuel cell and almost every giant car-manufacturers have demonstrated long operation of fuel cell powered prototypes of car/bus/fork lift and many other applications in last two decades. However the major set-back for the mass production of PEMFC is the high cost of Pt catalyst which is used as anode and cathode catalyst. While mass production of fuel cells can reduce most of the component cost, the cost of Pt is unlikely to reduce in the long term due to low abundance of Pt [6].

Fortunately with new recent material developments, the anion exchange membrane and ionomer are commercially available [7] since last decade. This opened up the possibilities of constructing AFCs which operate without liquid electrolyte and renewed the interest in AFC research. AFCs operating with Anion Exchange Membrane (AEM) is often called as Alkaline Membrane Fuel Cell (AMFC).

1.2 *Working principle of AMFCs*

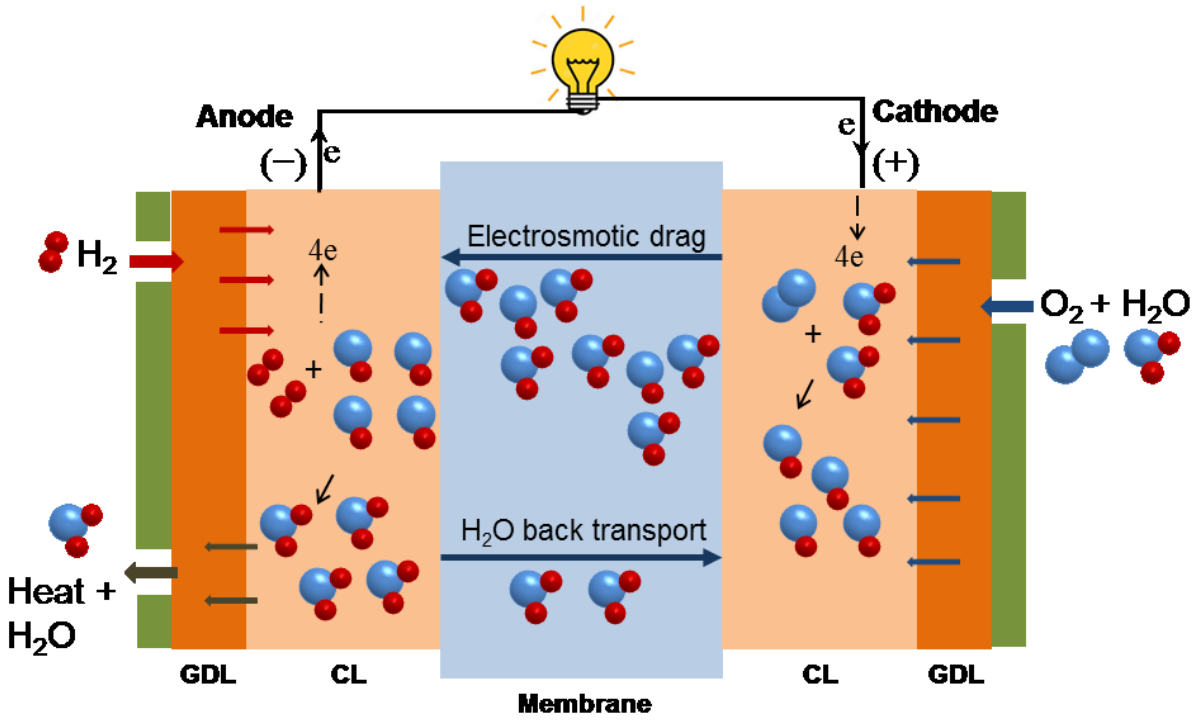

Figure 1.1 Working principle of alkaline membrane fuel cell.

Fuel cells directly convert chemical energy of fuel into electricity. Depending on the type of fuel cell, the reaction mechanism may differ but the underlying principle remains the same. Figure 1.1 shows the schematic representation of the working principle of H_2-O_2 AMFC. The following reactions occur at the anode and the cathode of AMFC.

$$H_2 + 2OH^- \rightleftharpoons 2H_2O + 2e^- \qquad E_a^o = -0.83\,V\ vs\ SHE \qquad (1.1)$$

$$O_2 + 2H_2O + 4e^- \rightleftharpoons 4OH^- \qquad E_c^o = 0.4\,V\ vs\ SHE \qquad (1.2)$$

$$H_2 + \frac{1}{2}O_2 \rightleftharpoons H_2O \qquad E_{cell}^o = 1.23\,V\ vs\ SHE \qquad (1.3)$$

Anode and cathode chambers of AMFC comprise of flow field channels, Gas Diffusion Layer (GDL) and Catalyst Layer (CL). The H_2 at anode and $O_2 + H_2O$ at cathode enter the fuel cell via flow field channels and distribute evenly over CL by passing through GDL. CL comprise of catalyst, catalyst support and Anion Exchange Ionomer (AEI). The role of ionomer in the CL is to facilitate the OH^- transport in the CL and maintain continuity of ionic transport between membrane and CL. The membrane together with anode and cathode electrode is called Membrane Electrode Assembly (MEA). During the operation, cathode catalyst layer catalyzes the cathodic reaction (Equation (1.2)) and resultant product, OH^- passes through AEM to the anode CL where it combines with H_2 in the CL to form water and electricity (Equation (1.1)). The current collectors pass on the electricity to the external circuit. With every one OH^- transport some water molecules may get electro-osmotically dragged to the anode side and in case of excess water accumulation in anode, water may back transport from anode to cathode.

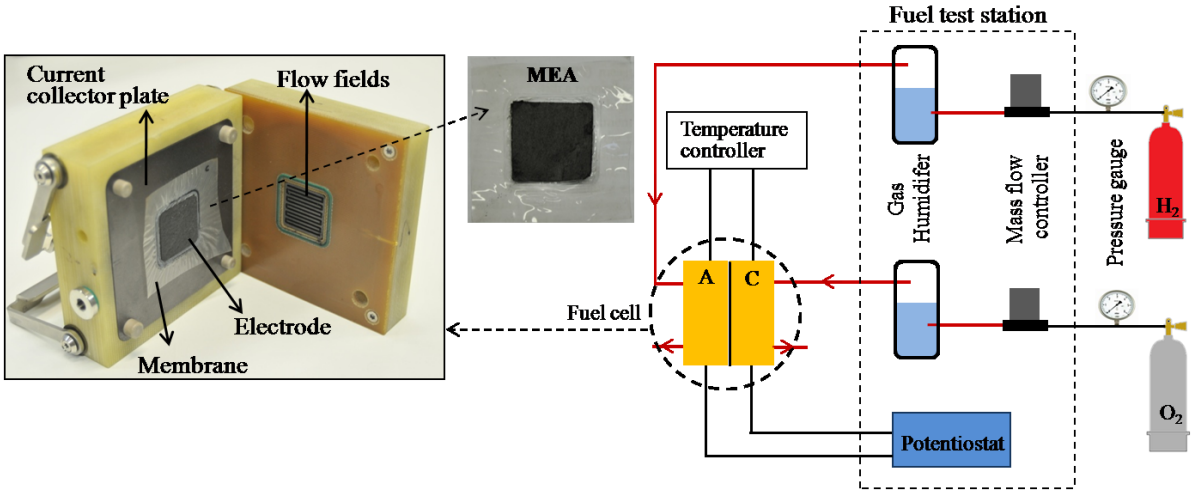

Figure 1.2 Fuel cell test set-up with fuel cell components.

A simple flow diagram of fuel cell test set up is given in Figure 1.2 together with optical image of fuel cell showing flow field, current collector and MEA. Fuel cell test station is used to characterize fuel cell electrochemically, to control temperature and

supply humidified H_2 and O_2 gases. The humidified gas helps in keeping the membrane and ionomer hydrated so that ionic conductivity remains high. In addition at cathode, it is also a source of water for the cathodic reaction.

1.2.1 Performance evaluation

The first impression of performance of a given fuel cell is usually obtained on examining the current-potential curve, also called as $i - E$ curve. Figure 1.3 shows a characteristic $i - E$ curve of AMFC. The cell potential, E_{eq} at zero current is called as Open Circuit Potential (OCP). During operation potential drops below OCP to a value depending on current, the magnitude of the potential drop measured from OCP is called overpotential, η. The potential drops due to polarization losses occurring at anode and cathode which can be broadly classified as kinetic loss, ohmic loss and mass transfer loss. Throughout the $i - E$ curve these losses exist. However in some regions of $i - E$ curve some of these losses are more dominant than other. For example, at low current region kinetic losses are more dominant and in high current region mass transport and ohmic losses are dominant. At medium current all these losses may be dominant and none of them may be negligible. The kinetic and mass transport losses shown in the Figure 1.3 are combined losses from anode and cathode. A general equation defining overall overpotential can be given as

$$\eta = \eta_k^A + \eta_{H_2,mt}^A + \eta_k^C + \eta_{O_2,mt}^C + \eta_{H_2O,mt}^C + \eta_{CL,iR}^A + \eta_{CL,iR}^C + \eta_{iR}^{mem} \qquad (1.4)$$

where η_k^A, $\eta_{H_2,mt}^A$ are kinetic loss and H_2 mass transfer loss respectively at anode; η_k^C, $\eta_{O_2,mt}^C$, $\eta_{H_2O,mt}^C$ are kinetic loss , O_2 mass transfer loss and H_2O mass transfer loss respectively at cathode; $\eta_{CL,iR}^A$, $\eta_{CL,iR}^C$, η_{iR}^{mem} are ohmic losses at anode CL , cathode CL and membrane, respectively.

Often kinetic losses of anode and cathode are difficult to separate and are studied in a separate set-up such as three electrode set-up where the electrode polarization is measured against a reference electrode. For example the kinetic loss from ORR is often studied in a three electrode Rotating Disk Electrode (RDE) set-up.

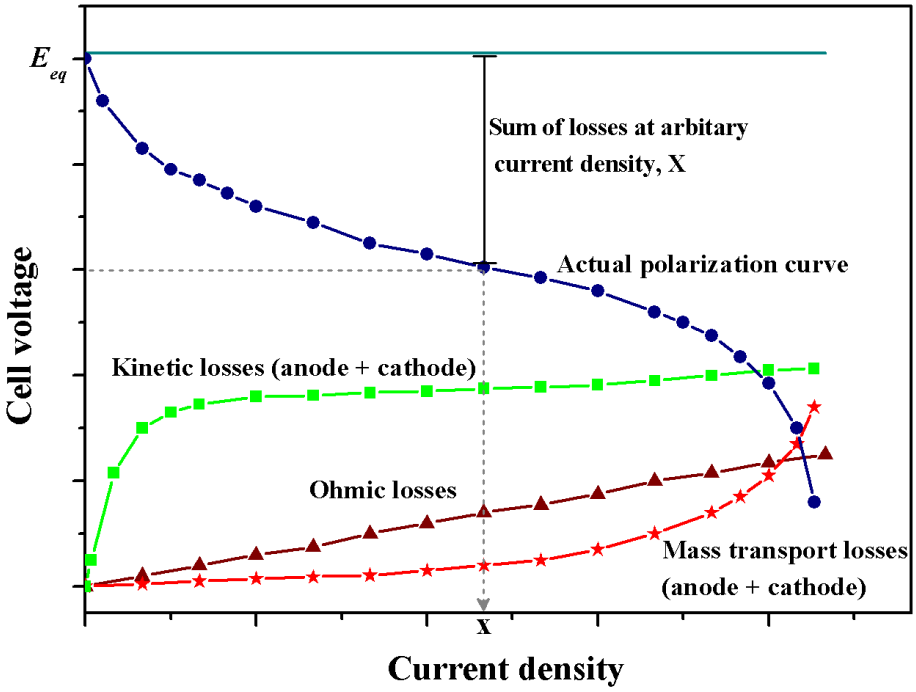

Figure 1.3 Characteristic performance curve (circle) of AMFC showing the relative effect of kinetic losses (square), ohmic losses (triangle) and mass transport losses (star).

1.3 *Introduction to RDE method*

RDE technique is one of the most widely used hydrodynamic method for the study of electrocatalysts. Measurement in three electrode RDE set-up is simpler, cheaper and faster than at the cell level. Figure 1.4 shows the schematic representation of RDE set-up used in this work to study ORR. The set-up comprises of Working Electrode (WE) with the possibility to rotate, Pt coil as Counter Electrode (CE) and Mercury-Mercury Oxide Electrode (MMO) as Reference Electrode (RE). The WE consists of a disk made up of Glassy Carbon (GC) enclosed tightly in a Teflon/PEEK shroud. A typical procedure of preparing a WE consists of coating the catalyst to be studied on GC followed by coating a binder which is preferably AEI in alkaline media. Prior to electrochemical measurements these electrodes are immersed in liquid electrolyte and the electrolyte is saturated by known concentration of O_2 by varying the ratio of O_2 and N_2 in the bubbling gas. The temperature of liquid electrolyte can be varied by heating the liquid electrolyte through a jacketed water bath. The polarization of WE can be measured against RE at various rotation rates of WE with the help of a Potentiostat. Rotation of electrode enables the controlled flow towards electrode and increases the rate of mass transport of reactant

creating steady conditions near the electrode quickly, unlike the stationary electrode. This permits electrochemical measurements at steady state conditions.

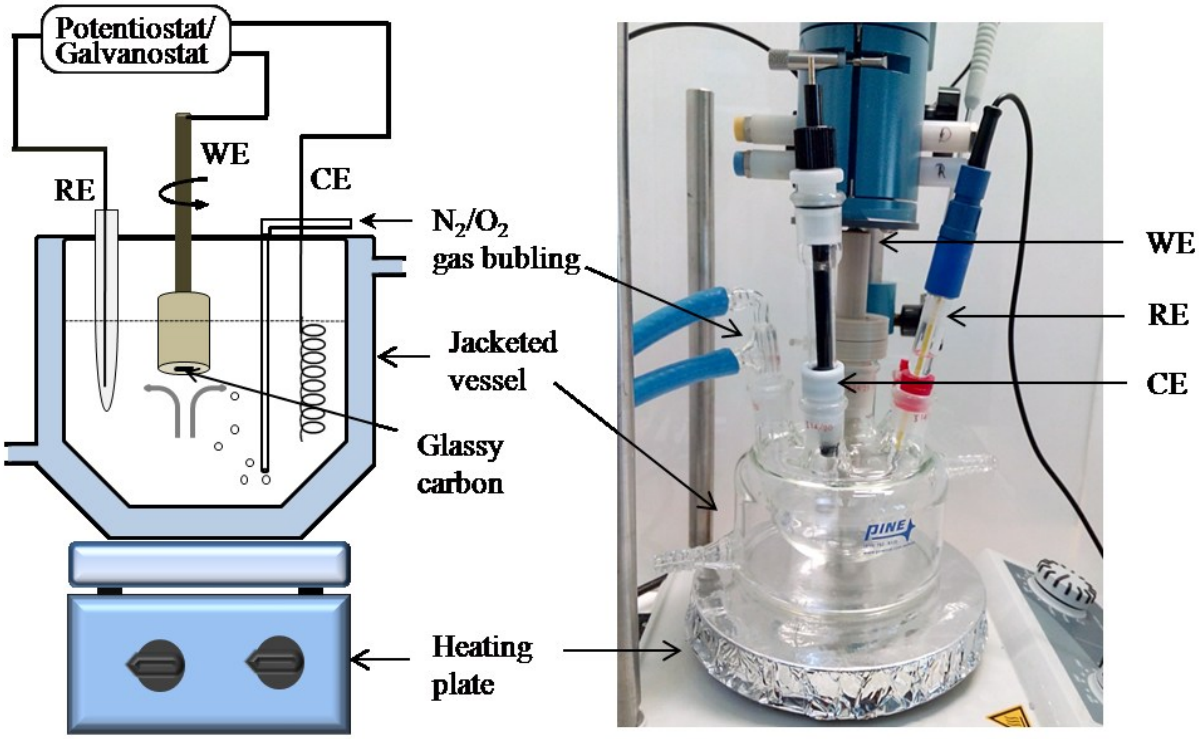

Figure 1.4 Schematic representation (left) of three electrode RDE setup; optical image (right) showing the real RDE set up.

Figure 1.5 shows the schematic view of flow streamlines near the RDE surface. As the electrode is rotated, a liquid layer is dragged along the rotating electrode and remains stagnant with respect to the electrode surface. This layer is termed as hydrodynamic boundary layer or Prandtl boundary layer. Much of the species transfer towards electrode with in hydrodynamic boundary layer occurs via convection. As the species moves closer to the electrode surface convection ceases and diffusion becomes dominant. The layer where mass transfer of species mainly occurs via diffusion is termed as diffusion layer. Due to the precise control of the rotation, the thickness of hydrodynamic boundary layer and diffusion layer, and mass flux of species can be defined in terms of mathematical model as described in Section 1.3.1.

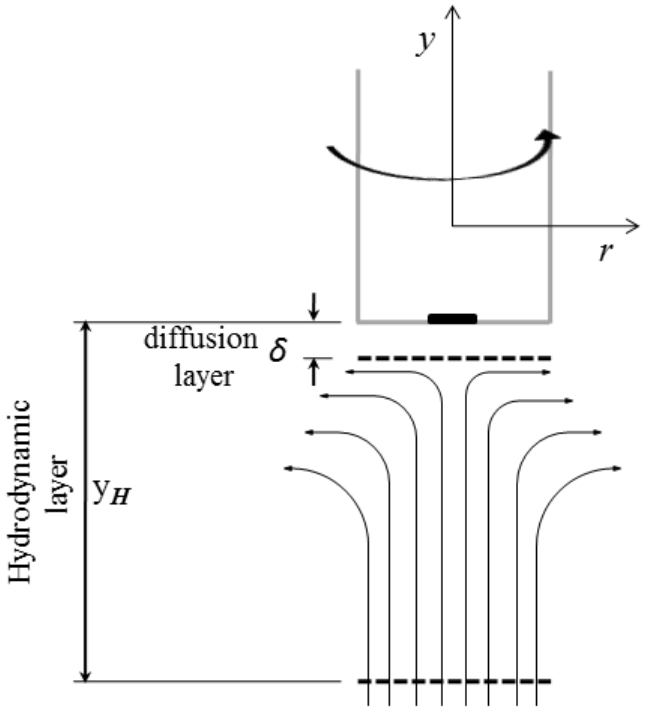

Figure 1.5 Flow profile at rotating disk electrode.

Alternatively, micro electrodes can also be used for electrochemical measurements at steady state conditions, thereby eliminating the need for rotation and simplifying the data processing. However, often catalyst to be studied is nano-sized metal particles dispersed on high surface area porous carbon support where catalytic activity is a function of catalyst particle size. It is difficult to obtain reproducible coating of these catalysts on the microelectrode surface (< 100 μm diameter).

1.3.1 Koutecky-Levich equation

For a reduction reaction $O + ne^- \rightarrow R$, at RDE where n is number of electrons , the flux of species *O,* J_j arriving at the electrode in an electrochemical cell can be given by Nernst-Planck equation,

$$J_j = -D_j \nabla C_j - \frac{z_j \mathrm{F}}{RT} D_j C_j \nabla \Phi + C_j \boldsymbol{v} \tag{1.5}$$

On right hand side, the first term represents diffusion, the second term represents migration, and the third term represents convection. For the system where liquid

electrolyte is in excess, the migration term can be neglected [8]. Assuming no variation of D_j with respect to x, y, z direction this equation reduces to,

$$\frac{\partial C_j}{\partial t} = D_j \nabla^2 C_j - \boldsymbol{v}.\nabla C_j \tag{1.6}$$

To solve this equation velocity profile $\boldsymbol{v}(x, y, z)$ must be obtained in terms of the rotation rate in x, y, z direction. The velocity profile near the electrode was obtained by von Karman [9] and Cochran [10] by solving the above equation under steady state conditions. They showed that velocity in axial and radial direction can be represented in terms of electrolyte viscosity ν and angular velocity ω of the rotating disk electrode,

$$v_y = 0.51\omega^{3/2}(\nu)^{-1/2}(y^2) \tag{1.7}$$

$$v_r = 0.51\omega^{3/2}(\nu)^{-1/2}ry \tag{1.8}$$

and the hydrodynamic boundary layer thickness can be given as

$$y_H = 3.6(\nu/\omega)^{1/2} \tag{1.9}$$

and the concentration gradient $\frac{\partial C_O}{\partial r}$ in the radial direction is zero and hence there is no flux or formation of diffusion layer in the radial direction.

Using this result, Levich [11] derived the equation for limiting current, i_L in axial direction as,

$$i_L = \left(0.62n\mathrm{F}AD^{2/3}\nu^{-1/6}(C_B - C_0)\right)\omega^{1/2} \tag{1.10}$$

where n is the number of electrons transferred, F is the Faraday's constant, A is the geometric area of the electrode, D is the diffusion coefficient of the reactant in the electrolyte, C_B is the bulk concentration or solubility of the reactant in the electrolyte and C_0 is the surface concentration which is close to zero.

Considering Fick's first law of diffusion, Equation (1.10) can be also rewritten as,

$$i_L = nFA\left(\frac{D}{\delta}\right)C_B \tag{1.11}$$

where diffusion layer thickness,

$$\delta = 1.61D^{1/3}\omega^{-1/2}\nu^{1/6} \tag{1.12}$$

For a typical value of D = 10^{-5} $cm^2 \cdot s^{-1}$, ν = 0.01 $cm^2 \cdot s^{-1}$ and ω = 30 - 400 s^{-1}, the diffusion layer thickness ranges from 10 to 40 μm. Further Koutecky and Levich [12] derived the so called Koutecky-Levich equation for current at any fixed potential as,

$$\frac{1}{i} = \frac{1}{i_k} + \frac{1}{i_L} \tag{1.13}$$

Where i is the measured current from disk, i_k is the potential dependent kinetic current and i_L is the diffusion limited current dependent on ω, as shown in Equation (1.10). The i_k and i_L in the Koutecky-Levich equation are conceptual descriptors, i_k is the current that would be reached when there is no mass transfer limitation for transport of electroactive species from bulk to electrode surface.

At any fixed potential in the limiting current region, the disk current is described by Koutecky-Levich Equation (1.13). For the film coated catalyst layer there is an additional resistance offered by the film and Equation (1.13) is modified as below [13],

$$\frac{1}{i} = \frac{1}{i_k} + \frac{1}{i_f} + \frac{1}{i_L} \tag{1.14}$$

where i_f is the film thickness dependent current and can be expressed as $nFA(HC_i - 0)D_f L^{-1}$, where C_i is the concentration of O_2 outside the film at film-liquid interface, H is Henry's constant for partition of O_2 at film-liquid interface, D_f is the diffusion coefficient of the reactant in film and L is the film thickness.

1.3.2 Transients at RDE

Although steady state is reached at RDE much faster than the stationary electrode, there exists some short time which the electrode takes to reach steady state. According to Prater *et al.*, [14] the time to reach steady state at RDE can be given as,

$$t \geq \frac{2.036}{\omega}(\nu/D)^{1/3} \tag{1.15}$$

Assuming diffusion co-efficient values as 1.9 · 10^{-5} $cm^2 \cdot s^{-1}$ and 4.65 · 10^{-5} $cm^2 \cdot s^{-1}$ and viscosity values as 0 .01 $cm^2 \cdot s^{-1}$ and 0.00457 $cm^2 \cdot s^{-1}$ [15] for O_2 in 0.1 M KOH solution at 20 °C and 60 °C respectively, at a rotation rates of 1600 rpm; the current will reach its steady state value within 0.076 s and 0.06 s for 20 °C and 60 °C respectively.

1.4 *State of art AMFC of performance*

It is widely perceived that performance of AMFC employing Pt/C as anode and cathode catalyst can be significantly increased by developing AEM/AEI with improved properties. The main requirements for a membrane to be used in AMFC are high conductivity and high chemical, thermal and mechanical stability. Much of the development on the membranes is to improve these properties. There is a vast amount of literature in the development of anion exchange membranes which are targeted to be used for other applications such as electrodialysis and electrolysis apart from AMFC. To confine the discussion within the scope of this thesis, only the literature where the working of the AEM/AEI is demonstrated without use of liquid electrolyte in AMFC is presented. Although reasonable conductivity values comparable to Nafion membrane between 30 - 70 $mS \cdot cm^{-1}$ [16] [17] [18] [19] have been achieved recently, thermal, chemical and mechanical stability still remains a challenge in alkaline media. Ionic conductivity is often improved by increasing the ion exchange capacity; however, it generally increases the water uptake leading to mechanical instability [7]. The other challenge is the degradation of polymer backbone and cation functional group by hydroxyl attack in alkaline media [7]. Nevertheless some research groups successfully prepared a membrane and demonstrated its working in AMFC even though the proof of long term operation is rarely reported. An overview of AMFC performances with these membranes are shown in Table 1.1.

As can be seen, the AMFC performances obtained by most research groups are mediocre in comparison to state of art PEMFC performance. In the published literature the highest to date power density is reported by Alesker *et al.* [20] and Piana *et al.* [21]. However Piana *et al.* [21] also showed that the power reduces to half its value with in 30 h of the long term test. The best durability result has been obtained by Luo *et al.* [22], with almost no sign of degradation in AMFC power until 50 h and slow degradation rate of ~ 400 $\mu V \cdot h^{-1}$ until 460 h using their membrane. Albeit the maximum power obtained by their AMFC is only 50 $mW \cdot cm^{-2}$ at 50 °C. Notable efforts are already underway by CellEra [23] where the company claims to have developed 1 kW stack of AMFC and obtained short term power density of about 700 $mW \cdot cm^{-2}$ at 80 °C with H_2 and O_2 pressurized at 2 bar on smaller 5 cm^2 single cell employing membrane and ionomer from Tokuyama Corporation. They have also demonstrated the durability of operational 5 cm^2 AMFC single cell for up to 800 h with voltage degradation of 40 $\mu V \cdot h^{-1}$. To date these are the best results obtained in the development of AMFCs. Given the early stage of

AMFC development, it is a significant achievement in short time; however this durability is still far from the demonstrated durability in PEMFC technology. Also, reasonable power density of 200 mW · cm^{-2} has been obtained with AMFC operating with non-platinum cathode catalyst [21] and 50 mW · cm^{-2} has been obtained with AMFC operating with non-precious cathode catalyst at both anode and cathode catalyst [24].

In the last decade the power obtained by AMFC has impressively improved by one order and now the best performance is about half that of PEMFC using Pt/C as anode and cathode catalyst at similar operating temperature. As the power and durability of AMFC have been increased significantly, the gap between AMFC and PEMFC technology is expected to come closer in near future.

1.4 State of art AMFC of performance

Table 1.1 State of the art AMFC performance

Fuel / Oxidant	**Anode catalyst loading ($mg_{Metal} \cdot cm^{-2}$)**	**Cathode catalyst loading ($mg_{Metal} \cdot cm^{-2}$)**	**Membrane / ionomer**	**Ionic conductivity ($mS \cdot cm^{-1}$) at ambient conditions**	**Max. Power density ($mW \cdot cm^{-2}$)**	**Temp (°C)**	**Ref.**
H_2/O_2 no back pressure (bp)	60 wt.% Pt/C - 0.07	60 wt.% Pt/C - 0.1	Tokuyama A201 membrane/ AS-4 ionomer	[a]0.2	90	60	[25]
H_2/O_2 no bp	40 wt.% Pt/C - 0.7, 40 wt.% Pt/C - 0.7	40 wt.% Pt/C - 0.7, Acta K-14 - 0.7	40 μm commercial membrane and commercial ionomer	70	180, 110	80	[16]
H_2/O_2 no bp	30 wt.% Pt/C - 0.5	30 wt.% Pt/C - 0.5	Tokuyama A-201 membrane, AS-4 ionomer	42	90	50	[17]
H_2 at 4 bar O_2 at 2 bar	Pd/Ni -1.5, Pd -1.5	Ag alloy - 3	Unknwon	-	400, 180	73	[20]
H_2/Air no bp	40 wt.% Pt/C - 0.45	40 wt.% Pt/C - 0.45	Unknown commercial membrane	-	400	50	[21]
H_2/Air no bp	40 wt.% Pt/C - 0.45	4020 acta cat FeCu/C - 0.8	Unknown commercial membrane	[a]0.2	200	50	[21]
H_2/O_2 at ~1 bar	60 wt.% Pt/C - 0.4	60 wt.% Pt/C - 0.4	QPMV-PDMV [quaternized poly (methyl methacrylate-co-butyl acrylate-co-vinylbenzyl chloride)]	10	50	50	[22]
H_2/Air no bp	20 wt.% Pt/C - 1	20 wt.% Pt/C - 1	Chitosan cross-linked with gluter-aldehyde	10-30	8	20-25	[26]
H_2/O_2 no bp	20 wt.% Pt/C - 0.5	20 wt.% Pt/C - 0.5	silica/poly(2,6-dimethyl-1,4-phenylene oxide	35	32	50	[18]

H_2/O_2 no bp	20 wt.% Pt/C - 0.5	20 wt.% Pt/C - 0.5, 20 wt.% Au/C - 0.5, 20 wt.% Ag/C - 0.5	Quaternized / cross-linked PCMS	9.2	230, 32, 15	50	[27]
H_2/O_2 no bp	20 wt.% Pt/C - 1	20 wt.% Pt/C - 1	Poly (methyl methacrylate-co-butyl-acrylate-co-vinyl benzyl)	8.2	35	60	[28]
H_2/O_2 no bp	20 wt.% Pt/C - 0.5	20 wt.% Pt/C - 0.5	ETFE/PVB trimethyl ammonium	Up to 34	130	50	[19]
H_2/O_2 at 2.5 bar	20 wt.% Pt/C - 1	20 wt.% Pt/C - 1	N-[(2-hydroxy-3-trimethylammonium)propyl] chitosan	4.8-7.3	14	50	[29]
H_2/O_2 no bp	Pt black - 4	Pt black - 4	Quarternary ammonia polysulfone	20	110	60	[30]
H_2/O_2 at 1.3 bar	Ni-Cr - 5	Ag-1	Trimethylammonium PSU	10	50	60	[24]
H_2/Air no bp	40 wt.% Pt/C - 0.5	40 wt.% Pt/C - 0.5	N, N, N, N – tetramethyl-1,6-hexanediamine (TMHDA) / trimethylamine (TMA)	[a]2.3	28	60	[31]

[a] cell resistance in $\Omega \cdot cm^{-2}$ as measured by high frequency impedance.

1.5 *Motivation and scope of the Thesis*

As shown in Table 1.1 the performance of H_2-O_2 AMFC employing commercial AEM and AEI is low in relation to PEMFC. Our measurements also show (Figure 1.6) low AMFC performance in relation to PEMFC performance measured at similar catalyst loading and operating conditions. To determine the performance limiting factor, the most straightforward method is to measure the single electrode polarization of cathode/anode with respect to a fast reversible reaction such as hydrogen oxidation reaction (HOR) / hydrogen evolution reaction (HER). For the case where kinetically fast reaction is not feasible, an additional reversible hydrogen reference electrode is attached to membrane-electrolyte which is positioned away from the direct current path between anode and cathode. This method of single electrode polarization measurement has been studied by several groups [32] [33] [34] [35] in PEMFC employing Nafion membrane and ionomer by having one or more additional reference electrodes. Using this method Zeng *et al.* [36] concluded that anode limits the AMFC performance for CL with AEI. However the method suffers from uncertainty in measured potential mainly because measured potential is highly sensitive to the position of the reference electrode with respect to anode/cathode [34] [35]. On the contrary, study of HOR/HER kinetics in alkaline media using RDE technique [37] showed anode potential losses of about 150 mV at 1.5 $A \cdot cm^{-2}$ at a Pt loading of 0.05 $mg \cdot cm^{-2}$. Although this potential loss is significant and two orders of magnitude higher than in acidic media, it is expected to be much lower than 150 mV with higher loadings of Pt often used in AMFC literature. Even though the HOR/HER kinetics are lower in alkaline media in relation to acidic media, it is still sufficiently higher than ORR kinetics in alkaline media and hence does not explain the low performance obtained in AMFC. Furthermore it has been shown by several other groups [37] [38] [39] that the ORR kinetics in alkaline media is as facile as in acidic media by RDE technique. Filpi *et al*. [16] evaluated the performance of H_2/O_2 AMFC and proposed that the difference between estimated performance after kinetic and ohmic correction and the measured performance could be due to transport losses such as reactant transport and OH^- transport. Apart from this, major reasons for low performance suggested in the literature is insufficient water supply at cathode even with humidified Air/O_2 at practical stoichiometries [40] and low ionic conductivity of membrane and ionomer [7].

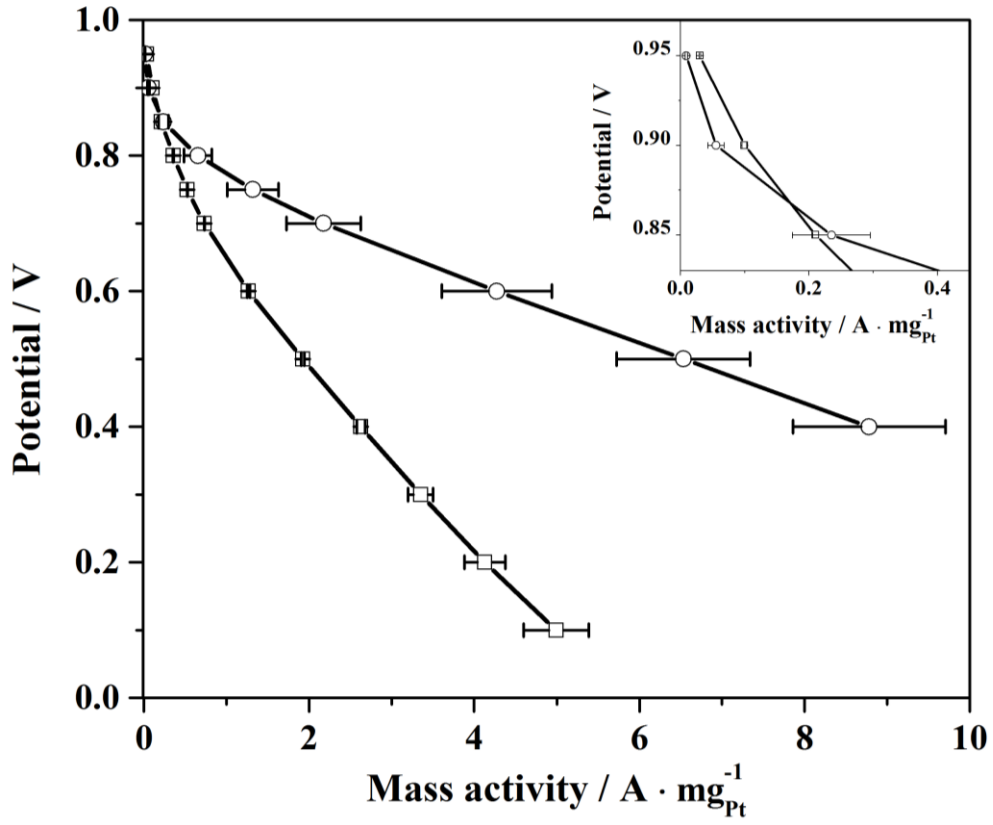

Figure 1.6 Comparative normalized polarization curves for AMFC and PEMFC MEAs measured with anode - 0.107 $mg_{Pt} \cdot cm^{-2}$/ cathode - 0.107 $mg_{Pt} \cdot cm^{-2}$ loadings: AMFC (empty square); PEMFC (empty circle). Inset: enlarged view of the kinetic region.

However, in most of the studies in literature, there are suggestions for potential cause for low performance with little experimental evidences. Systematic quantification of all these losses at the fuel cell level is scarce in literature. In this work, AMFC performance is systematically evaluated to find the performance limiting factors. The contribution of kinetic, mass transfer and ohmic loss to overall loss is quantitatively determined. These losses are compared with losses present in PEMFC whenever deemed necessary.

As a guide, Figure 1.7 shows the distribution of chapters in the present Thesis and types of overpotential losses included in each chapter.

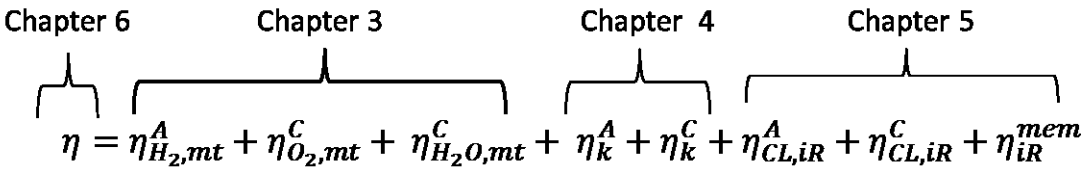

Figure 1.7 Distribution of types of over-potential losses in the chapters.

The brief chapter-wise description is given below:

Chapter 2 introduces the basic concepts and theory useful in understanding the present Thesis. The behavior of current-overpotential relation at various scenarios such as low overpotential, high overpotential and with mass transfer limitation are described. The concept of electrochemical techniques such as Chronoamperometry and Cyclic Voltammetry are introduced. The experimental details of electrode preparation for RDE set up and fuel cell are described. This chapter also includes the results of preliminary studies conducted to show electrochemical stability of ionomer.

Chapter 3 investigates the overpotential losses caused by mass transfer limitations of H_2, O_2 and H_2O transports in AMFC. The diffusion coefficient of H_2O through membrane is determined at 60 °C using dew point temperature measurements to evaluate the back transport of H_2O from anode to cathode. With these results the limiting current expected in AMFC is estimated. Diffusion coefficient, solubility and permeability of O_2 in ionomer are determined at 22 °C and 60 °C using RDE technique to evaluate the mass transfer losses associated with O_2 transport through ionomer.

Chapter 4 investigates the contribution of kinetic losses to overall loss in AMFC. ORR kinetics is evaluated at an elaborate range of O_2 concentrations and overpotential values in RDE set up enabling to determine a rate expression describing the ORR kinetics. In AMFC, measurements of performance curves with various anode and cathode loadings allowed to estimate the contribution of anode and cathode over potential to the overall loss. Further the overpotential caused by ORR kinetics in AMFC is evaluated by extracting the kinetic parameters from mass transfer corrected current - overpotential curves.

Chapter 5 provides the results of ohmic losses measured in AMFC. In this chapter the ionic resistance offered by anode catalyst layer, cathode catalyst layer and membrane are measured. These results are then compared with the ohmic loss present in PEMFC.

Chapter 6 summarizes the main findings of the Thesis and discusses the requirements and the operating conditions at which AMFC performance may come closer to PEMFC performance. Future perspective and further research directions are also discussed.

Chapter 2
Theory, Techniques and Experimental Details[2]

2.1 *Theory*

The overall reaction of an electrochemical cell can be divided into two half-cell reaction. Considering a cell with following reaction at WE, where the prefix s_i represents the stoichiometric coefficient,

$$s_O O + ne^- \rightleftarrows s_R R \tag{2.1}$$

and the reaction that of Normal Hydrogen Electrode (NHE) at reference electrode as,

$$s_{H_2} H_2 \rightleftarrows s_{H^+} H^+ + ne^- \tag{2.2}$$

The overall reaction is

$$s_{H_2} H_2 + s_O O \longrightarrow s_R R + s_{H^+} H^+ \tag{2.3}$$

Change in Gibbs free energy of this reaction can be given as,

$$\Delta G = \Delta G° + RT \ln \frac{a_R^{s_R} a_{H^+}^{s_{H^+}}}{a_O^{s_O} a_{H_2}^{s_{H_2}}} \tag{2.4}$$

[2] Part of the results in this Chapter published in P.S. Khadke, U. Krewer, *J. Phys. Chem. C*, 118 (**2014)** 11215-11223.

where a_i is the activity of species i, R is the universal gas constant and T is the temperature. Since $\Delta G = -nFE_{eq}$ and $\Delta G° = -nFE^o_{Eq}$, where E_{eq} is the equilibrium potential at current zero and E^o_{Eq} is the equilibrium potential at standard conditions and current zero. Equation (2.4) takes the form of Nernst equation

$$E = E^o_{Eq} - \frac{RT}{nF}\ln\frac{a_R^{s_R} a_{H^+}^{s_{H^+}}}{a_O^{s_O} a_{H_2}^{s_{H_2}}} \tag{2.5}$$

For NHE $a_{H^+} = a_{H_2} = 1$

$$E = E^o_{Eq} + \frac{RT}{nF}\ln\frac{a_O^{s_O}}{a_R^{s_R}} \tag{2.6}$$

2.1.1 Electrode potential

Since the activities are generally unknown for the real experiments, it is difficult to calculate the electrode potential from Equation (2.6). To overcome this difficulty the formal potential $E^{o\prime}$ is used in literature instead of E^o_{Eq}. The formal potential is a measured potential at conditions such that $C_O^{s_O}/C_R^{s_R}$ is set equal to 1. Equation (2.6) can be rewritten as

$$E = E^o_{Eq} + \frac{RT}{nF}\ln\frac{\gamma_O C_O^{s_O}}{\gamma_R C_R^{s_R}} \tag{2.7}$$

where γ_O and γ_R are the activity coefficient of O and R respectively and the measured formal potential is given by

$$E^{o\prime} = E^o_{Eq} + \frac{RT}{nF}\ln\left(\gamma_O/\gamma_R\right) \tag{2.8}$$

The formal potential is affected by ionic strength, impurities, and ion paring [41] and may change from medium to medium. The formal potential might differ significantly for instance in 0.1 M KOH to the conditions present in fuel cell. Hence the medium specific equilibrium potential at zero current after incorporating medium specific formal potential can be written as

$$E_{eq} = E^{o\prime} + \frac{RT}{nF}\ln\frac{C_O^{s_O}}{C_R^{s_R}} \tag{2.9}$$

During operation potential deviates from E_{eq} to a value depending on current, hence the overpotential for the reaction occurring at WE can be defined as,

$$\eta_k = E - E_{eq} \tag{2.10}$$

2.1.2 Current – overpotential relation for electrochemical reactions

For many reactions the potential E in Equation (2.10) depends on ratio of reactant and product surface concentration and as well as on the rate of reaction. Hence Nernst equation cannot be used to determine the value of E as it does not show any dependencies of E on reaction kinetics. For such cases Butler-Volmer equation is generally used. The seminal work by J. A. V. Butler [42], M. Volmer and T. Erdey Gruz [43] led to origin of widely adopted Butler-Volmer equation. Butler-Volmer equation shows the relation between current and overpotential for a one step one electron electrochemical reaction such as, $O + ne^- \rightleftharpoons R$. Butler-Volmer equation has its origin from activated complex theory and assumes that reactant has to overcome an energy barrier called activation energy to form products and vice versa. It is given by

$$i_k = i_0[e^{-\beta f \eta_k} - e^{(1-\beta) f \eta_k}] \tag{2.11}$$

where β is the symmetry factor, $f = F/RT$. When the electrode is not polarized, the cathodic and anodic reactions are at dynamic equilibrium, with anodic and cathodic current equal to a current termed as exchange current, i_0.

$$i_0 = FAk_f C_O e^{-\beta f (E_{eq} - E^{O\prime})} = FAk_b C_R e^{(1-\beta) f (E_{eq} - E^{O\prime})} \tag{2.12}$$

where C_O and C_R are the surface concentration of reactant and product respectively, k_f and k_b are the rate constants of forward and backward reactions respectively. Since the exchange current is directly proportional to rate constants, it is the measure of reaction rate: the higher the i_0 value higher the reaction rate.

For a multistep reaction Equation (2.11) can be rewritten as,

$$i_k = i_0\left[e^{\alpha_b f \eta_k} - e^{-\alpha_f f \eta_k}\right] \tag{2.13}$$

This equation is of similar form as Equation (2.11), however in this charge transfer coefficient α is different than β and may take values other than 0.5. For example for a

multistep reaction, $\alpha_f = \frac{\gamma}{\lambda} + r\beta$ [44], where γ +1 is the step number of the rate determining step (rds), λ is the number of times rds is repeated and r = 0 for a chemical rds and r = 1 for a charge transfer rds. The charge transfer coefficient is critical in determining the reaction pathway.

2.1.3 Determination of exchange current density and charge transfer coeffcient

At small overpotentials (η_k < -10 mV), e^x can be approximated as $1 + x$ according to Taylor expansion, so that,

$$i_k = 2i_0\alpha_f f\eta_k \tag{2.14}$$

This equation can be applied only for fast reactions where significant measurable currents can be obtained for small overpotential values. A plot of i_k *vs* η_k yields the values of i_0.

For slow reactions, large overpotentials (η_k < -100 mV) are required to measure any significant current. At large overpotential, $e^{\alpha_b f\eta} \ll e^{-\alpha_f f\eta}$, and Equation (2.13) reduces to Tafel equation as,

$$i_k = -i_0 e^{-\alpha_f f\eta_k} \tag{2.15}$$

or

$$\eta_k = \frac{RT}{\alpha_f F}\ln i_0 - \frac{RT}{\alpha_f F}\ln i_k \tag{2.16}$$

A plot of $\ln(i_k)$ *vs* η_k yields the values of i_0 and α_f.

During an electrochemical reaction the surface concentration of the electroactive species may deviate significantly from bulk concentration due to mass transfer limitation of the electroactive species from bulk to reaction surface. The measured current is then influenced by the magnitude of diffusion controlled current. Butler-Volmer Equation (2.13) accounting for these influence then becomes [45],

$$\frac{i}{i_0} = \left(1 - \frac{i}{i_{L,a}}\right)e^{\alpha_b f\eta_k} - \left(1 - \frac{i}{i_{L,c}}\right)e^{-\alpha_f f\eta_k} \tag{2.17}$$

where $i_{L,a}$ and $i_{L,c}$ are the anodic and cathodic limiting current, respectively.

2.1.4 Butler-Volmer equation with adsorption

Many multistep reactions proceed with one or more adsorbed intermediates and overall reaction rate is influenced by coverage of these intermediates. Depending on whether the rds is adsorption or desorption, the rate may be proportional to either free surface $1-\theta$, or proportional to blocked surface θ.

$$\frac{i}{i_0}=\left(1-\frac{i}{i_{L,a}}\right)(1-\theta)e^{\alpha_b f\eta_k}-\left(1-\frac{i}{i_{L,c}}\right)\theta e^{-\alpha_f f\eta_k} \tag{2.18}$$

2.2 *Electrochemical techniques*

2.2.1 Chronoamperometry

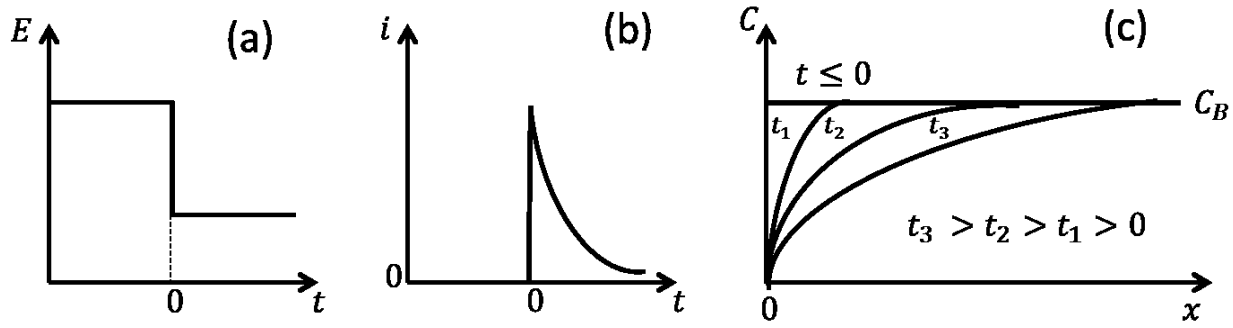

Figure 2.1 Potential, current and concentration profile for a chronoamperometric experiment: **(a)** step input of potential **(b)** current response with respect to time for a step input of potential **(c)** concentration profile with respect to distance away from electrode, C_B represents bulk concentration.

In a chronoamperometric experiment the current obtained from stationary electrode in an unstirred solution is recorded with respect to time in response to step input of potential as depicted in Figure 2.1(a)&(b). When the potential step is large enough, then the current is totally controlled by mass transfer of electroactive species as it is limited by the rate at which the electroactive species arrives at the electrode. In such experiments the concentration at the electrode surface is zero leading to the continued flux of electroactive species towards the electrode. This results in formation of electroactive species depletion zone near the electrode which thickens with time as depicted in Figure 2.1(c). The thickness of this zone is referred as diffusion layer. The diffusion length, given as $\delta = (Dt)^{0.5}$ is the distance from the electrode where the concentration gradient at time t ceases

to zero. For example, for $D = 10^{-5}$ cm$^2 \cdot$ s^{-1} and $\delta = 5$ μm, t is 0.025 s; below 0.025 s the diffusion length is less than 5 μm.

For a planar electrode such as GC disk and Pt disk the diffusion controlled current response for a step input of potential in an unstirred solution is given by Cottrell equation [46],

$$i_L(t) = \frac{nFAD^{1/2}C_B}{\pi^{1/2}t^{1/2}} \tag{2.19}$$

The current given by Cottrell equation is faradic current, however in real experiment there exists always a non-faradic charging current due to charged double layer which flows for short times. The charging current decays exponentially and becomes negligible after five times the time-constant, $5R_uC_d$, where R_u is uncompensated resistance and C_d is charge double layer capacity. To apply Cottrell equation, either the data after five time constants is considered or chronoamperometry is performed in the absence of electroactive species and subsequently subtracted from chronoamperometric curve in presence of electroactive species.

For many experiments the area, A used in Cottrell equation is geometrical area of the electrode. However this depends on the time scale of the experiment. The difference between the magnitude of the roughness factor and diffusion layer thickness becomes an important criterion for determining the area to be used in Cottrell equation. When the roughness factor is much smaller than diffusion layer thickness, geometric area of the electrode can be assumed as A [47]. In this Thesis, the agglomerate size of most of the catalyst particles deposited on GC is < 1 μm and hence the roughness is approximated to 1 μm. When the diffusion layer thickness has grown to 10 μm, the geometric area can be used in Equation (2.19).

2.2.2 Cyclic voltammetry

Cyclic Voltammetry (CV) is a potentio-dynamic technique; here the potential is cycled linearly at constant rate between two chosen limit potentials (potential window). The rate at which potential varies is usually called as sweep rate or scan rate, υ. When the potential is swept only in one direction then it is called as Linear Sweep Voltammetry (LSV).

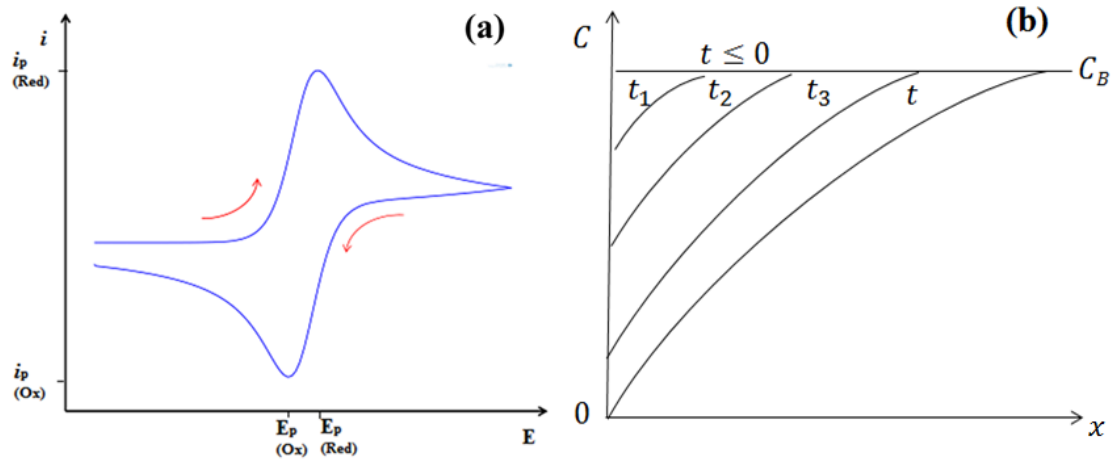

Figure 2.2 (a) Typical cyclic voltammogram for a redox couple in solution: **(b)** Concentration profile with respect to time from the starting potential to peak potential in forward scan.

Figure 2.2 (a) shows a characteristic cyclic voltammogram for a redox couple in a liquid electrolyte. When the potential of the working electrode is swept in the anodic direction, the current starts to increase at a potential which represents the reversible potential of the redox couple. As the potential becomes more positive, the current increases and attains a maximum value, i_L at the peak potential and then decreases. As the sweeping direction of potential is reversed, the current is replicated with an opposite sign (cathodic current). During the forward scan the surface concentration changes continuously from bulk concentration until it becomes near to zero at limiting current. The schematic of concentration profile is shown in Figure 2.2 (b). The surface concentration changes from bulk concentration at $t \leq 0$ to zero concentration at t. Once the measured current at time t is equal to i_L (peak current) then it drops according to Cottrell equation until the growing diffusion layer is perturbed by natural convection. Practically for a stationary electrode in an unstirred solution this perturbation occurs at times greater than 10 s [48] [49], at which point onwards the current fluctuates and Cottrell behavior is lost. Hence the scan rate is usually set in such a manner that the measurement is finished before the diffusion layer has grown substantially. If the purpose of the measurement is to determine i_k which can be represented in terms of bulk concentration then measurements are carried out at the maximum scan rate possible, since at short times the surface concentration is close to bulk concentration (see Figure 2.2 (b)). However the upper limit of scan rate is set to have negligible effect of charging current, $i_c = C_d \cdot (dV/dt)$. This is especially important when the current density to be measured is in the low range. Hence the scan rate generally falls

between 5 - 100 mV · s^{-1} for vast majority of the cyclic voltammetric experiments found in literature.

In this Thesis, the Electrochemically Active Surface Area (ECSA) and C_d of Pt or Pt/C is determined by conducting CV in N_2 saturated electrolyte. ECSA of Pt or Pt/C can be estimated from determining charge required to desorb/absorb monolayer of H_2 on Pt surface. Figure 2.3 represents a typical cyclic voltammogram of Pt/C in 0.1 M KOH aqueous solution measured at a scan rate of 50 mV · s^{-1} over a potential window of -0.85 V to 0.25 V *vs* MMO. The CV can be divided into 3 regions in positive direction scan, H_2 desorption region, charge double layer region and PtOH/PtO formation region. On scanning the potential in the positive direction, adsorbed hydrogen on the Pt surface gets desorbed by an anodic reaction, $Pt - H_{ad} \rightarrow Pt + H^+ + e^-$ at lower potential values, with two peaks corresponding to activity of different crystalline planes of Pt. In charge double layer region, the only charge flow is due to double layer charging. From this region C_d can be determined. Further, at higher potential values, Pt surface undergoes oxidation to form PtOH as $Pt + OH^- \rightarrow Pt - OH + e^-$ and then PtO as $Pt - OH + OH^- \rightarrow Pt - O + H_2O + e^-$. In the reverse scan, at higher cathodic potential PtO reduces back to Pt followed by hydrogen adsorption on the surface of Pt at lower cathodic potential as, $Pt + H_2O + e^- \rightarrow Pt - H_{ad} + OH^-$. This reaction is followed by evolution of hydrogen as $2H_2O + 2e^- \rightarrow H_2 + 2OH^-$ which can be re-oxidized on reversing the potential.

From this cyclic voltammogram, the total charge required for hydrogen adsorption and desorption on the surface of Pt can be measured by integrating the area (shown by hashed area in Figure 2.3) under the respective curves, followed by normalizing with respect to scan rate. Using this integrated charge, Q_C, electrochemical surface area of Pt can be obtained from the following equation assuming a charge value of 2.1 · 10^{-4} C · cm^{-2} for a monolayer adsorption of H_2 on a smooth Pt surface [50].

$$ECSA = \frac{Q_C}{2 \cdot (2.1 \cdot 10^{-4}\text{C} \cdot \text{cm}^{-2}) \cdot A \cdot L_{Pt}} \tag{2.20}$$

where Q_C is in Coulombs, A is the geometric area of the electrode in cm^2 and L_{Pt} is the Pt loading in mg · cm^{-2}.

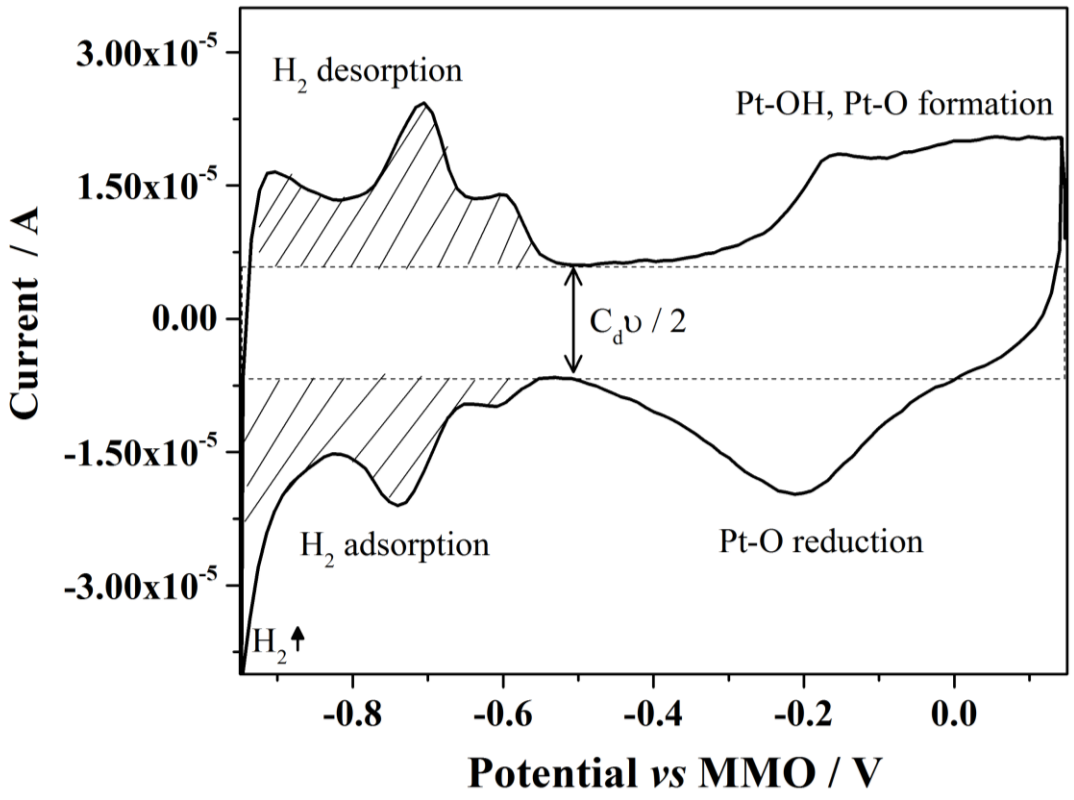

Figure 2.3 Characteristic cyclic voltammogram of Pt/C in 0.1 M KOH aqueous electrolyte saturated with N_2, with a scan rate of 50 mV · s^{-1}.

2.3 *Experimental*

The experimental section includes the procedure of electrode preparation for RDE set–up and fuel cell. Apart from this, the results of some preliminary studies aimed to investigate the electrochemical stability of ionomer are also discussed.

2.3.1 *Electrode preparation for RDE setup*

2.3.1.1 Catalyst ink

The catalyst ink was prepared by adding 51.7 mg of 60 wt. % Pt/C (Alfa Aesar, United Kingdom) into 40 mL of deionized water (Millipore, 18.2 MΩ .cm) followed by ultra-sonication for 20 minute in an ice bath and dilution to obtain 1.96 μg_{Pt} in 20 μL of volume. This suspension was ultra-sonicated each time in an ice bath for 10 min before dropping 2 - 20 μL ink with micro pipette on GC surface in order to obtain a loading of 1 to 24 $\mu g_{Pt} \cdot cm^{-2}_{disk}$. The catalyst was dried at ambient conditions. The volume to be dropped on GC

was kept to maximum 20 μL. When desired loading was not reached additional ≤ 20 μL was dropped consecutively after the previous coating was dried.

Another set of catalyst ink was prepared in isopropanol (Sigma-Aldrich, Germany) – water solution (isopropanol : water = 99:1) using the same procedure described above. A 10 μL aliquot of this solution was dropped on GC surface in order to obtain a loading of ~ 8 $\mu g_{Pt} \cdot cm^{-2}{}_{disk}$. For higher loadings, additional 10 μL was dropped consecutively after the previous coating was dried.

The area of GC used for measurements at 22 °C was 0.247 cm^2 whereas for measurements made at 60 °C it was 0.196 cm^2. The microscopic images of the catalyst coated GC were taken by optical microscope (Model DFC450C) supplied by Leica Microsystems, Switzerland.

2.3.1.2 Ionomer film

Commercially obtained AS-4 ionomer solution (5 wt. % solids in isopropanol) procured from Tokuyama Corp., Japan was accordingly diluted in water in order to obtain ionomer films of thicknesses 1, 2, 3 and 5 μm on catalyst coated GC by dropping 10 μL of ionomer solution. The density of recast ionomer film was assumed to be the same as A201 membrane (ρ = 1.06 $g \cdot cm^{-3}$) supplied by Tokuyama Corp., Japan.

2.3.2 *Electrochemical measurements in RDE set-up*

A standard three electrode RDE set up ((Model 636) and glass (Corning 7740 borosilicate) electrochemical cell procured from Pine Instruments was used for all electrochemical measurements. MMO (Belltec, Germany) was used as reference electrode. Pt mesh was used as counter electrode and catalyst coated GC disk or Pt disk as working electrode. The electrochemical measurements were performed in 0.1 M KOH at temperature 22 ºC or 60 ºC and atmospheric pressure. ORR voltammograms, impedance, cyclic voltammogram and chronoamperometric curves were measured by using an IM6e Potentiostat procured from Zahner GmbH, Germany. High frequency impedance measurements at 10 kHz were also carried out prior to each electrochemical measurement to determine uncompensated electrolyte resistance, R_u. The obtained values were in the range of 31±1 Ω at 22 °C and 20±1 Ω at 60 °C. Cyclic voltammetric measurements were performed at a scan rate of 50 $mV \cdot s^{-1}$ in N_2 (grade 5.0 Westfalen AG, Germany) saturated electrolyte. All cyclic

voltammograms are base corrected and base cyclic voltammetry was performed on bare GC at similar operating conditions. The ORR voltammograms were measured at a scan rate of 10 mV · s^{-1} with 300 - 3600 rpm in O_2 saturated electrolyte. The chronoamperometry was performed in O_2 saturated electrolyte at non-rotating catalyst coated GC disk. To account for contribution from double layer charging current, chronoamperometry is also performed in N_2 saturated electrolyte and subsequently subtracted from O_2 saturated chronoamperometry curve.

2.3.3 Working electrode stability and reproducibility

Preparation of WE involves coating of catalyst on GC and then coating the catalyst layer with ionomer for binding the catalyst to GC. Before reliable measurements can be made, following criteria must be met:

a) To ensure reproducibility in electrochemical measurements the GC should be uniformly coated with catalyst particle with agglomerate size as low as possible.

b) Binder should be electrochemically stable and not contain any impurities which can act as inhibitor for catalyst activity

c) Binder should not degrade in the time scale of the experiment.

In the following sections these criteria are evaluated experimentally.

2.3.3.1 Catalyst distribution on glassy carbon

It is of utmost importance that the catalyst distribution on GC should be uniform and reproducible while evaluating the catalyst activity [51]. Preferably, the catalyst agglomerate size should be as low as possible for better catalyst utilization, so that accurate and reproducible current values are obtained. Monitoring the catalyst drying on GC surface using a microscope from the time of catalyst ink dropping until drying, gives insight into the factors leading to non-uniform catalyst distribution. As soon as the ink is dropped on GC, the catalyst particles move randomly inside the droplet. This Brownian like motion was seen to be faster in isopropanol, whereas in water it is much slower. Faster moving particles accompanied with higher collision force was usually found either to dislodge the smaller agglomerates stuck previously on GC or cling to only bigger agglomerates. As a result, the catalyst distribution after drying differs for isopropanol and

water as solvent. Figure 2.4 shows the microscopic images of catalyst distribution on GC surface for isopropanol and water as solvent. The white background in the images is GC surface and black specks are Pt/C particles. The images were taken after drying of each consecutive coating of catalyst in steps of 8 $\mu g_{Pt} \cdot cm^{-2}$, at the same location in order to trace the growth of agglomerates. For water as the solvent the catalyst is uniformly distributed with very few agglomerates and the best coating is reached when the loading was kept at or below ~ 16 $\mu g_{Pt} \cdot cm^{-2}$ (Figure 2.4 (a-b)) with most of the particles size below 1 μm. For higher loadings the particles start agglomerating and occurrence of agglomerates > 5 μm increases rapidly (Figure 2.4(c)). For isopropanol, the distribution is significantly non-uniform and bigger agglomerates are found even with 8 $\mu g_{Pt} \cdot cm^{-2}$ (Figure 2.4(d-f)). In case of isopropanol, a significant number of agglomerates grow in size at the same location during drying and when the loading is increased from 8 to 24 $\mu g_{Pt} \cdot cm^{-2}$ (indicated by circles in images d-f). In most of the literature, the loading of catalyst particles when using water as solvent varies between 10 - 50 $\mu g_{Pt} \cdot cm^{-2}$. Although the diffusion limited current is only marginally affected for loading of 10 - 50 $\mu g_{Pt} \cdot cm^{-2}$, the best mass activity values at low overpotential are obtained when loading is kept below 20 $\mu g_{Pt} \cdot cm^{-2}$ [52] [53] [54]. This is justified in this work by the microscopic images.

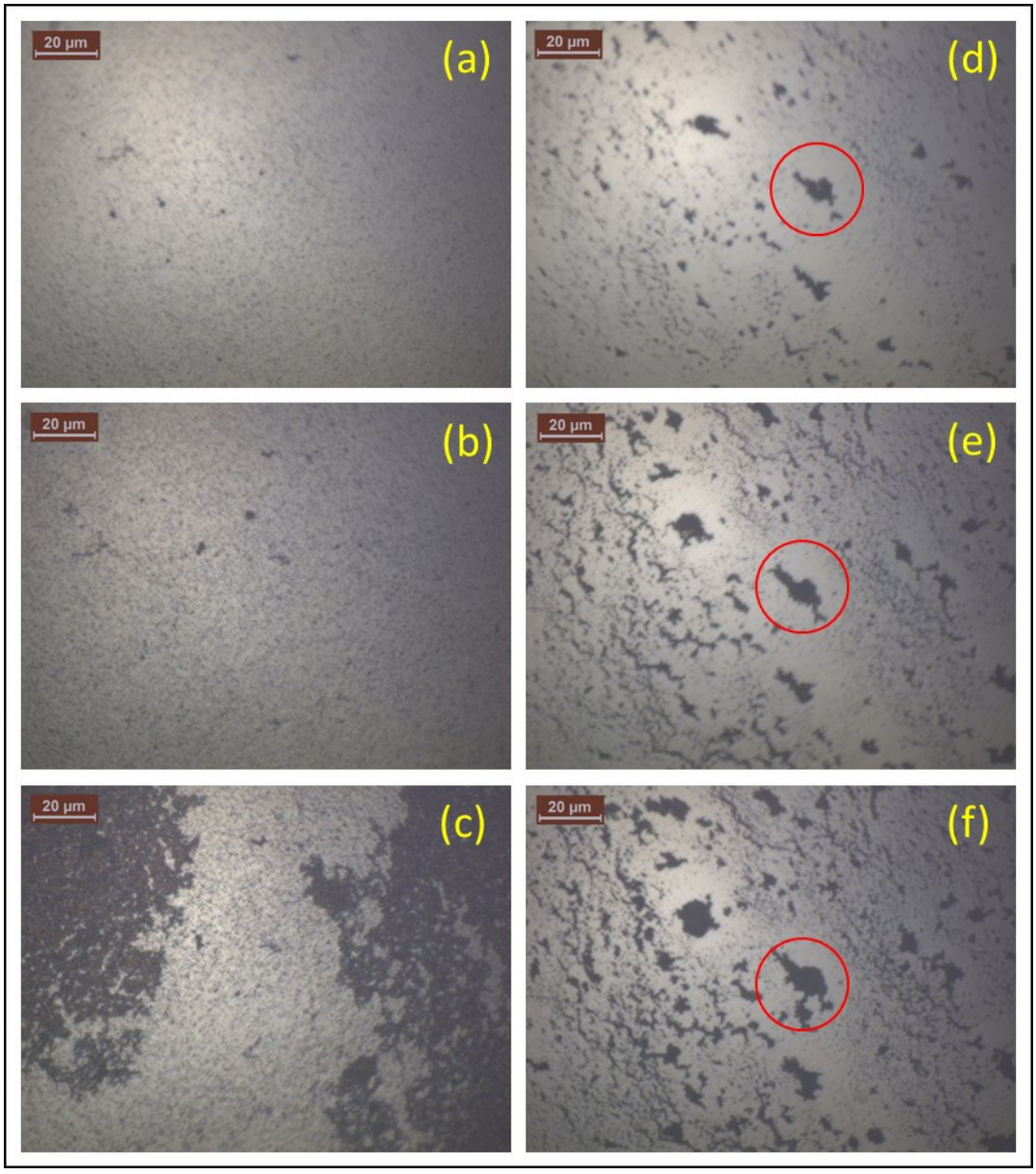

Figure 2.4 Microscopic pictures of catalyst distribution on GC surface: water as solvent for loading of (a) 8 $\mu g_{Pt} \cdot cm^{-2}$ (b) 16 $\mu g_{Pt} \cdot cm^{-2}$ (c) 24 $\mu g_{Pt} \cdot cm^{-2}$; isopropanol as solvent for loading of (d) 8 $\mu g_{Pt} \cdot cm^{-2}$ (e) 16 $\mu g_{Pt} \cdot cm^{-2}$ (f) 24 $\mu g_{Pt} \cdot cm^{-2}$.

2.3.3.2 Impurities in ionomer

Figure 2.5 shows the CV of GC electrode coated with Pt/C and 1 μm ionomer film. Here the current obtained is normalized with respect to the ECSA of Pt evaluated as described in Section 2.2.2 The obtained CV is a characteristic CV of Pt/C catalyst suggesting that ionomer is electrochemically inactive in the potential window of CV measurement. It shows the typical Pt-H adsorption/desorption region, double-layer region, and Pt-oxide region similar to that reported previously for Pt in alkaline media [37].

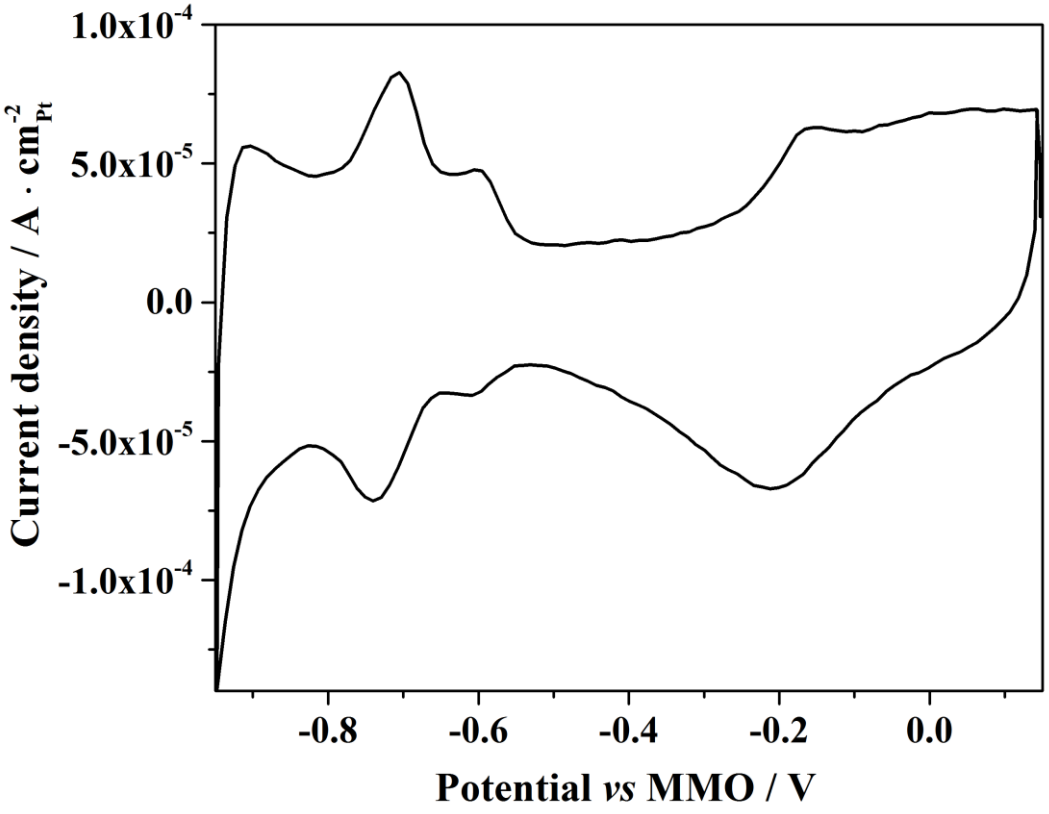

Figure 2.5 Cyclic voltammogram for Pt/C coated on GC with 1 µm ionomer film measured at a scan rate of 50 mV · s^{-1} in N_2-saturated 0.1 M KOH at 22 °C.

2.3.3.3 Ionomer degradation

Short term durability studies of AS-4 ionomer film were carried out by measuring ORR voltammograms for 1000 cycles. For this study, 5 μm film of AS-4 ionomer was coated on Pt disk instead of using Pt/C coated GC. This allows to exclude degradation or agglomeration of catalyst layer while cycling. Also, cyclic voltammetric measurements under N_2 atmosphere were conducted before and after durability test.

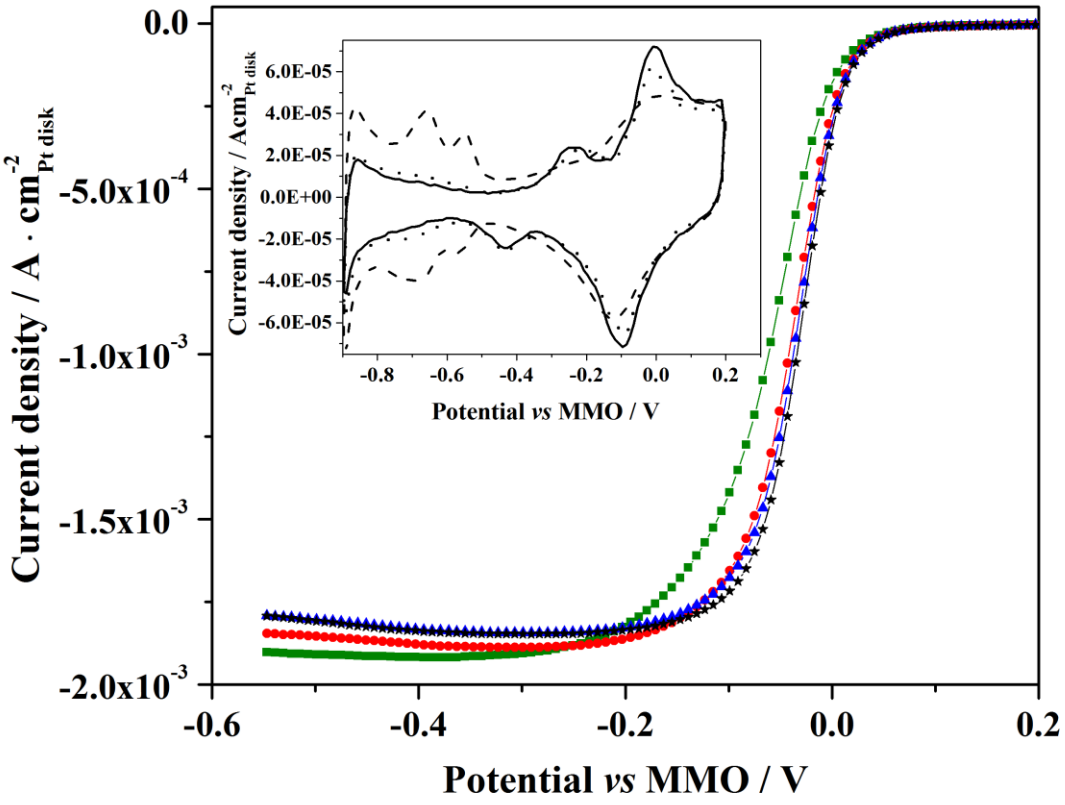

Figure 2.6 ORR voltammograms (10 mV · s^{-1}) and CVs (50 mV · s^{-1}) of Pt disk coated with 5 µm ionomer film measured in 0.1M KOH before and after ageing by cycling. ORR after 10^{th} (square), 300^{th} (circle), 600^{th} (triangle), and 1000^{th} (star) cycles. Inset: CV under N_2 saturated electrolyte before 1000 cycles (dashed line), after 1000 cycles (solid line), after removing ionomer (dotted line).

Figure 2.6 shows the ORR voltammogramms for various numbers of cycles for ionomer coated on polycrystalline Pt disk electrode consisting of Pt (111), Pt (100) and Pt (110) crystalline planes. It can be seen that the current improves in the activation region whereas it decreases in the limiting region. An explanation for improved activity is provided by cyclic voltammograms under N_2 atmosphere. Inset shows cyclic voltammetric measurements in N_2 saturated electrolyte for Pt disk for three cases 1) Pt disk before 1000 ORR cycles 2) Pt disk after 1000 ORR cycles and 3) Pt disk after removing of ionomer film. It is clear that the cyclic voltammograms of case 2 and 3 are similar and are very different from case 1. The cyclic voltammogram in case 1 resembles more to typical cyclic voltammogram of polycrystalline Pt, but cyclic voltammograms of case 2 and 3 resembles

to cyclic voltammogram of Pt (111), [55] suggesting that after 1000 ORR cycles, Pt (111) is predominantly exposed more than other planes. Since Pt (111) plane is more active for ORR [55] in relation to other planes, we see an increase in the current in the activation region during ORR cycling. The cyclic voltammetric results support the previous findings [56] that the active sites of Pt disk undergo reorientation while cycling. The decrease in current in the limiting region is ascribed to delamination of film from Pt disk during cycling which can increase the diffusion thickness and hence decreases the limiting current. This shows that AS-4 AEI is electrochemically stable during ORR cycling in alkaline media and deviations in ORR voltammogram is only caused by changes in Pt disk morphology and ionomer delamination.

2.3.3.4 Impurities from glass electrochemical cell

Studies have pointed out that impurities arising from dissolution of glass in alkaline electrolyte may affect ORR curves on Pt electrode [57] [58]. In their study following steps were followed:

1. CV/ORR measurements in Teflon cell on Pt disk in 0.1M KOH for 3 h.
2. Addition of Duran glass piece to the Teflon cell and repeated scanning (CV/ ORR) between 0.05 to 0.5 V *vs.* RHE for 25 minutes.
3. Measurement of CV/ ORR between 0.05V to 1V *vs.* RHE (1 scan)
4. Measurement of CV/ ORR between 0.05V to 1.5V *vs.* RHE (3 scans)

The authors claimed (no curves shown) stable CV in Ar saturated electrolyte and ORR measurements in step1. That is the H_{upd} peaks (the peaks obtained between -0.8V to -0.55V in Figure 2.3) did not change and the ORR activity stayed constant over whole time the cell was in operation. In step 3, H_{upd} peaks in CV were suppressed and diffusion limited current in ORR curves did not stay constant below 0.5V *vs.* RHE. However after completion of 4^{th} step the curves returned to original values as obtained in step1. The authors attributed the anomalies observed in step 3 from single scan to impurities from glass and concluded that for measurement of true activity of ORR, Teflon cell should be used. However the authors did not present the results with all steps for Teflon cell without glass piece for comparison purposes. On the contrary Subbaraman *et al.* [59] showed that suppression of H_{upd} peaks in CV can also be seen in Teflon cell when measured for sufficiently long time for example 100 cycles. They argued that, change in curves over a

long time is largely due to the adsorption of trace impurities like transition metal oxides and sulfides inherent to electrolyte and not from the impurities of glass. Furthermore considering the often need of activating electrode [60] [61] to obtain reproducible behavior, the conclusions that the changes in CV and ORR from single scan are caused by impurities from glass presently seems to be premature.

In this thesis the influence of impurities from glass if any, has been ignored as we obtained good and reproducible results even by using glass electrochemical cell. As can be seen from Figure 2.6 the ORR activity do not show any significant deviations between 300th cycle and 1000th cycle even though the time elapsed between these scans is ~29 h. In addition we also obtained excellent repeatability between the ORR curves (see Figure 4.6) as discussed in section 4.1.3.1.

2.3.4 Preparation of fuel cell MEAs

Two types of fuel cell MEAs with an active area of 4 cm^2 were prepared, Type-1 with various low anode and cathode catalyst loadings and Type-2 with high anode and cathode catalyst loadings. For all MEAs the ionomer loading in CL was 40 wt. % with respect to Pt/C.

Type1 MEAs were prepared by spray coating the required amount of catalyst ink on A201 membrane (Tokuyama Corp Japan) or Nafion-115 membrane (QuinTech Germany) maintained at 65 °C. The catalyst loadings were between 0.07 $mg_{Pt} \cdot cm^{-2}$ to 0.16 $mg_{Pt} \cdot cm^{-2}$. Typical catalyst ink was prepared by sonicating the mixture comprised of 50 mg Pt/C (60 wt. % Pt, Alfa Aesar, United Kingdom), 250 µL deionized water (Millipore, 18.2 MΩ · cm), 30 mL isopropanol (Sigma-Aldrich, Germany), 500 µL AS-4 ionomer solution (5 wt. % solution, Tokuyama Corp. Japan) or Nafion ionomer solution (5 wt. % solution, QuinTech Germany). Since the weight difference between the bare membrane and catalyst coated membrane were < 0.3 mg for some MEAs, difficulties were encountered for measuring the weight difference. This difficulty arose from the changing weight of catalyst coated membrane with time as the membrane slowly cooled to ambient temperature right after removing it from the spray set up maintained at 65 °C. To avoid this, the catalyst coated membranes were allowed to equilibrate with the ambient temperature for at least 15 min before measuring the weight.

Similar ink composition was used for Type-2 MEA except the amount of isopropanol was 15 mL. For preparation of Type-2 MEA the catalyst ink was brush coated onto two gas diffusion layers, GDL 35BC (SGL Tech. GmbH, Germany) and hot pressed together with A201 membrane at 100 °C at 6 N · mm^{-2} for 3 min. Gas diffusion layer GDL 35BC is a teflonsied (5wt. %) carbon paper coated with macro porous layer. For preparation of inert layer MEA (IL-MEA) of Type-2 all the conditions were same except an additional layer comprising of 50% carbon (wt. %) and 50% AS-4 (wt. %) ionomer were brush coated on cathode GDL after coating CL. Schematic representation of Type-2 MEA and IL-MEA are shown in Figure 2.7. The thickness of bare GDL, catalyst coated GDL, catalyst and inert layer coated GDL were measured by digital micrometer from Mitutoyo Japan after hot pressing at similar conditions described above for MEA preparation. The average thickness was determined by averaging the thickness measured at 5 different locations.

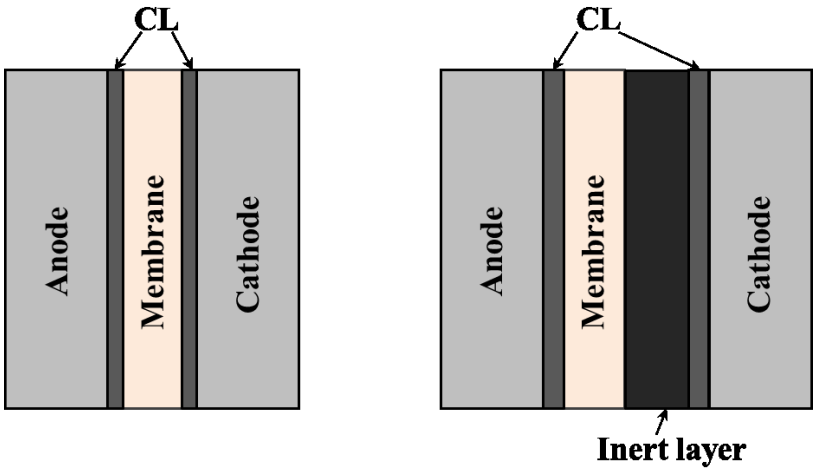

Figure 2.7 Schematic representations of **(left)** Type 1 and Type-2 MEA and **(right)** IL-MEA.

As shown by Weinzierl *et al.* [40] high stoichiometries of humidified Air/O_2 are required for sufficient supply of H_2O for the ORR at the cathode. Therefore humidified (80% RH) H_2 and O_2 were supplied at 60 °C to the fuel cell employing Type-1 and Type-2 MEAs at high stoichiometry values of 18 for H_2 at the anode and 36 for O_2 (which is equivalent to stoichiometry 4 for H_2O) at the cathode for 1 A · cm^{-2}. The high flow rates at anode also aid in avoiding water flooding at anode. The high frequency resistance of complete AMFC as measured by impedance spectroscopy technique is assumed as membrane resistance neglecting the usually small electrical resistance in the electrode and

setup. Measured values of high frequency resistance at 10 kHz with 10 mV amplitude were ~ 0.2 $\Omega \cdot cm^{-2}$ for all the AMFC MEAs and ~ 0.15 $\Omega \cdot cm^{-2}$ for all PEMFC MEAs.

Chapter 3
Mass Transport Losses[3]

During an electrochemical reaction the depletion of reactants in a MEA near the CL causes a flux of reactant from flow field to CL via GDL. The rate of flux depends on the mass transfer coefficient of gases in GDL. Here, the mass transfer coefficient is the ratio of diffusion coefficient to the diffusion layer thickness. To obtain high power from fuel cells, large mass transfer of gases is desired. Poor mass transfer of gases through GDL can cause large overpotential affecting the currents even in kinetic region. In AMFC the mass transfer limitations can arise from flow of H_2, O_2 and H_2O, whereas in PEMFC it arises from flow of, H_2 and O_2. Apart from this, at high currents the inefficient product removal can cause mass transfer limitations arising from excessive water formation at anode of AMFC and in cathode of PEMFC. However these effects can be neglected at low to medium currents. Moreover, since very high stoichiometric values of reactant gases were supplied to fuel cell in every experiment (see section 2.3.4), the concentration of reactant gases throughout the flow field channel are assumed constant.

3.1 *Hydrogen, oxygen and water transport limitations in AMFC and PEMFC*

The diffusion limitation at AMFC can arise from mass transfer limitation of H_2, O_2 and H_2O from flow channel to CL via GDL(carbon paper + macro porous layer). While H_2

[3] Part of the results in this Chapter published in P.S. Khadke, U. Krewer, *J. Phys. Chem. C*, 118 (**2014)** 11215-11223.

and O_2 transport occurs mainly from flow channel to CL via GDL, H_2O can transport from anode CL to cathode CL via membrane by diffusion and cathode CL to anode CL via membrane by electro-osmotic drag. From Fick's first law of diffusion, the limiting current arising from H_2, O_2 and H_2O diffusional resistance in GDL can be represented as,

$$i_{L,H_2} = 2FAD_{GDL,H_2}C_{H_2}/L_{GDL} \tag{3.1}$$

$$i_{L,O_2} = 4FAD_{GDL,O_2}C_{O_2}/L_{GDL} \tag{3.2}$$

$$i_{L,H_2O} = 2FAD_{GDL,H_2O}C_{H_2O}/L_{GDL} \tag{3.3}$$

where L_{GDL} is the thickness of GDL; D_{GDL,H_2}, D_{GDL,O_2} and D_{GDL,H_2O} are the diffusion coefficient of H_2, O_2 and H_2O through GDL; C_{H_2}, C_{O_2} and C_{H_2O} are the concentrations of H_2, O_2 and H_2O in the flow field channel. Apart from the number of H_2O molecules required for the cathodic reaction, i_{L,H_2O} should also account for electro osmotic water drag from cathode to anode. Assuming 4 molecules of H_2O are dragged from cathode to anode for every OH^- [62] [63] produced, the effective number of H_2O molecule lost at the cathode is 4.5 for every one electron transfer and hence the limiting current arising from water diffusion resistance in GDL becomes,

$$i_{L,H_2O} = \frac{\frac{2}{9}FAD_{GDL,H_2O}C_{H_2O}}{L_{GDL}} \tag{3.4}$$

Equation (3.4) changes further when water back transport from anode CL to cathode CL via membrane is incorporated. However as it will be shown later that water back transport is negligible when no liquid water is present in the anode CL, for now Equation (3.4) is considered for further calculations. When the anodic and cathodic gas is humidified to 80% RH at 60°C, C_{H_2O} is 5.25 times lower than C_{H_2} and C_{O_2}. Comparing Equation (3.1), (3.2) and (3.4) it can be seen that $i_{L,H_2O} << i_{L,H_2}$ and $i_{L,H_2O} << i_{L,O_2}$. Therefore it is reasonable to neglect the effect of i_{L,H_2} and i_{L,O_2} and assume that overall limiting current in AMFC is nearly equal to i_{L,H_2O} as defined in Equation (3.4). For determining i_{L,H_2O} from Equation (3.4) D_{GDL,H_2O} and A should be known. D_{GDL,H_2O} is the effective diffusion coefficient of water in oxygen as there is no other medium present in the cathodic gas and can be calculated as follows [64],

$$D_{GDL,H_2O} = D_{H_2O-O_2}\frac{\varepsilon}{\tau} \tag{3.5}$$

where ε is porosity and τ is tortuosity of GDL. Inserting $D_{H_2O-O_2}$= 0.318 $cm^2 \cdot s^{-2}$ [65] [66] [67], τ=2.5 [64] [68] and ε= 0.526 [68], D_{GDL,H_2O} is calculated as 0.067 $cm^2 \cdot s^{-1}$. The value of area A in Equation (3.4) is equal to the geometric area of the CL where water is being transported when the cell current is mass transfer limited. This value is not straight forward to calculate and depends on the reaction zone which varies with current being drawn from the fuel cell. Reactants are transported from flow channel to CL via GDL; due to the large transport distance under the rib compare to GDL thickness, the reactant may not reach some parts of catalyst layer under the rib area. The simulation results by many research groups [69] [70] [71] [72] have shown that local current density under rib area reduces with increasing overall current density and goes near to zero at current densities nearing to mass transfer limited current density (Figure 3.1(left)). However, at low overall current density the local current density is uniform in all regions (Figure 3.1(right)). This suggests that at low current catalyst layer under channel and rib area is utilized whereas at current limited by mass transfer, the reaction essentially happens in the catalyst layer under the channel. Therefore the effective A can be assumed as channel area. It may happen that reaction zone at cathode CL may shift little due to the interaction from anode reaction zone, however since $i_{L,H_2O} << i_{L,H_2}$ the likelihood of this is low. The channel area and rib area of flow field used here is 2.19 cm^2 and 1.8 cm^2 respectively. Substituting A = 2.19 cm^2, D_{GDL,H_2O} = 0.067 $cm^2 \cdot s^{-1}$, C_{H_2O}= 5.7 · 10^{-6} mol · $cm^{-3}$and L_{GDL}= 0.03 cm, the calculated i_{L,H_2O} from Equation (3.4) is equal to 0.6 A. The water concentration, C_{H_2O}= 5.7 · 10^{-6} mol · cm^{-3} is the concentration of water in oxidant gas at 60 °C when humidified to 80 % RH. The limiting current value obtained here is quite low in comparison to limiting current values obtained at PEMFC. Such low values of limiting current suggest that mass transfer limitations are expected to start already at low overpotential.

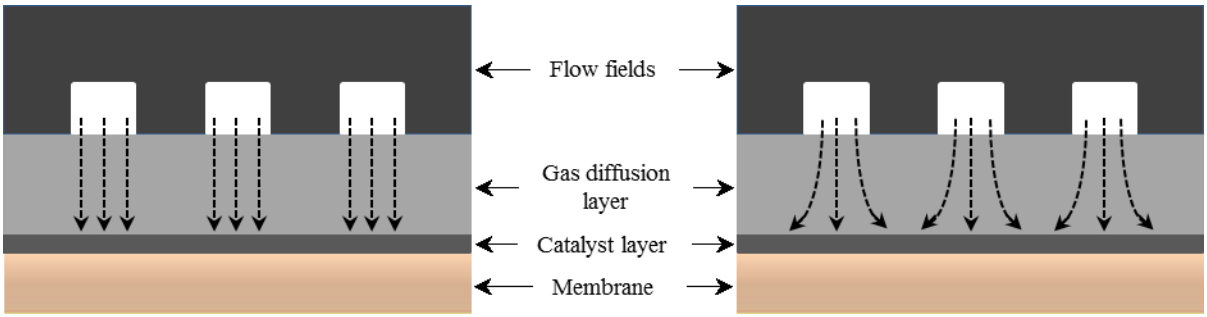

Figure 3.1 Schematic representation of water transport from flow channel to CL via GDL: **(left)** current is diffusion limited; and **(right)** current is low for instance in kinetic region.

In an operating AMFC, the back transport of water from anode CL to cathode CL through membrane can also act as source of water for the cathodic reaction. In Equation (3.4) the back transport of water from anode to cathode is not considered. For calculating water back transport, diffusion coefficient of water through membrane, D_{m,H_2O}, is required. D_{m,H_2O} is found by building a set up shown in Figure 3.2. In this experiment, the anode and cathode flow-field is separated by membrane. Water is passed on the anode side and dry air is passed on the cathode. Dry air picks up the water diffusing through membrane and passes over humidity sensor via heated cathode outlet tube. The heating element at the cathode outlet was able to raise the sensing temperature to only 45 °C. This created problem when the cell temperature was 60 °C. Therefore to avoid water condensation, infra-red lamp was used and through which the sensing temperature was maintained successfully between 70 - 80 °C. The amount of water vapor in the cathode outlet is equal to water diffused through membrane from anode to cathode. The amount of water in cathodic gas is found from the dew point temperature (T_d) measured by humidity sensor. From T_d, the partial pressure of water vapor (p_{H_2O}) in cathode outlet gas can be calculated by Antoine equation,

$$log_{10}(p_{H_2O}) = a - \frac{b}{c + T_d} \tag{3.6}$$

where p_{H_2O} is in mmHg, a = 8.071, b =1730.63, c = 233.426 and T_d is in °C. Material balance in cathode stream gives,

$$\dot{n}_{in,Air} = \dot{n}_{out,Air} \tag{3.7}$$

$$\dot{n}_{out,Air} = (p_{N_2} + p_{O_2})\frac{\dot{V}}{RT} = (P_T - p_{H_2O})\frac{\dot{V}}{RT} \tag{3.8}$$

$$\dot{n}_{out,H_2O} = p_{H_2O}\frac{\dot{V}}{RT} \tag{3.9}$$

where $\dot{n}_{in,Air}$ and $\dot{n}_{out,Air}$ are the molar flow of air in mol · s^{-1} at the inlet and outlet of cathode respectively and $\dot{n}_{out,H_2O}$ is the molar flow of water in mol · s^{-1} at the outlet of cathode, $\dot{V}$ is the volumetric flow rate in m^3 · s^{-1}, p_{H_2O}, p_{N_2} and p_{O_2} are the partial pressure in Pa of H_2O, N_2 and O_2 respectively and P_T is total gas pressure equal to 101.3 kPa. By taking ratio of Equation (3.8) and (3.9), $\dot{n}_{out,H_2O}$ can be calculated since $\dot{n}_{in,Air}$ and p_{H_2O} are known.

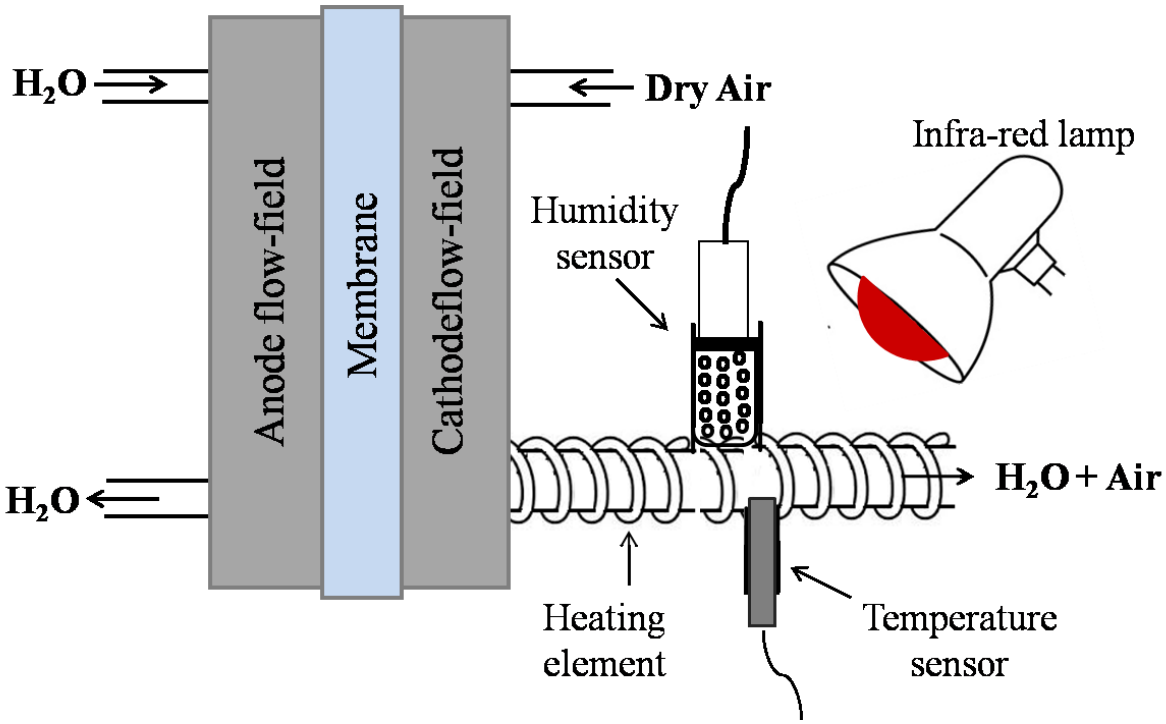

Figure 3.2 Schematic view of the set up constructed for measurement of dew point temperature and relative humidity.

Figure 3.3 (a) shows the H_2O flux diffused across membrane against air flow rate. The results presented are for Tokuyama A201 membrane at 30 °C and 60 °C and Nafion-115 membrane at 60 °C. It can be seen that molar flow rate of water is similar for Tokuyama membrane and Nafion membrane even though the thickness of Nafion

membrane (~ 150 μm) is about five times that of Tokuyama membrane (~ 30 μm). The water transport through Tokuyama membrane is relatively poor and the diffusion coefficient is much lower than that of Nafion membrane as determined from Fick's first law, given as,

$$\dot{n}_{out,H_2O} = AD_{m,H_2O}\frac{(C_{H_2O} - 0)}{L_m} \tag{3.10}$$

where L_m is the thickness of membrane, C_{H_2O} = 0.055 mol · cm^{-3}. A is the effective area for water diffusion through membrane. Depending on the magnitude of lateral diffusion of water in membrane and whether there is water film formed under the rib, the effective area may lie between 2.19 cm^2 and 4 cm^{2}considering channel area and rib area of flow field as 2.19 cm^2 and 1.8 cm^2 respectively. Hence the calculated range of D_{m,H_2O} at 60 °C from Equation (3.10) for Tokuyama and Nafion membrane is 5.25 · 10^{-7} cm^2 · s^{-1} to 9.6 · 10^{-7} cm^2 · s^{-1} and 26.87 · 10^{-7} cm^2 · s^{-1} to 52.8 · 10^{-7} cm^2 · s^{-1} respectively. The value of D_{m,H_2O} found in this study for Nafion membrane compares well with many literature values between 40 · 10^{-7} cm^2 · s^{-1} to 70 · 10^{-7} cm^2 · s^{-1} tabulated by Zhao *et al.* [73]. Considering the range of diffusion coefficient value for Tokuyama membrane and C_{H_2O} = 7 · 10^{-6} mol · cm^{-3} at the anode, the expected current from the back transport of water in AMFC is between 0.515 mA to 1.73 mA as calculated from,

$$i = \frac{2FAD_{m,H_2O}C_{H_2O}}{L_m} \tag{3.11}$$

The water concentration value used in the above equation corresponds to water concentration of a gas at 100 % RH at 60 °C. It should be noted that in practical operating conditions of AMFC the current corresponding to water back transport will depend mainly on water condensation in the anode CL. When the water vapor concentration in anode CL grows beyond 7 · 10^{-6} mol · cm^{-3}, it will condense and water concentration will abruptly change to 0.055 mol · cm^{-3} in some regions of the CL. In this case there may be significantly more diffusion of water from anode CL to cathode CL through membrane and this may aid in improving AMFC performance. For instance when the anode CL is completely flooded with liquid water, the current due to back transport of water is 13.6 A (3.4 A· cm^{-2}). Although, this scenario is good for cathode, it is not desirable in AMFC operation as it blocks the H_2 supply to anode CL.

Until now the mass transfer limitations arising from O_2 and H_2 transport through ionomer film in CL is not considered. When the limitation of O_2 and H_2 transport through ionomer is severe, it might further reduce the limiting current. In the following sections this issue is investigated.

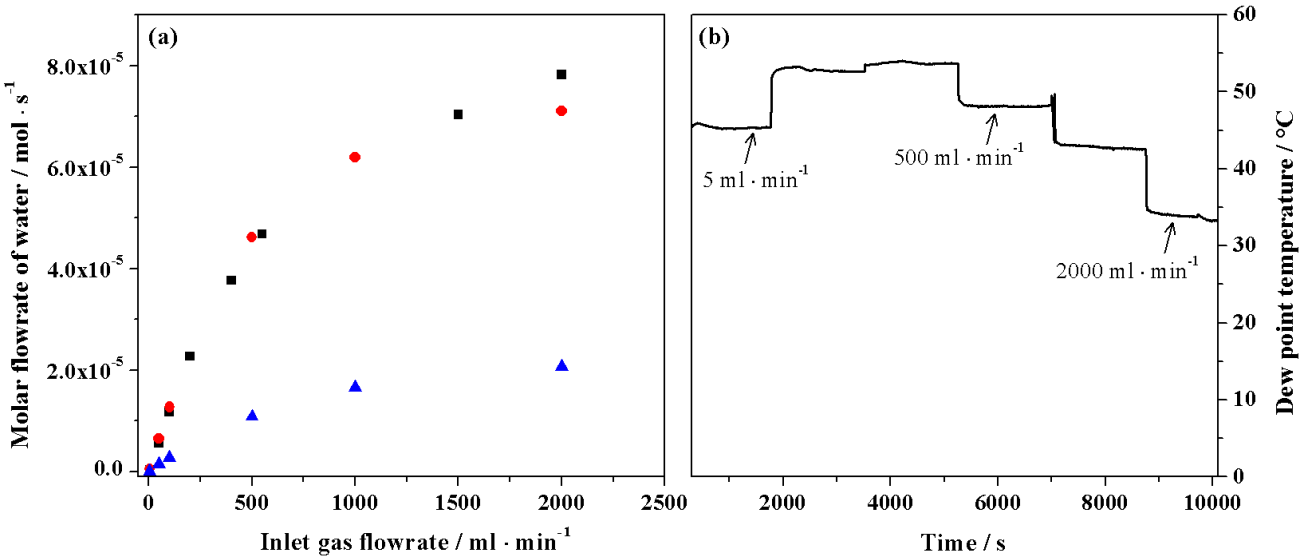

Figure 3.3 (a) Water transport through Tokuyama membrane at 60 °C (circle) and 30 °C (triangle) and Nafion membrane at 60 °C (square); **(b)** Sample data of dew point temperature at various inlet gas flow rate for Nafion-115 membrane at 60 °C.

3.2 *Oxygen transport at Pt/C-anion exchange ionomer interface at RDE*

The CL of fuel cell comprises of ionomer and catalyst, and for a facile mass transport of reactant through the catalyst layer, permeability and diffusion coefficient of the reactant in ionomer should be high. Due to the difficulty of determining these parameters in an ill-defined condition at fuel cell level, in literature these transport parameters for O_2 have been reported in an electrochemical set-up with well-defined conditions. In past, the O_2 transport through Pt/cation-exchange-ionomer [74], Pt/cation-exchange-membrane [75] [76] [77] [78] [79] [80] [81] [82] and Pt/anion-exchange-membrane [79] [83] had been studied. The parameters obtained from these studies assist in determining the mass transfer resistance of O_2 in CL and membrane of fuel cell employing similar ion-exchange ionomer and membrane. The transport parameters are important for modeling of fuel cell and in designing and optimizing fuel cell electrodes.

Most of the earlier studies as shown above were carried out at electrode/membrane interface. The study on electrode/ionomer interface is scarce in literature. The CL of AMFC used in the present study employs commercially available Tokuyama AS-4 anion exchange ionomer. No studies of O_2 transport through Pt/ Tokuyama AS-4 ionomer have been conducted yet. This chapter quantifies the mass transport characteristics of O_2 at Pt/anion exchange ionomer interface by determining the diffusion coefficient and Henry's constant of O_2 in Tokuyama AS-4 anion exchange ionomer film. These parameters are determined at 22 °C and 60 °C, and compared with other values reported in the literature.

To determine these parameters, electrochemical methods such as linear sweep voltammetry on RDE in steady state conditions and chronoamperometry on stationary disk electrode in unsteady state conditions are performed. The diffusion parameters determined from both these methods are compared and correlated.

3.2.1 Effect of ionomer-film thickness

Disk currents at low overpotential values are largely kinetically controlled and at high overpotential diffusion controlled. A requirement for determining diffusion parameters is that the measured current is diffusion controlled. The diffusion controlled current is independent of scan rate and catalyst loading, if the electrode is uniformly coated with catalyst. When diffusion parameters of ionomer film are to be determined then the film thickness should be thick enough to reduce the diffusion controlled limiting current even further. Whereas, while determining the kinetic parameters, the film thickness should be low enough not to limit the kinetically controlled current significantly and high enough to bind the catalyst to the GC. These constraints guides the way electrode is prepared for studying diffusion and kinetic parameters.

Figure 3.4 shows the negative going ORR voltammograms for various film thicknesses at 1600 rpm. It can be seen that i in the limiting current region at < - 0.4 V decreases with increase in the film thickness. However, the curves are identical within experimental error for 1 μm and 0.5 μm thick films. The film of thickness ≤ 1 μm does not cover the CL completely (as the roughness is ~ 1 μm) and is thin enough not to limit the current in all regions of ORR polarization curve. Therefore the mass transfer resistance offered by film to O_2 diffusion can be neglected. These electrodes can be used to determine the kinetic parameters as it will be discussed in Section 4.1. When the film

thickness is ≥ 2 μm, the film offers resistance to O_2 diffusion. These electrodes can be used for calculating O_2 diffusion parameters through ionomer.

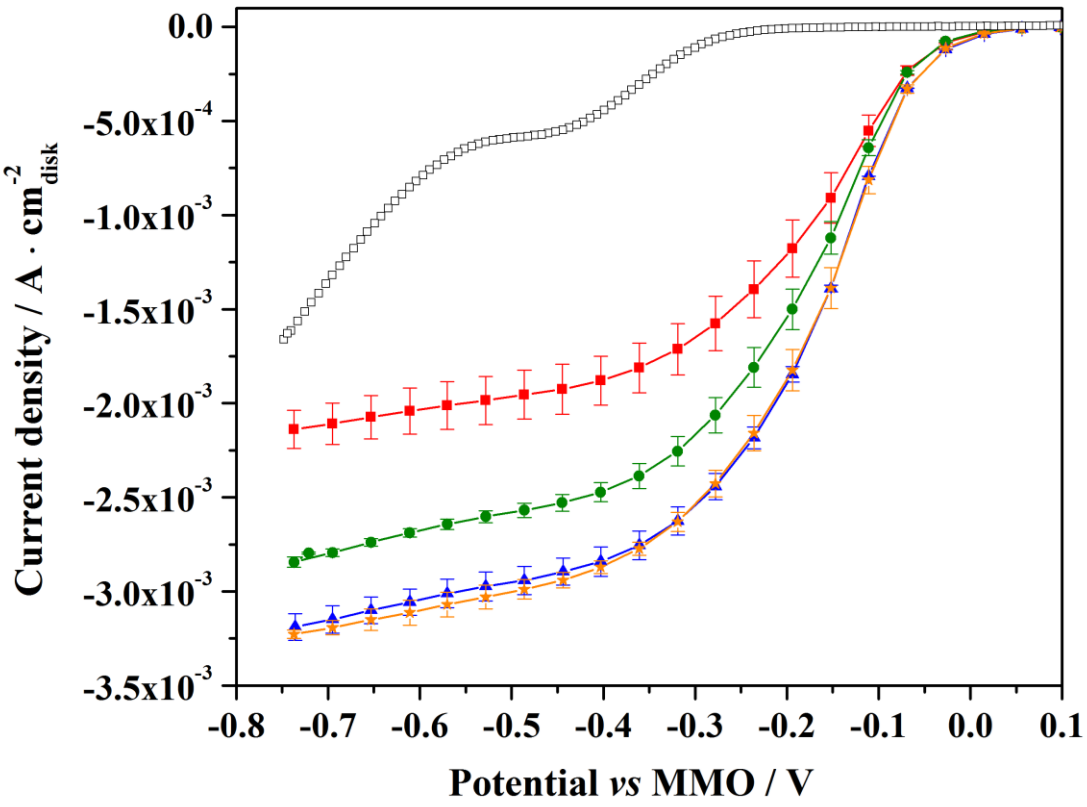

Figure 3.4 Polarization curves for negative going ORR in O_2-saturated 0.1 M KOH on GC (empty square) and on Pt/C coated with 5 µm (square), 2 µm (circle), 1 µm (triangle) and 0.5 µm (star) ionomer film thicknesses; scan rate: 10 mV· s^{-1}; rotation rate: 1600 rpm; temperature: 22 °C. The error bar represents the deviation from three different experiments.

3.2.2 Liquid side film-electrolyte interface concentration

Schematic representation of concentration profile near electrode surface for a rotating electrode coated with ionomer film is shown in Figure 3.5 for two cases, when the current is zero and when the current is diffusion limited. The rotation of electrode in RDE creates a diffusion layer in the liquid side with a thickness, $\delta = 1.61D^{1/3}\upsilon^{1/6}\omega^{-1/2}$, as previously shown in Equation (1.12). Due to rotation of the electrode, convection brings O_2 outside this layer where the concentration of O_2 is essentially equal to bulk concentration, C_B. In this case the current is measured at steady state conditions and the

diffusion length is fixed and is independent of time. It is equal to combined thickness of film and δ. At liquid-film interphase the concentration of O_2 partitions based on Henry's constant, *H*.

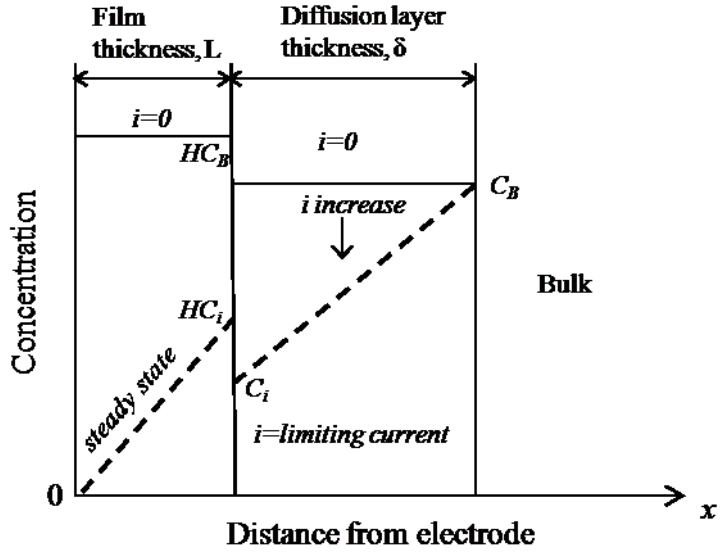

Figure 3.5 Schematic representation of concentration profile near electrode surface for a rotating electrode, i = 0 (solid line); i = limiting current (dashed line).

At steady state, the O_2 flux through film and diffusion layer must be identical and the respective diffusion limited current at high over potential, can be given as,

$$i_L = (nFA(HC_i - 0)D_f L^{-1}) = (nFA(C_B - C_i)D\delta^{-1}) \quad (3.12)$$

Where D_f is the diffusion coefficient of O_2 in ionomer film, *L* is the film thickness, *D* is the diffusion coefficient of O_2 in solution and C_i is the concentration of reactant at the liquid side of the film-electrolyte interface and can be rewritten as,

$$C_i = C_B - \frac{i\delta}{nFAD} \quad (3.13)$$

In Equation (3.13) *i, F, A* are known and $\delta = 1.61D^{1/3}\upsilon^{1/6}\omega^{-1/2}$, C_i and HD_f can be calculated for each rotation speed once *n* is known.

3.2.3 Number of electrons

The purpose of calculating n is to substitute these values in Equation (3.12) and Equation (3.13), so that C_i and HD_f can be determined. However, due to significant electrochemical activity of GC (see Figure 3.4) at high overpotentials, the total limiting

current is a result of the activity from Pt and GC. The number of electrons involved in ORR in alkaline media on Pt and GC/carbon are 4 [84] [55] and 2 [85] [86] [87] respectively. The ORR on GC shows two limiting current regions due to two kinds of active sites [88]. Here first limiting current region can be seen in the given scanned potential range and the other limiting current is expected to reach at more negative potential values. Both limiting regions correspond to 2 electron reaction which was confirmed by detecting H_2O_2 in RRDE experiment [89]. Due to these complications, it is difficult to find the value of n which needs to be substituted in Equation (3.12) and Equation (3.13). Therefore an effective n value is determined from Koutecky-Levich plots.

At any fixed potential in the limiting current region, the current at disk for film coated catalyst layer is described by the modified Koutecky-Levich Equation (1.14) [13],

$$\frac{1}{i} = \frac{1}{i_k} + \frac{1}{i_f} + \frac{1}{i_L} \tag{3.14}$$

where i_f is the film thickness dependent current and can be expressed as $nFAHC_B D_f L^{-1}$. As previously mentioned in section 1.3.1, it should be noted that i_k, i_f and $i_L$in Equation (3.14) is only the conceptual descriptor and does not correspond to current encountered in any real situation. Defining the measured current i by Equation (3.14) offers a convenient way to understand how measured current changes at all operating conditions when either of these currents are rate controlling in different regions of polarization curve.

Equation (3.14) can be rewritten as,

$$\frac{1}{i} = \frac{1}{i_k} + \frac{1}{i_f} + \frac{1}{0.62nFAD_O^{2/3}\omega^{1/2}\nu^{-1/6}C_B} \tag{3.15}$$

According to this, plot of $1/i$ *vs* $\omega^{-1/2}$ (Koutecky-Levich plot) should be straight line with slope equal to $0.62nFAD^{2/3}\nu^{-1/6}C_B$ and intercept as $(1/i_k + 1/i_f)$. To generate Koutecky-Levich plots, ORR voltammograms for all the film thicknesses at various rotation rates are needed. Figure 3.6 shows sample ORR voltammograms measured at 60 °C at various rotation rates for electrode coated with 3 µm film. The current in the limiting region increases as the rotation rate increases. Considering any current value in the diffusion limited region, for example at - 0.4 V, Koutecky-Levich plot can be generated. Figure 3.7 shows the Koutecky-Levich plots for various film thicknesses at - 0.4 V. As

expected the value of n is lower than 4 for all experiments suggesting electrochemical activity from carbon. The number of electrons calculated from Koutecky-Levich plot also accounts for changes in effective diffusion area such that,

$$n = n' \cdot \frac{A'}{A} \tag{3.16}$$

where n' is the number of electrons obtained when effective diffusion area is equal to geometric area A and A' is the effective diffusion area. Therefore n is expected to vary for each experiment as the effective diffusion area depends on catalyst distribution which differs with every coating even for the same catalyst loading. As it will be discussed later in Section 4.1.1, the effective diffusion area is equal to geometric area only when inter-particle distance of catalyst and roughness of CL is much smaller than diffusion layer thickness, δ.

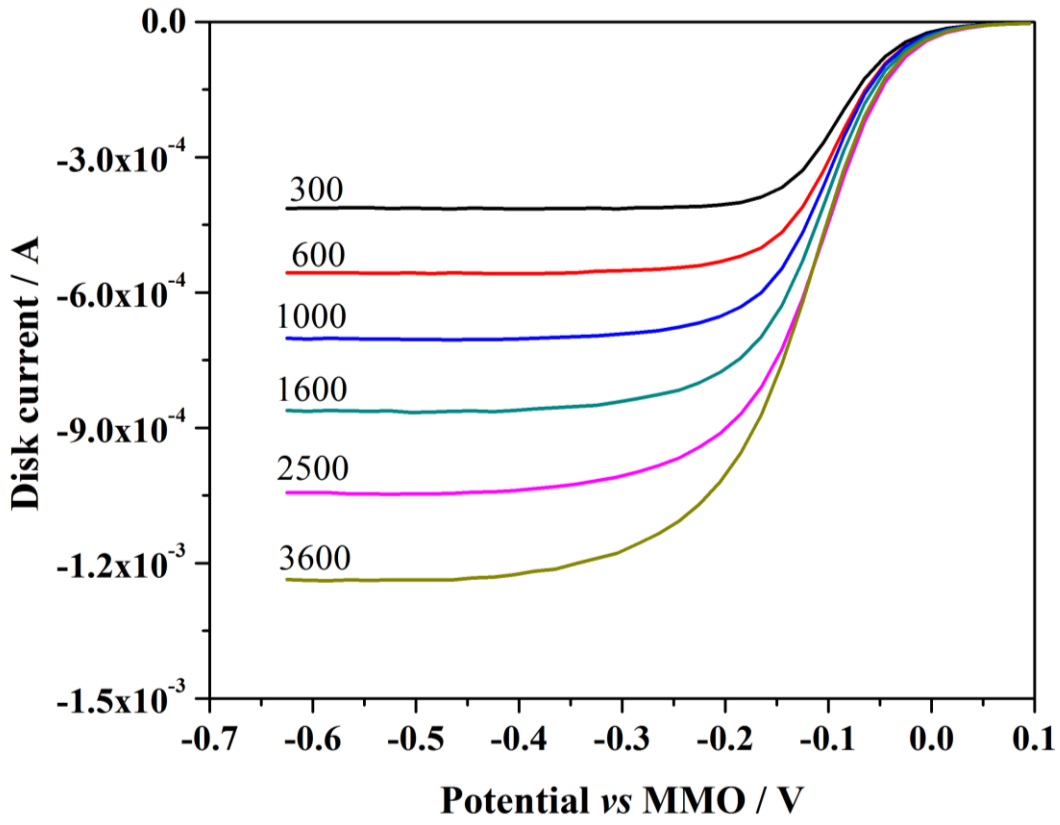

Figure 3.6 ORR voltammogramms for GC coated with 20 $\mu g_{Pt} \cdot cm^{-2}$ at 60 °C with 3 µm ionomer film thickness in O_2-saturated 0.1 M KOH at a scan rate of 10 $mV \cdot s^{-1}$ at various rotation rates in rpm.

Once the values of n is known then the value of HD_f can be calculated from Equation (3.12) at each rotation rate to see the influence of liquid side interface concentration on HD_f. Figure 3.8 shows the variation of HD_f values with respect to C_i values at various rotation rates at 22 °C and 60 °C respectively.

It can be seen that C_i values increase with increase in rpm as expected and the corresponding D_f (since H is expected to be constant) values are nearly constant for all rpms for respective temperature. This shows that the diffusion process in Tokuyama AS-4 ionomer follows Fick's law of diffusion *i.e.* the diffusion coefficient is independent of concentration.

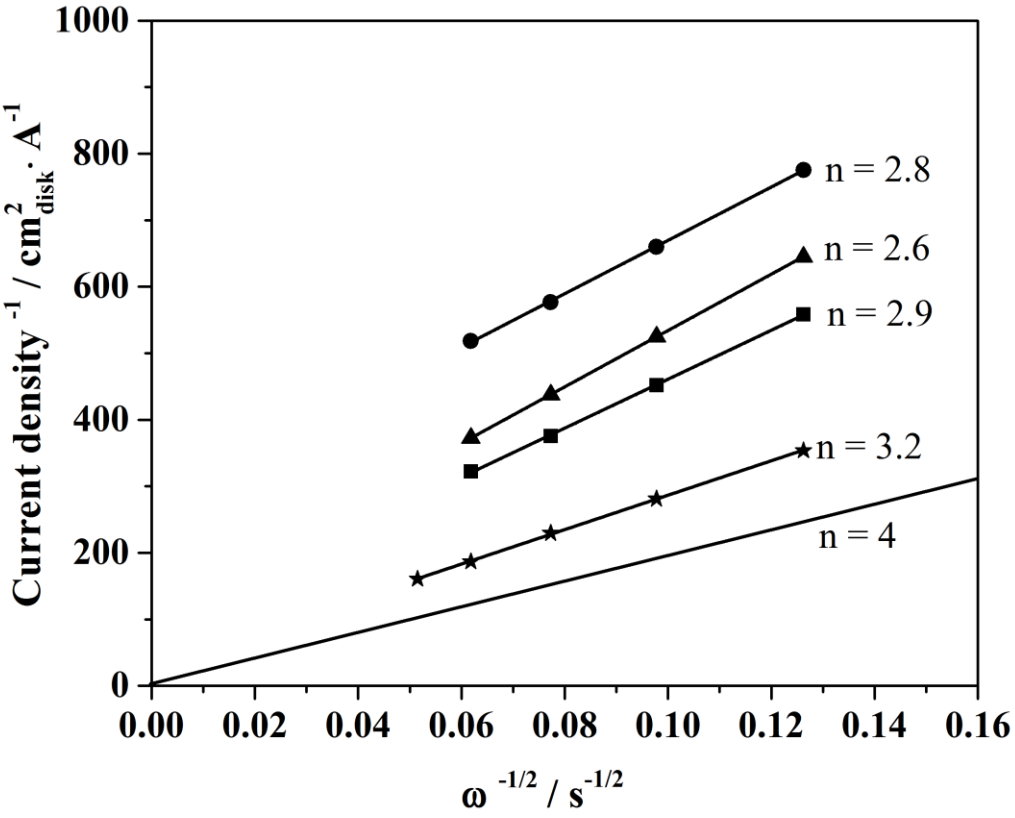

Figure 3.7 Koutecky-Levich plots for ORR at - 0.4 V *vs* MMO in 0.1 M KOH on Pt/C with ionomer film thickness of 5 µm (circle), 2 µm (triangle), 1 µm (square) at 22 °C and 3 µm at 60 °C; theoretical curve for n = 4 (solid line).

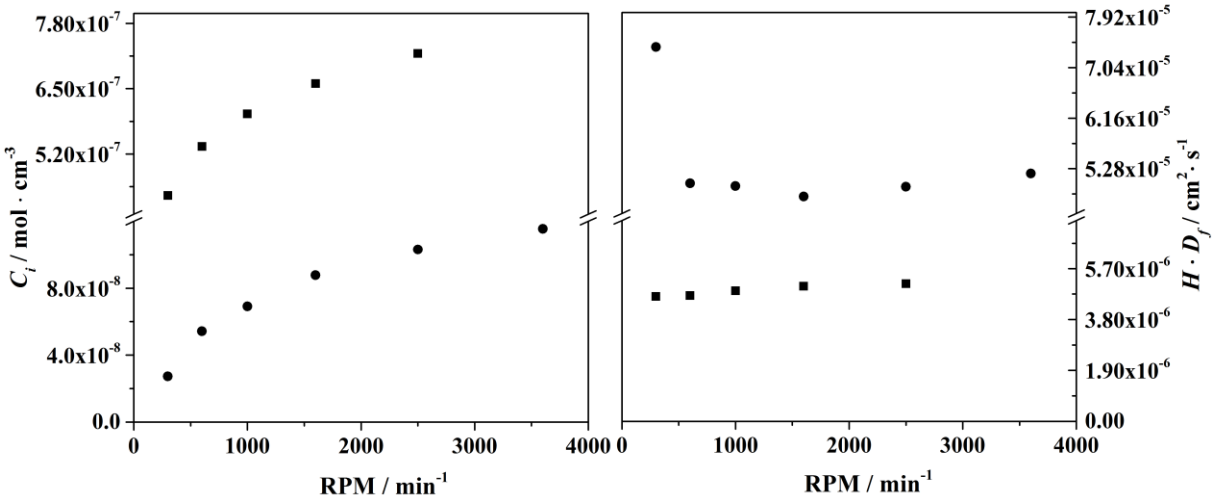

Figure 3.8 Concentrations at film-electrolyte interface in 0.1M KOH with 3 µm film at 60 °C (circle) and 5 µm film at 22 °C (square) and corresponding diffusion coefficients *vs* rpm.

3.2.4 Henry's constant and diffusion coefficient of O_2 in Film

To finally determine the diffusion co-efficient and Henry's constant of O_2 in ionomer film, a chronoamperometric curve is recorded. For chronoamperometry studies the potential is changed stepwise from a point where no O_2 reduction is happening (+ 0.2 V) to a potential where O_2 reduction is diffusion controlled (- 0.5 V). The concentration profile near the electrode coated with ionomer film is schematically shown in Figure 3.9, where solid line represents initial concentration at time $t = 0$ and the dashed line represents concentration profile at any time t after the step potential is imposed. Before the step potential is imposed on the cell, the O_2 concentration is HC_B at the surface of the catalyst. As soon as the potential is imposed on the cell, the current peaks and then reduces rapidly as shown in Figure 3.10.

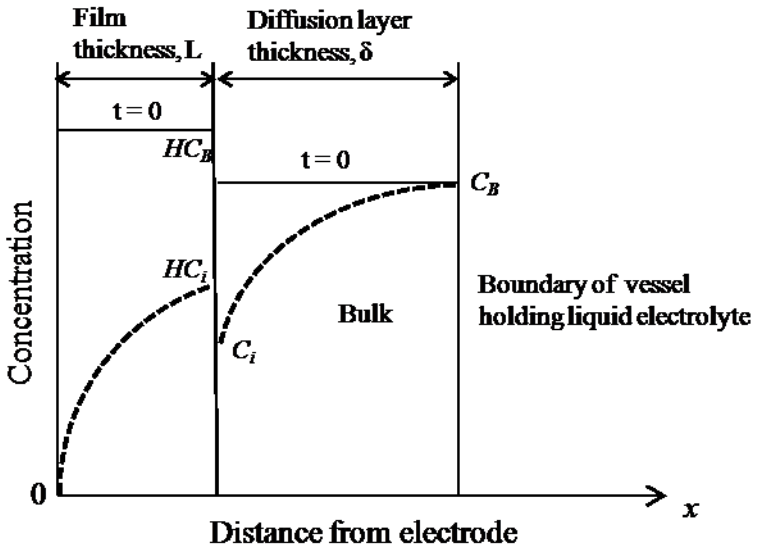

Figure 3.9 Schematic representation of concentration profile near electrode surface for a non-rotating electrode, $t = 0$ (solid line); i = limiting current (dashed line).

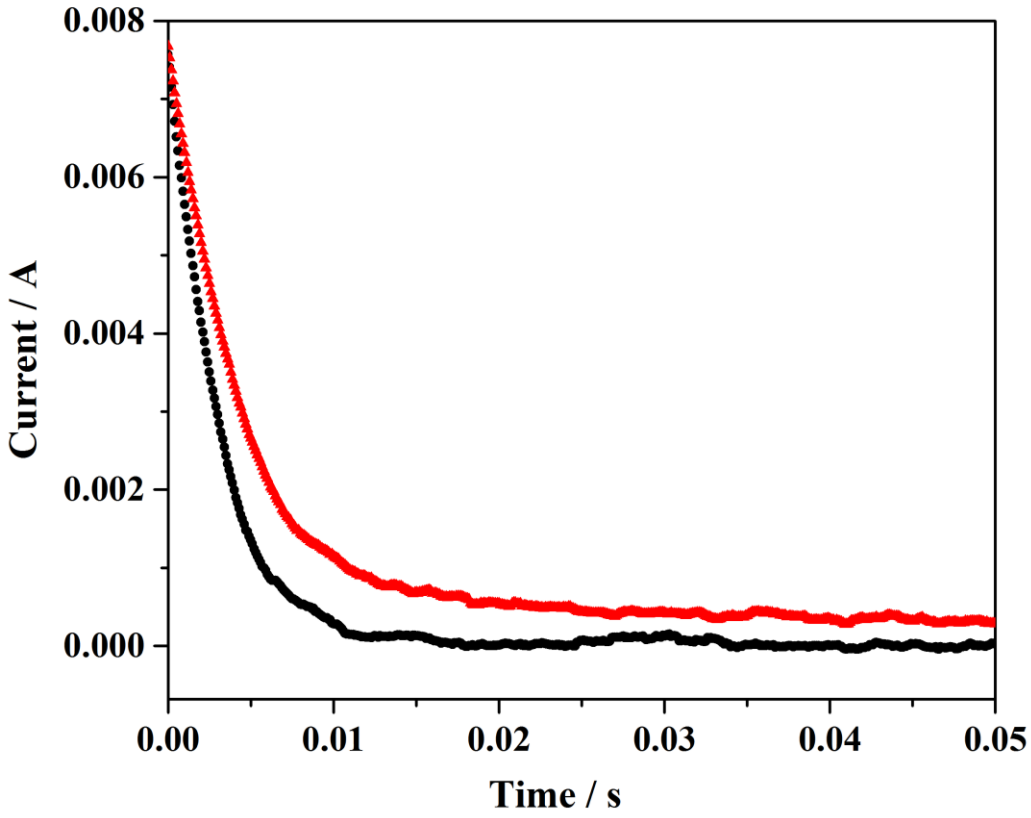

Figure 3.10 Chronoamperometric curve of electrode coated with 3 µm film for O_2 (triangle) and N_2 (circle) saturated electrolyte at zero rpm in 0.1 M KOH at 60 °C.

3.2 Oxygen transport at Pt/C-anion exchange ionomer interface at RDE

The current response for electrode without any film at zero rpm in liquid electrolyte is given by Cottrell equation (Equation (2.19)). For a case where electrode is covered with membrane (> 50 μm) on a microelectrode, a modified Cottrell equation is often used [90] [77] [80].

$$i = \frac{nFAD_f^{1/2}C_f}{\pi^{1/2}t^{1/2}} + \frac{nFAD_fC_f}{r_0} \tag{3.17}$$

where, r_0 is the radius of electrode. The slope of $i(t)$ *vs* $t^{-1/2}$ gives the value of $D_f^{1/2}C_f$ and intercept gives D_fC_f. Since this equation does not consider Henry's constant, its applicability is limited to thicker films. The current can be considered as purely faradaic current only after the time for charging the double layer has been passed. With thicker films the current shows Cottrell behavior for long time and hence Equation (3.17) can be used reasonably well. However, this equation cannot be used for electrodes covered with thin films < 10 μm, as the Cottrell behavior is lost within the time of double layer charging. For thin films, Pamela *et al.* [91] derived the equation by considering following relations,

$$\frac{\partial c_f(x,t)}{\partial t} = D_f \frac{\partial^2 c_f}{\partial x^2} (ionomer\ film) \tag{3.18}$$

$$\frac{\partial c_s(x,t)}{\partial t} = D_s \frac{\partial^2 c_s(x,t)}{\partial x^2} (solution) \tag{3.19}$$

and boundary conditions,

$$c_s(x,0) = C_B \qquad x > L, t = 0 \tag{3.20}$$

$$c_f(x,0) = HC_B \qquad 0 < x < L, t = 0 \tag{3.21}$$

$$\lim_{x\to\infty} c_s(x,t) = C_B \tag{3.22}$$

$$D_f \left(\frac{\partial c_f(x,t)}{\partial x}\right)_{x=L} = D \left(\frac{\partial c_s(x,t)}{\partial x}\right)_{x=L} \tag{3.23}$$

Where x is the distance from electrode and c_f and c_s are the concentration of O_2 in the film and in the solution respectively at any time t. Analytical solution of the differential equation yields,

$$\frac{i(t)}{i_L(t)} = a\left[1 + 2\sum_{j=1}^{\infty}\left(\frac{1-a}{1+a}\right)^{j} e^{(-j^2\delta^2/D_f t)}\right] \tag{3.24}$$

Where $a = \frac{H}{(D/D_f)^{1/2}}$. Figure 3.11 shows the experimentally obtained $i(t)/i_L(t)$ *vs* t curves for electrodes covered with 5 μm at 22 °C and 3 μm film at 60 °C. The value of $i(t)$ is obtained from chronoamperometric curve represented in Figure 3.10. The Cottrell current $i_L(t)$ is calculated from Equation (2.19) by assuming values of C_B and D from Table 3.2.

.

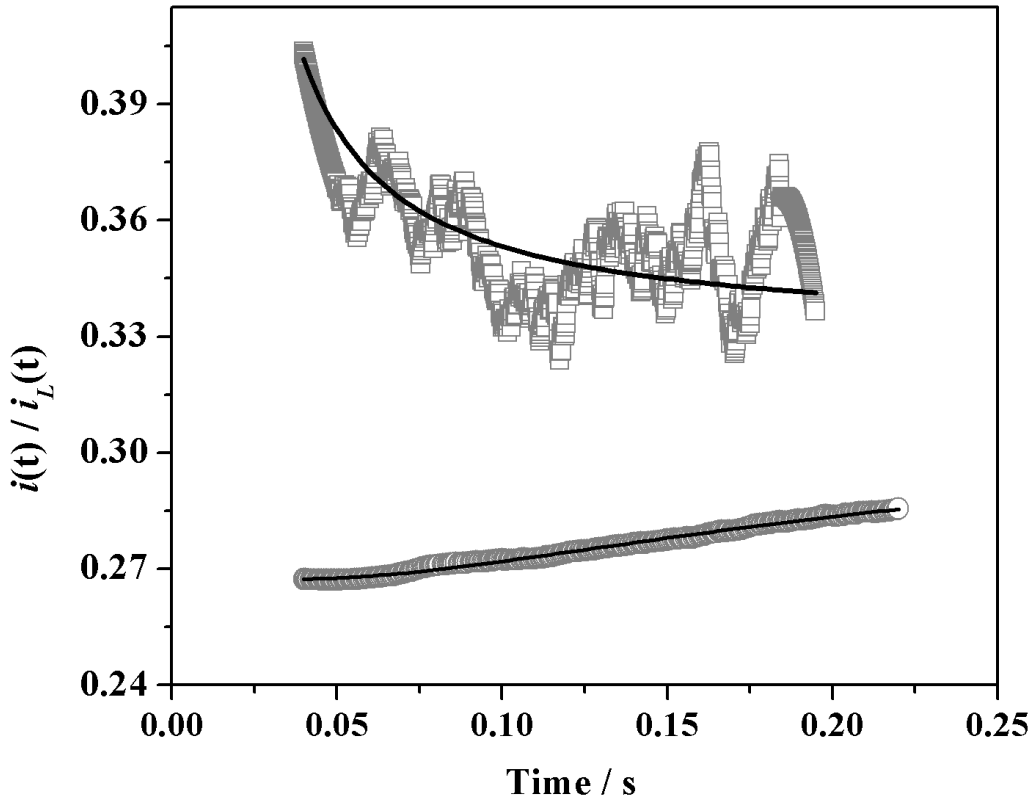

Figure 3.11 $i(t)/i_L(t)$ *vs* t curves for electrodes coated with 5 μm film (circle) at 22 °C and 3 μm film (square) at 60 °C. The solid lines represent the best fit curves according to Equation (3.25).

The time window is chosen based on time required to charge the double layer as lower bound and considering the validity of Equation (3.24) for finite j values. An

approximate value of charge double layer is obtained by conducting CV on these electrodes in a de-aerated solution. The value of C_d is equal to 300 µF at 60 °C for electrode coated with 3 µm film and is equal to 200 µF at 22 °C for electrode coated with 5 µm film. Time taken to charge 99 % of the double layer can be given by $5 \cdot R_u C_d$. This is equal to time < 0.04 s for both the electrodes. The value of $\left(\frac{1-a}{1+a}\right)^j$ lies between - 1.0 to 1.0 for all values of a and the value of $2\sum_{j=1}^{\infty}\left(\frac{1-a}{1+a}\right)^j e^{(-j^2\delta^2/D_f t)}$ can be assumed negligible for j > 40 and t < 0.2 s, assuming $D_f < 2 \cdot 10^{-4}$ cm$^2 \cdot$ s^{-1} at both 22 °C and 60 °C. Using these constraints the chosen time window is between 0.04 to 0.2 s. The experimental curves are fitted using Equation (3.24). The curve fits reasonably well after introducing a correction factor Y, for the values of H and D_f such that HD_f is close to the value obtained with steady state. Equation (3.24) with correction factor becomes,

$$\frac{i(t)}{i_L(t)} = Y.a\left[1 + 2\sum_{j=1}^{\infty}\left(\frac{1-a}{1+a}\right)^j e^{(-j^2\delta^2/D_f t)}\right] \tag{3.25}$$

The value of Y for 3 µm and 5 µm film is 0.33 and 0.303 respectively. This can be justified by variation in calculating Cottrell current $i_L(t)$, which can occur by small variation in the assumed values of either D and or C_B values. The curve fitting is sensitive to H and D_f values for both experiments, showing good fits only for short range of H and D_f values as shown in Figure 3.11. Table 3.1 shows values of $H$and D_f obtained from fitting and HD_f obtained from linear sweep voltammetric measurements at rotating electrode.

Table 3.1 Diffusion parameters determined from linear sweep voltammetry at rotating disk electrode and chronoamperometry at stationary disk electrode in an unstirred solution.

Electrode	Area (cm^2)	Temp (°C)	Loading (µg$_{Pt} \cdot$ cm^{-2})	HD_f (cm$^2 \cdot$ s^{-1})	H	D_f (cm$^2 \cdot$ s^{-1})
				Linear sweep voltammetry	Chronoamperometry	
Pt/C + 5 µm film	0.247	22	8	$5 \cdot 10^{-6}$	2.85 ± 0.05	(1.75 ± 0.31) · 10^{-6}
Pt/C + 3 µm film	0.196	60	20	$50 \cdot 10^{-6}$	6.5 ± 0.5	(7.73 ± 0.6) · 10^{-6}

D_f and C_f values from literature for polymer/liquid and polymer/gas interface are tabulated in Table 3.2 together with values obtained in this work. The polymer material is either ionomer or membrane. The D_f values for Nafion polymer falls in same order whereas the C_f data are slightly scattered. C_f is the representative concentration in the polymer and at the electrode surface when current is zero (see Figure 3.5). It is equal to HC_B and hence depends on the concentration at the polymer/liquid or polymer/gas interface. Since O_2 solubility varies by one order in liquid phase and gas phase, C_f can vary by one order and, hence explains the wide variation of C_f values given in Table 3.2. Therefore, for comparative purpose, Henry's constant at given temperature is a better representation of O_2 transport kinetics rather than C_f. Similarly HD_f is a better representation of rate of O_2 transport rather than permeability, given by $C_f D_f$. The higher the value of HD_f the higher is the O_2 transport rate. H and HD_f values are calculated and tabulated for literature values by assuming C_B values from second part of Table 3.2, where solubility data for O_2 in liquid electrolyte is presented. For oxygen solubility in gas phase, C_B is equal to $3.4 \cdot 10^{-5}$ mol $\cdot$ cm^{-3} at 25 °C and $3 \cdot 10^{-5}$ mol $\cdot$ cm^{-3} at 50 °C when RH is 100 %.

It can be seen that the higher values of H are for polymer/liquid interface where water uptake of polymer is expected to be even more than polymer equilibrated with gas humidified to 100 % RH. This suggests that higher water content of polymer increases O_2 solubility in polymer and hence increases the rate of O_2 transport. This trend is similar to what has been previously observed by [80] [81] where they show increase in O_2 permeability with increase in water content of polymer. The value of HD_f are only 1 - 3 times higher for Nafion ionomer/membrane compared to alkaline membrane/ionomer for experiments with liquid electrolyte as well as without liquid electrolyte. Therefore it can be concluded that O_2 transport at the Pt/anion exchange ionomer interface is not expected to limit alkaline membrane fuel-cell cathode performance. On similar grounds, H_2 transport at the Pt/anion exchange ionomer interface is not expected to limit alkaline membrane fuel-cell anode performance, since D_{H_2} is generally larger than D_{O_2} [79] [92].

3.2 Oxygen transport at Pt/C-anion exchange ionomer interface at RDE

Table 3.2 Mass transport parameters of O_2 in various electrode interfaces

Medium	D_f [a] · 10^5 ($cm^2 \cdot s^{-1}$)	C_f [b] · 10^6 ($mol \cdot cm^{-3}$)	H	HD_f · 10^{-5} ($cm^2 \cdot s^{-1}$)	Temp. (°C)	Ref.
AS-4 ionomer film in 0.1 M KOH	0.175	3.42	2.85	0.5	22±1	This work
AS-ionomer film in 0.1 M KOH	0.77	4.22	6.5	5	60	This work
A201 anion exchange membrane	0.429	0.93	0.027	0.01	25	[83]
Neosepta anion exchange membrane in 0.5 M K_2SO_4	0.024	0.77	-	-	25	[79]
Nafion membrane in 0.5 M K_2SO_4	0.024	7.2	-	-	20	[79]
Nafion membrane in 0.5 M H_2SO_4	0.070	13	11.5	0.8	20	[78]
Nafion membrane 100% RH	0.074	26	0.76	0.056	25	[77]
Nafion membrane in 1 N H_2SO_4	0.062	18.7	16.5	1.02	25	[82]
Nafion membrane in water	0.095	9.34	7.18	0.68	30	[76]
Nafion membrane 100% RH	0.075	10.65	0.31	0.023	30	[80]
Nafion membrane 100% RH	0.217	6.68	0.22	0.047	50	[80]
Nafion membrane in water	0.245	8.56	-	-	50	[75]
Nafion membrane 100% RH	0.6	0.4	0.013	0.008	50	[81]
Nafion ionomer film in 0.7 M H_3PO_4	0.2	3.7	3.39	0.68	-	[74]

[a] Diffusion coefficient of O_2 in ionomer film/membrane, [b] solubility of O_2 in ionomer film/membrane

Medium	$D^{c} \cdot 10^{5}$ ($cm^2 \cdot s^{-1}$)	$C^{d} \cdot 10^{6}$ ($mol \cdot cm^{-3}$)	Temperature (°C)	Ref.
0.1 M KOH	1.9	1.2	20	[15]
0.1 M KOH	4.5	0.65	60	[15]
1 M KOH	1.65	1.0	25	[93]
0.7 M H_3PO_4	1.94	1.09	-	[74]
0.5 M H_2SO_4	-	1.13	25	[79]
1 M H_2SO_4	-	0.9	25	[93]
H_2O	2.95	1.3	25	[79]

[c] Diffusion coefficient of O_2 in liquid electrolyte, [d] solubility of O_2 in liquid electrolyte

Chapter 4
Kinetic Losses[4]

In this chapter, the overpotential caused by kinetic losses is evaluated for ORR on Pt/C at RDE, and for HOR and ORR on Pt/C in AMFC. To gain more insight into ORR kinetics, kinetic parameters such as exchange current, i_0 and charge transfer coefficient, α are determined at various concentrations of O_2 in 0.1 M KOH and AMFC at 60 °C. The kinetic parameters for ORR on Pt/C in AMFC and 0.1 M KOH at various O_2 concentrations are rarely reported at 60 °C. In addition a rate expression is provided for ORR in 0.1 M KOH accounting for O_2 concentration and limiting current. The obtained kinetic parameters from these studies are compared with kinetic parameters obtained from AMFC and PEMFC.

4.1 *ORR kinetic loss measured in 0.1 M KOH at RDE*

The Rotating Disk Electrode method in conjunction with linear sweep voltammetry is widely used for evaluation of catalyst for their catalytic activity for application in electrochemical devices such as fuel cells and metal-air batteries. Rotation of disk electrode enables the electrochemical measurements at steady state conditions. Investigation of ORR at RDE with Pt and non-Pt catalyst is one of the most widely studied topics due to its direct application in fuel cells. These studies are often made in the search

[4] Part of the results in this Chapter published in P.S. Khadke, U. Krewer, *Electrochem. Comm*. 51 (**2015**) 117-120.

of electro-catalyst with high activity towards ORR since ORR is found to be limiting reaction in PEMFC when Pt is employed as catalyst. Much research has been done in the past on Pt/C activity towards ORR in both acidic and alkaline media. The reported values of kinetic currents vary by as much as 2 order of magnitude based on measurement procedure [53]. Due to this, in the last decade some research groups [54] [94] have mainly focused on development of RDE method for better evaluation of catalytic activity of Pt towards ORR. One such well-established optimized methodology [54] [52] comprises of coating the Pt/C catalyst on GC with loadings less than 30 $\mu g_{Pt} \cdot cm^{-2}$, coating a thin ionomer film (< 0.5 μm) over catalyst to bind the catalyst to GC, performing cyclic voltammetry at 50 $mV \cdot s^{-1}$ in a de-aerated liquid electrolyte for determining ECSA, performing LSV between 5 - 20 $mV \cdot s^{-1}$ at 1600 rpm in O_2 saturated liquid electrolyte and determining the kinetic current at 0.9 V *vs* RHE for a mass transfer and iR corrected positive going sweep in LSV. Kinetic currents are often reported after normalizing with respect to ECSA or mass of Pt to account for different catalyst loadings used by various groups. In this Thesis, a more or less similar optimized procedure is adapted except that the kinetic parameters were obtained from sampled voltammetry (constant potential for fixed time) rather than LSV.

The measured current from electrode is always under the influence of mass transport loss and ohmic loss. The ohmic loss can be easily corrected once R_u is known. The limiting current i_L is an indicator of how large is the mass transport losses. The measured current after iR correction is nearly equal to kinetic current only when limiting current is large as evident from Equation (2.17). In general for qualitative analysis it can be assumed that $i \sim i_k$ when $i < 0.1\ i_L$. Hence in order to determinei_k, knowledge of i_L is required. For the purpose of qualitative examination, the region of polarization curve where $i < 0.1\ i_L$ is referred as kinetic region in further discussions.

4.1.1 Limiting current at various loadings

The limiting current is directly proportional to effective diffusion area which in turn depends on how diffusion fields are formed. The effective diffusion area depends on relative magnitude of CL roughness and inter-particle catalyst distance to the diffusion layer thickness [41] [95] [96]. Figure 4.1 shows the schematic representation of two scenarios. When the GC is covered by catalyst particles such that inter-particle distance and CL thickness are much lower than diffusion layer thickness, then the effective

diffusion area is the area of whole GC even though some area of GC is not covered by catalyst. When the GC is covered by catalyst particles such that inter-particle distance are much larger than diffusion layer thickness, then the diffusion fields are only locally formed and the effective diffusion area is the geometric area of agglomerate particle locally. The magnitude of the effective diffusion area can be qualitatively assessed by looking at the optical images of GC coated with various loading of catalyst as shown in Figure 4.2. It shows image of GC coated with 1 $\mu g_{Pt} \cdot cm^{-2}$, 5 $\mu g_{Pt} \cdot cm^{-2}$ and 40 $\mu g_{Pt} \cdot cm^{-2}$. The black area is the GC area mostly not covered with catalyst particles and grey area is GC area covered with catalyst particles varying in population and density depending on loading. It can be seen that for GC coated with 40 $\mu g_{Pt} \cdot cm^{-2}$ the GC is completely covered with multiple layers of catalyst particles whereas for GC coated with 1 $\mu g_{Pt} \cdot cm^{-2}$ and 5 $\mu g_{Pt} \cdot cm^{-2}$ the uncovered area is in order of mm. When the GC is rotated at 1600 rpm at 60°C, the diffusion layer thickness calculated from Equation (1.12) is equal to 18.2µm, and as shown previously in section 2.3.3.1 the CL roughness is < 1 µm. Therefore the diffusion field of catalyst particles in black area will be clearly separated from that of diffusion field of grey area. The inter-particle distance with in the grey area depends on the loading and is slightly higher for lower loading than for higher loadings as previously shown in Figure 2.4. For these reasons the diffusion limited current may vary for GC coated with loadings < 10 $\mu g_{Pt} \cdot cm^{-2}$ and since the catalyst distribution changes in each experiment, the diffusion limited current may vary for two experiments even though the loadings are kept identical.

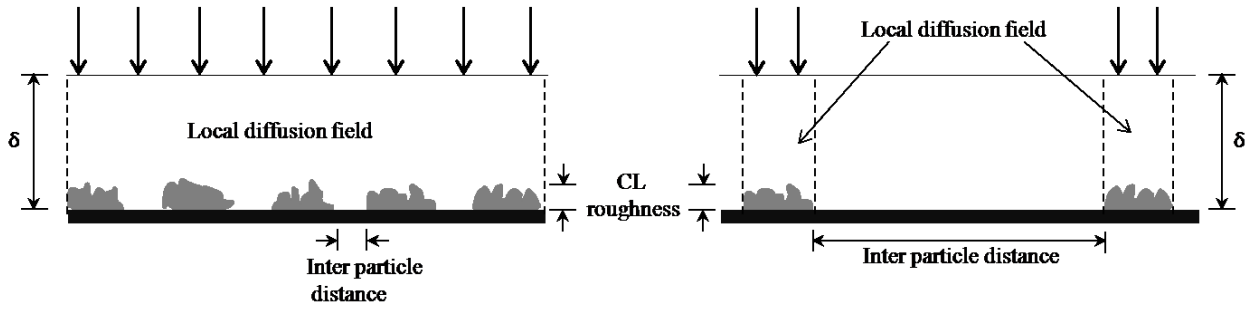

Figure 4.1 Schematic representation of the diffusion filed when interparticle distance is **(left)** less than diffusion layer thickness; **(right)** greater than diffusion layer thickness.

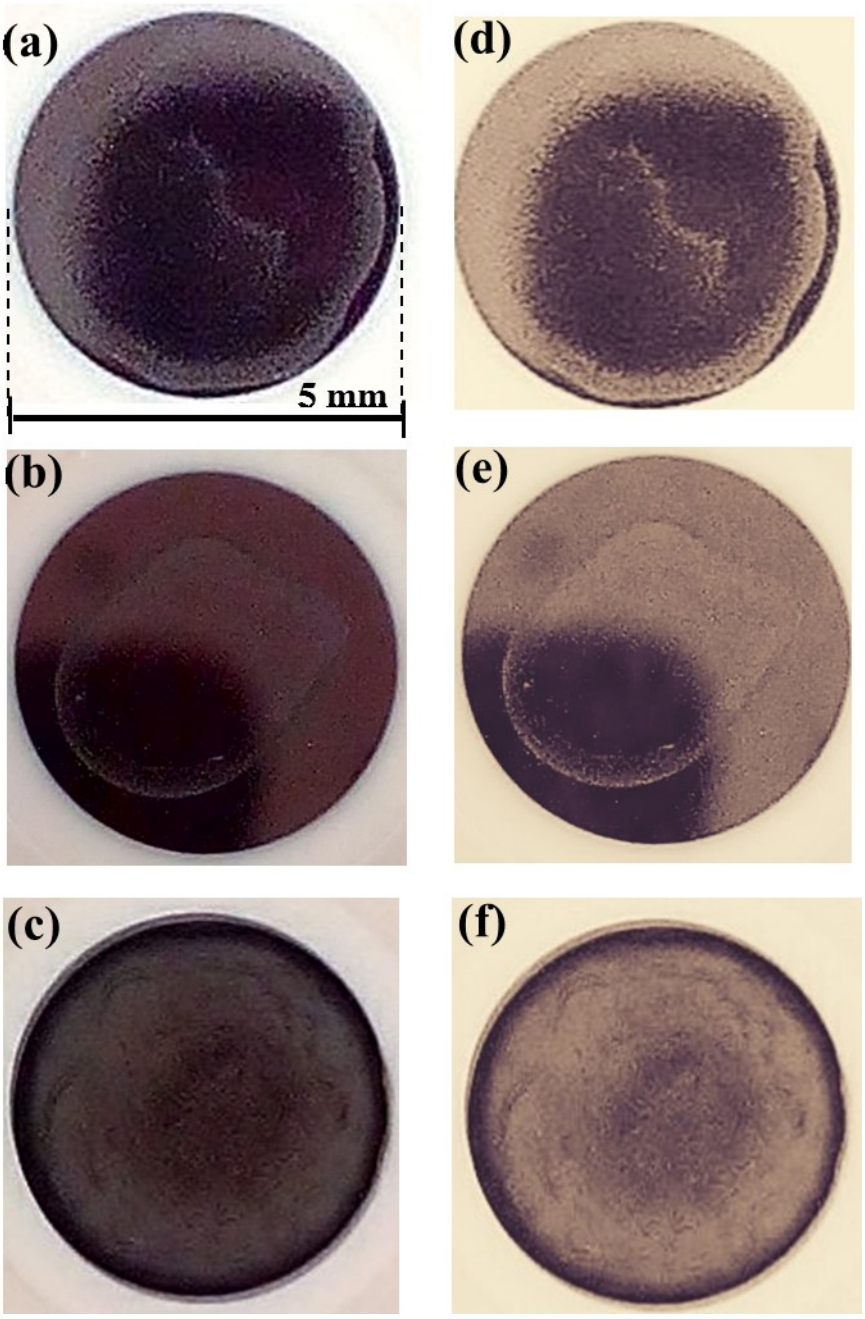

Figure 4.2 Original optical images (left) and processed images (right) of GC coated with 1 $\mu g_{Pt} \cdot cm^{-2}$ **(a, d)**, 5 $\mu g_{Pt} \cdot cm^{-2}$ **(b, e)** and 40 $\mu g_{Pt} \cdot cm^{-2}$ **(c, f)** loadings.

At RDE, diffusion limited current can be obtained for ORR by performing LSV at wide range of scan rate (typically between 5-100 $mV \cdot s^{-1}$). It has been shown in Section 3.2.1 that electrodes with ionomer film < 1 μm are suitable for kinetic analysis, hence all the electrodes used hereafter employed film thickness of 0.5 μm.

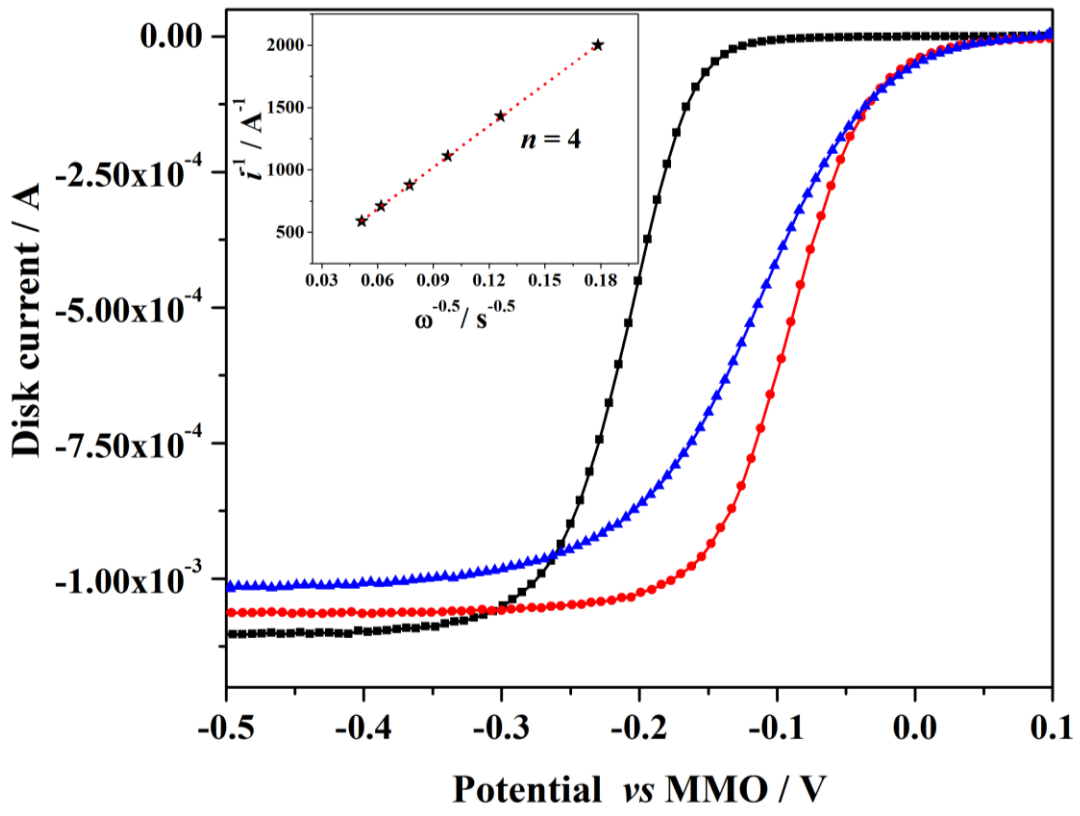

Figure 4.3 Linear sweep voltammograms of ORR at Pt disk (square) and various high Pt loading, 20 $\mu g_{Pt} \cdot cm^{-2}$ (circle), 10 $\mu g_{Pt} \cdot cm^{-2}$ (triangle) with scan rate of 20 mV . s^{-1} at 60 °C, 1600 rpm. Inset: Koutecky-Levich plot for Pt disk.

Figure 4.3 shows LSV of ORR measured for Pt disk and GC coated with 20 $\mu g_{Pt} \cdot cm^{-2}$ and 10 $\mu g_{Pt} \cdot cm^{-2}$, where current values reach diffusion controlled limiting current at higher overpotential (more negative potential) values. The geometric area of GC and Pt disk are 0.196 cm^2. The limiting current for Pt disk electrode is 1.11 mA which is very close to the theoretical i_L calculated from Equation (1.11) at 1600 rpm as 1.15 mA. The theoretical limiting current is calculated after determining number of electrons from slope of Koutecky-Levich plot for Pt disk as described previously in Section 3.2.3. The Koutecky-Levich plot for Pt disk is shown in the inset of Figure 4.3. The assumed values of D, C_B and ν are $4.5 \cdot 10^{-5}$ $cm^2 \cdot s^{-1}$, $6.5 \cdot 10^{-7}$ $mol \cdot cm^{-3}$ and 0.0048 $cm^2 \cdot s^{-1}$ respectively [15]. As frequently reported in the literature [84] [55] , it is found that the number of electrons for ORR on Pt is 4 which in turn suggests (recall Equation (3.17)) that effective diffusion area and geometric area are identical. For GC coated with Pt/C there is more than

one type of catalytically active sites. Apart from Pt, all types of carbon show some activity towards ORR [85] [86] [87]. This means that carbon of Pt/C and underlying GC surface can catalyze ORR. However for GC/carbon to be electrochemically active two criteria must be met a) electrode is polarized to high overpotential b) Pt particles are not in the vicinity of GC/carbon for tens of μm. Due to this the activity of carbon of Pt/C can be neglected in all cases as agglomerate size of Pt/C on GC is < 1 μm. At low loadings however significant amount of GC is exposed and Pt particles are not in the vicinity for tens of μm as shown in Figure 4.2 for GC coated with 1 $\mu g_{Pt} \cdot cm^{-2}$ and 5 $\mu g_{Pt} \cdot cm^{-2}$. In this case the limiting current at high overpotential will be significantly influenced by electrochemical activity of uncovered GC area. Although not very prominent, this effect can be seen for GC coated with 10 $\mu g_{Pt} \cdot cm^{-2}$ and 20 $\mu g_{Pt} \cdot cm^{-2}$ where limiting current reduces slightly as the loading is reduced from 20 $\mu g_{Pt} \cdot cm^{-2}$ to 10 $\mu g_{Pt} \cdot cm^{-2}$.

The interference from GC activity can be clearly seen by comparing ORR voltammograms of bare GC with GC coated with 1 and 5 $\mu g_{Pt} \cdot cm^{-2}$ (Figure 4.4). The disk current seems to reach a limiting current at - 0.2 V before the current is again increased due to GC activity. Here the geometric area of Pt, is low compared to earlier experiments and geometric area of uncovered GC is significantly high. Separating the influence of GC/carbon in the limiting current region is essential when the kinetic parameters for ORR with respect to Pt is desired. Although the voltammograms for GC coated with 1 $\mu g_{Pt} \cdot cm^{-2}$ and 5 $\mu g_{Pt} \cdot cm^{-2}$ have non-zero slope implying surface concentration C_O to be non-zero, it can be still assumed that in absence of GC activity, the limiting current due to geometric area of Pt would have been reached near to -0.2V. This assumption is reasonable considering the way diffusion field is formed for GC coated with low loading of Pt, concentration field is formed near isolated active sites [96] and insignificant GC activity at - 0.2 V.

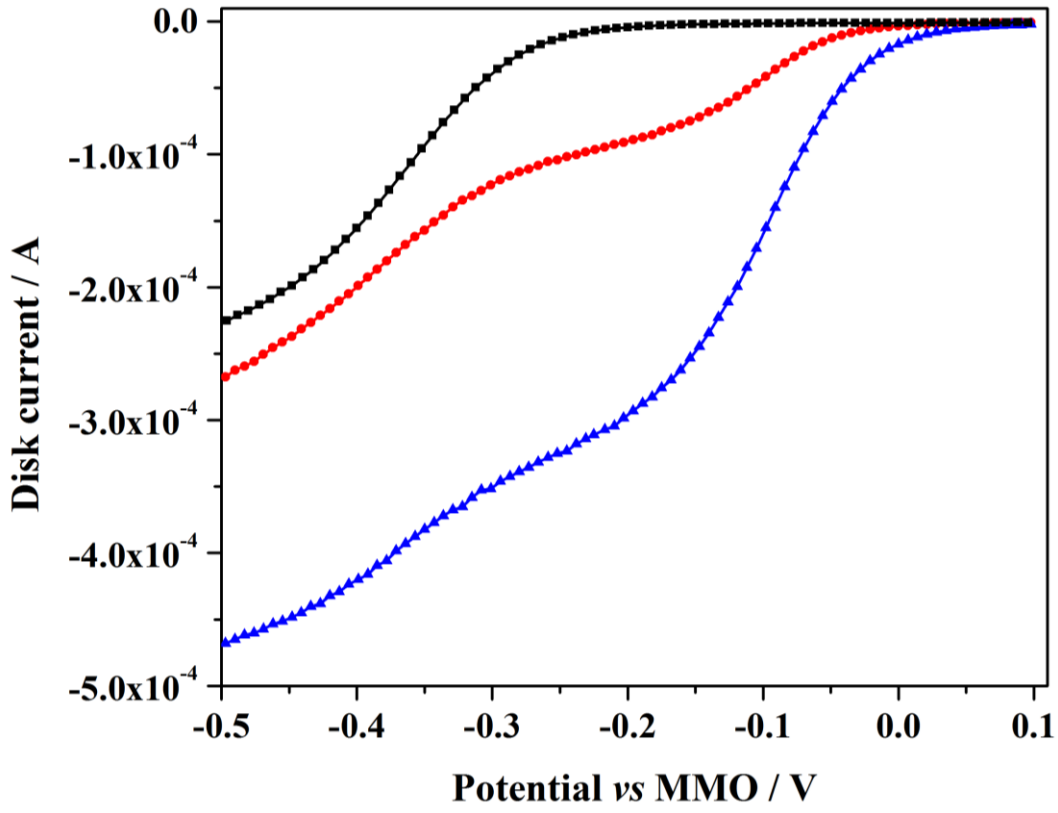

Figure 4.4 Linear sweep voltammograms of ORR at bare GC disk (square) and GC coated with various low Pt loadings, 1 $\mu g_{Pt} \cdot cm^{-2}$ (circle), 5 $\mu g_{Pt} \cdot cm^{-2}$ (triangle) with scan rate of 20 mV . s^{-1} at 60 °C, 1600 rpm.

4.1.2 Catalyst utilization

The limiting current depends only on the geometric area of the electrode whereas kinetic current depends largely on the microscopic area of the catalyst which can be several orders higher in magnitude than the geometric area. It should be noted that when the current is diffusion limited, the magnitude of the current for a given effective diffusion area remains identical independent of whether the CL is thinner or thicker. As long as the CL roughness remains much lower than diffusion layer thickness, the limiting current is not affected by multiple layers of catalyst particles. However, when the current is not diffusion limited, for instance in kinetic region, O_2 may diffuse deep into the CL and react. Hence due to the high number of active sites in Pt/C electrode than Pt disk, the current in kinetic region for Pt/C electrode are much higher than Pt disk as can be seen in Figure 4.3. Yet, current in the kinetic region for GC coated with 10 $\mu g_{Pt} \cdot cm^{-2}$ and 20 $\mu g_{Pt} \cdot cm^{-2}$ are similar. This is counter intuitive as kinetic current is supposed to double when the catalyst loading

doubles. This suggests that only some of the catalyst particles are participating in the reaction and there are some buried catalysts particles which do not have access to O_2. The kinetic parameters obtained from electrode with such loadings certainly lead to large error. Higher loadings may identify limiting current precisely, they nonetheless lead to low catalyst utilization. Whereas in Figure 4.4, the current in kinetic region for GC coated with 1 $\mu g_{Pt} \cdot cm^{-2}$ is about 4 - 5 times lower than GC coated with 5 $\mu g_{Pt} \cdot cm^{-2}$ suggesting the catalyst utilization is nearly complete. If catalyst utilization is complete, the kinetic current will increase linearly with increase in the loading such that the mass normalized curves will merge with each other. Therefore in the following section the kinetic current is determined for the electrodes after making sure that the loadings are in the range where catalyst utilization is nearly complete.

4.1.3 Steady-state measurements

In Butler-Volmer equation, current in the current-overpotential ($i - \eta$) relation is a steady state current. Hence in this work, the kinetic parameters are obtained from steady state polarization curve analogous to that shown in Figure 4.5. It shows the current behavior for step change in voltage for GC coated with 5 $\mu g_{Pt} \cdot cm^{-2}$. From time 0 to 270 s the overpotential is changed stepwise with step duration of 30 s. Right after every overpotential step, the current peaks to charge the double layer and reaches steady state value after 10 - 15 s.

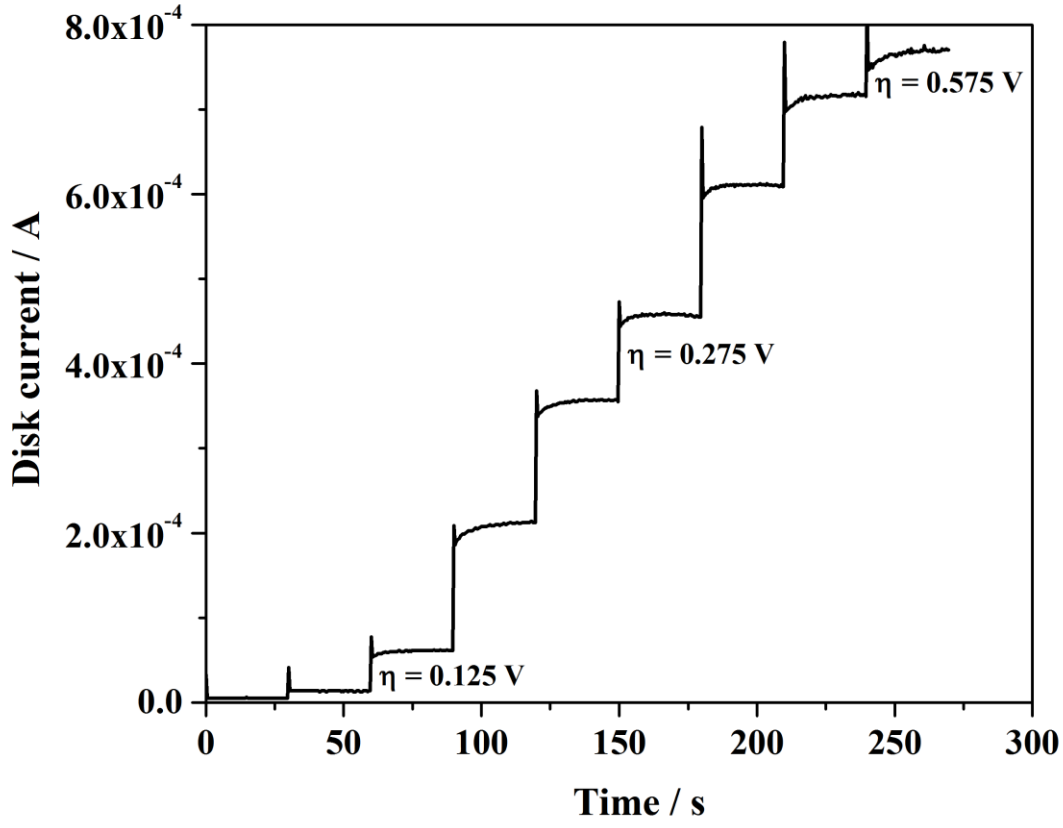

Figure 4.5 ORR current measured for GC coated with 5 $\mu g_{Pt} \cdot cm^{-2}$ with respect to time for varying overpotential at 1600 rpm in 0.1 M KOH at 60 °C.

4.1.3.1 Repeatability and reproducibility

$i - \eta$ curves are generated and plotted in Figure 4.6 by considering the data obtained at 30^{th} s for each overpotential step from Figure 4.5. Excellent repeatability between the consecutive cycles of $i - \eta$ curves have been observed for each overpotential step. This suggests that within the duration of the experiment, catalyst surface has undergone only reversible changes if any changes are to occur due to surface reorientation or adsorption of non-reacting adsorbing species.

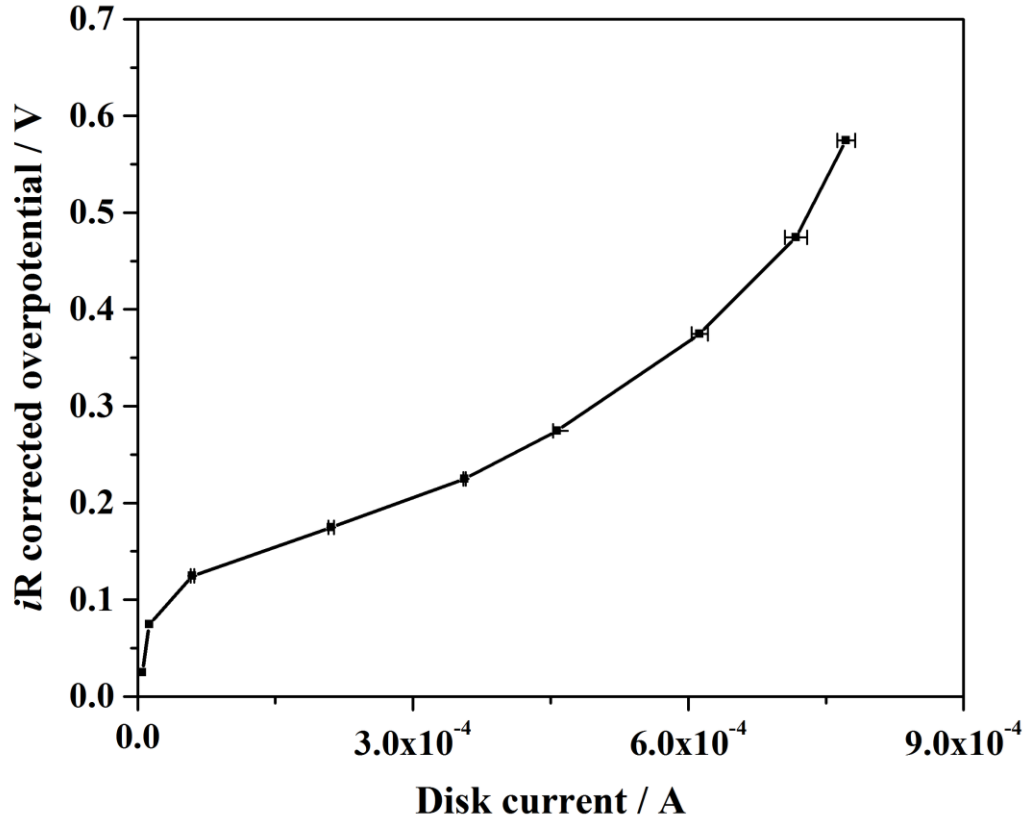

Figure 4.6 Repeatability of $i - \eta$ curve for GC coated with $5\mu g_{Pt} \cdot cm^{-2}$ in 0.1 M KOH at 60 °C. The error bar represents the deviation between the currents obtained from 3 cycles of the same experiment.

Good reproducibility is also obtained between experiments as shown in Figure 4.7. As discussed previously in Section 4.1.1, the limiting current for ORR with respect to Pt reaches at - 0.2 V *vs* MMO, this corresponds to overpotential of 0.275 V. Beyond this overpotential activity of carbon also contributes to the total current. It can be seen that until this overpotential, the reproducibility is excellent after which it starts to deviate. The limiting current at overpotential > 0.275 V depends on uncovered GC area and the catalyst distribution. Therefore, for lower loading the limiting current may vary depending on how catalyst is distributed on GC. Electrode with fine catalyst distribution covering larger GC area can give higher limiting current than electrode with coarse catalyst distribution covering lesser GC area even though the loading of both electrodes are same. Since the electrodes are prepared by dropping catalyst ink on GC according to the procedure described in Section 2.3.1, it is difficult to obtain a consistent distribution in every experiment. This can be supported further by comparing Figure 4.6 and Figure 4.7, where deviation in data in Figure 4.6 is very less until overpotential equal to 0.275 V. It should

be noted that variation in catalyst distribution does not cause inconsistency in kinetic current region and currents are reproducible.

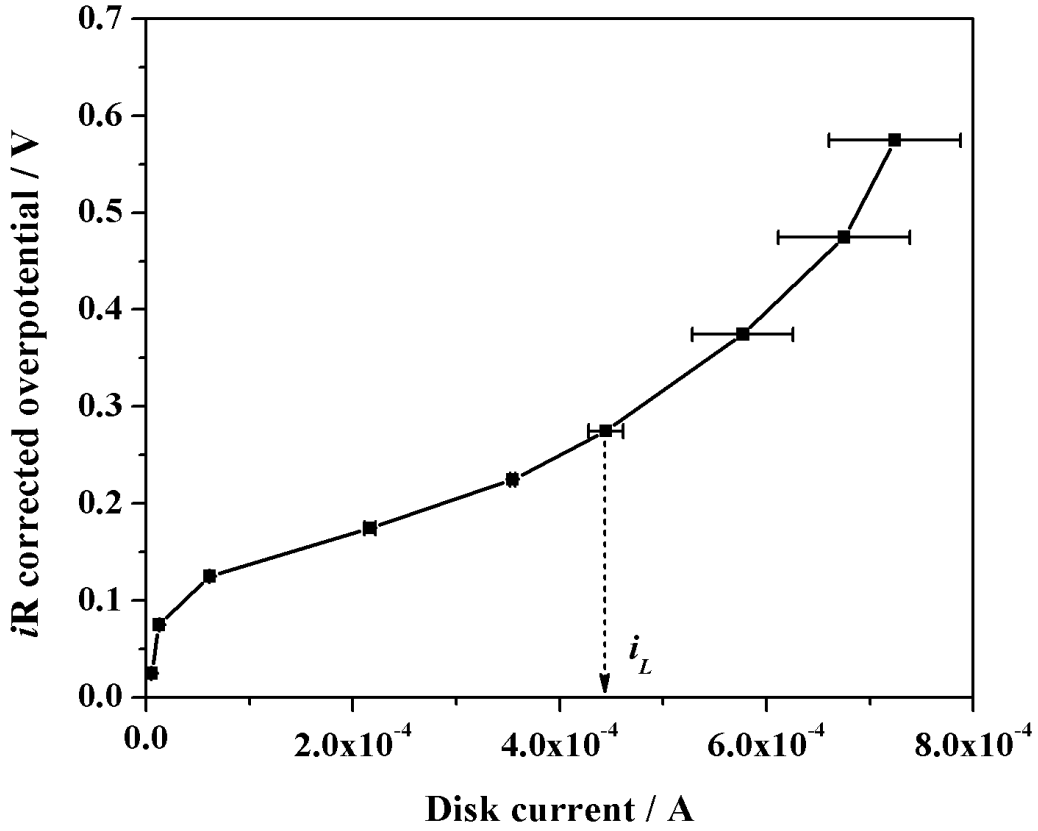

Figure 4.7 Reproducibility of $i - \eta$ curves for GC coated with 5$\mu g_{Pt} \cdot cm^{-2}$ in 0.1 M KOH at 60 °C. Error bar represents deviation of two experiments.

4.1.3.2 Complete catalyst utilization

Previously in Section 4.1.2 the importance of catalyst utilization was discussed. Figure 4.8 shows the mass-normalized $i - \eta$ curves for two different Pt loadings. The curves merge very well and stay within the experimental error until overpotential of 0.275 V, showing near to complete utilization of catalyst for the ORR. It can be concluded from Figure 4.3, Figure 4.4 and Figure 4.8 that complete utilization of catalyst can be obtained for ORR on Pt in alkaline media for loading $\leq$ 10 $\mu g_{Pt} \cdot cm^{-2}$. Therefore the kinetic parameters are determined from electrode with 5 $\mu g_{Pt} \cdot cm^{-2}$ loading.

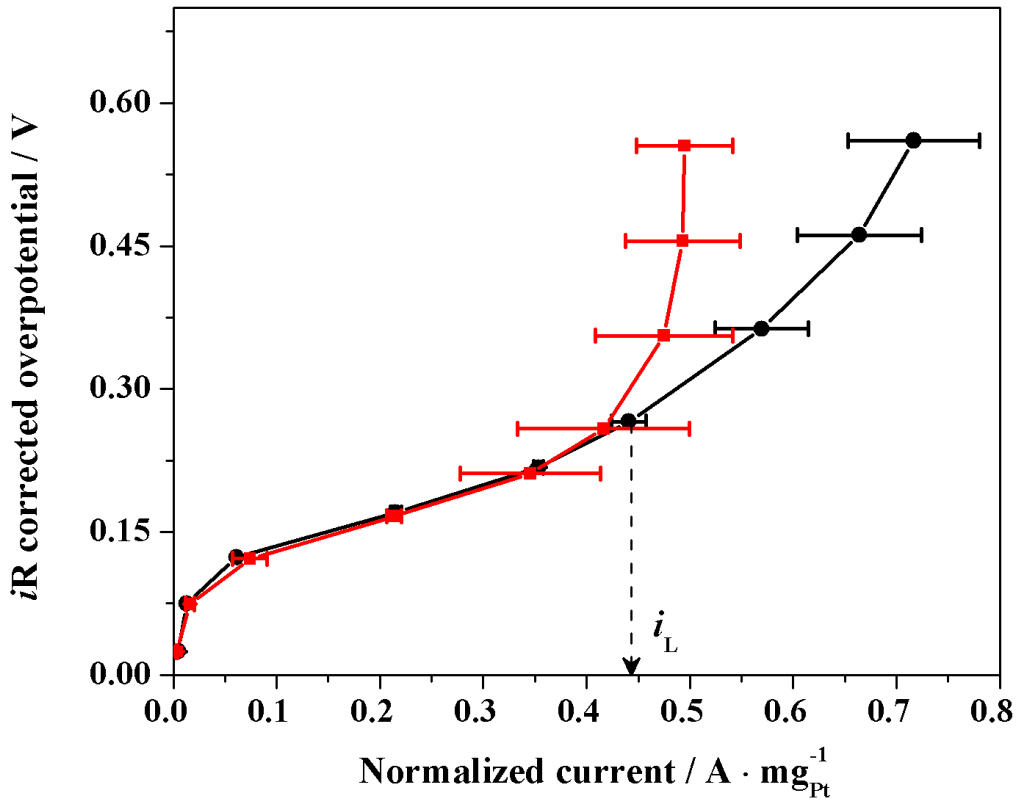

Figure 4.8 $i-\eta$ curves normalized to mass of Pt for GC coated with 5 $\mu g_{Pt} \cdot cm^{-2}$ (circle) and 10 $\mu g_{Pt} \cdot cm^{-2}$ (square) in 0.1 M KOH at 60 °C. The limiting current with respect to Pt is represented by dashed arrow. Error bar represents deviation of two experiments.

In Figure 4.8, $i-\eta$ curves are normalized to mass of Pt. In some literature [53] [97] [98], there is also a practice of normalizing $i-\eta$ curve with respect to ECSA determined by performing CV (see Section 2.2.2) on Pt/C. This has been shown to work especially when comparing activities of Pt/C with different wt. %. [53]. It should be noted that normalization by ECSA is based on the assumption that the entire electrochemical active Pt sites available for hydrogen adsorption/desorption in the absence of O_2, is also available for ORR in the presence of O_2. It assumes that when the ECSA increases, the active sites for ORR also increase to same degree. This assumption is not valid for ORR on polycrystalline Pt in alkaline media as it can be seen from Figure 2.6, where CVs in N_2 saturated electrolyte show decrease in ECSA over period of time even though ORR in O_2 saturated electrolyte increases.

4.1.4 Determination of kinetic parameters

To gain more insight into ORR kinetics, ORR voltammograms are measured at several O_2 concentrations and Tafel plots are obtained at all these concentrations. The concentration of O_2 in liquid electrolyte is varied by bubbling the gas mixture containing varied concentration of O_2 and N_2. Depending on the O_2 concentration in gas, the O_2 concentration in liquid will be set according to the Henry's constant (also called as partition coefficient) at the gas-liquid interphase. Figure 4.9 shows the schematic of concentration profile of O_2 at gas-liquid interphase at equilibrium conditions.

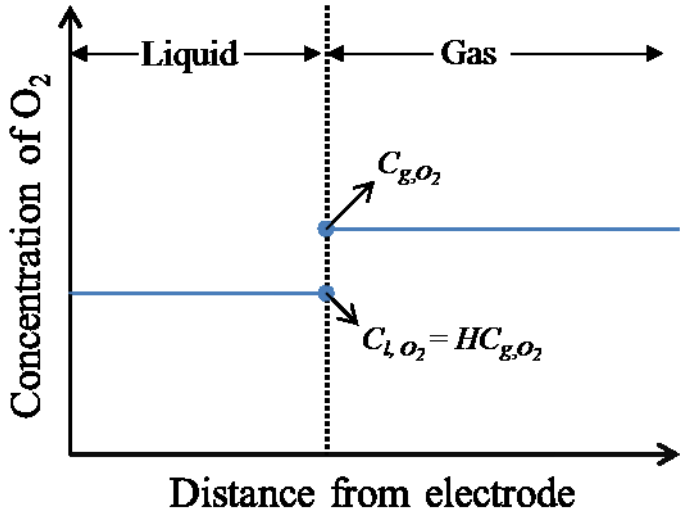

Figure 4.9 Schematic of concentration profile for O_2 at gas-liquid interphase.

The concentration of O_2 partitions at gas-liquid interphase according to following relation.

$$C_{l,O_2} = HC_{g,O_2} \tag{4.1}$$

where C_{g,O_2} and C_{l,O_2} are the O_2 concentration in gas phase and liquid phase respectively. Henry's constant is calculated for 0.1 M KOH at 60 °C by assuming the O_2 solubility as $0.65 \cdot 10^{-6}$ mol · cm^{-3} [15]. After obtaining Henry's constant, other values of O_2 solubility in liquid electrolyte at various partial pressure of O_2 in gas are generated as shown in Figure 4.10. Similarly, i_L can be calculated for each of these concentrations from Equation (1.10).

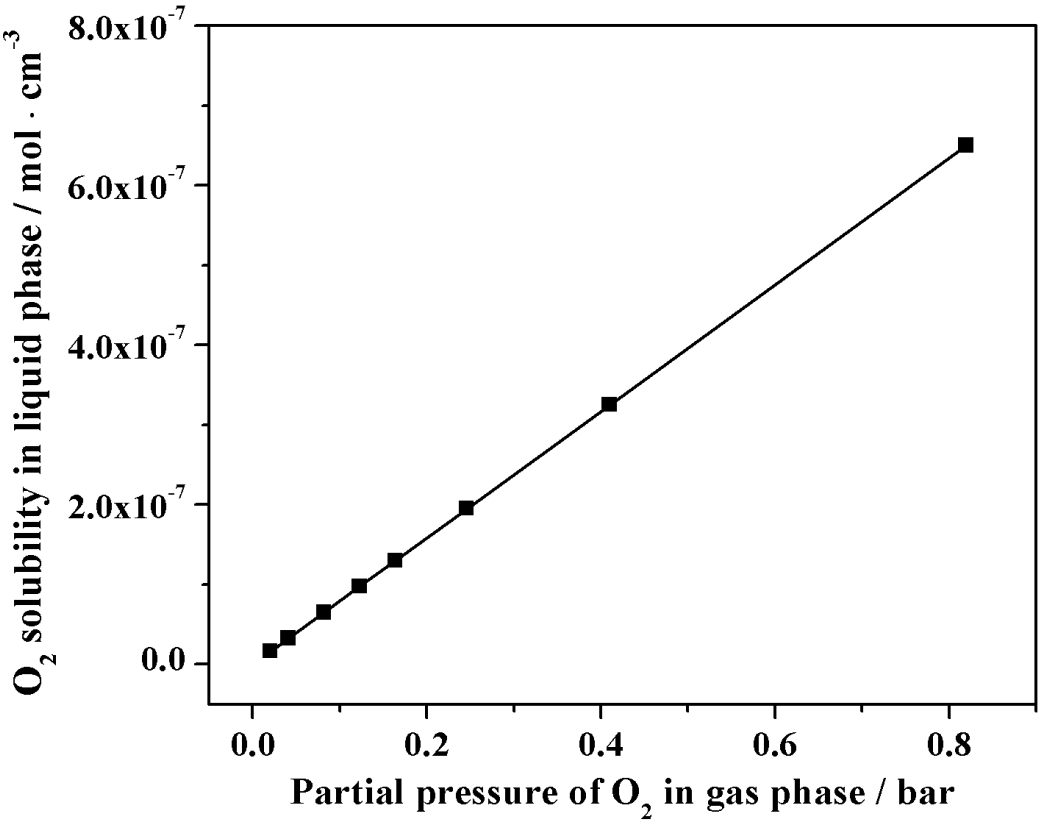

Figure 4.10 O_2 solubility in liquid electrolyte plotted against O_2 partial pressure in gas phase at 60 °C in 0.1 M KOH.

Figure 4.11 shows a plot of iR corrected overpotential *vs* current normalized to mass of Pt with varying O_2 bulk concentration in 0.1 M KOH. As expected the limiting current with respect to Pt at η = 0.275 V reduces proportionally with O_2 bulk concentration.

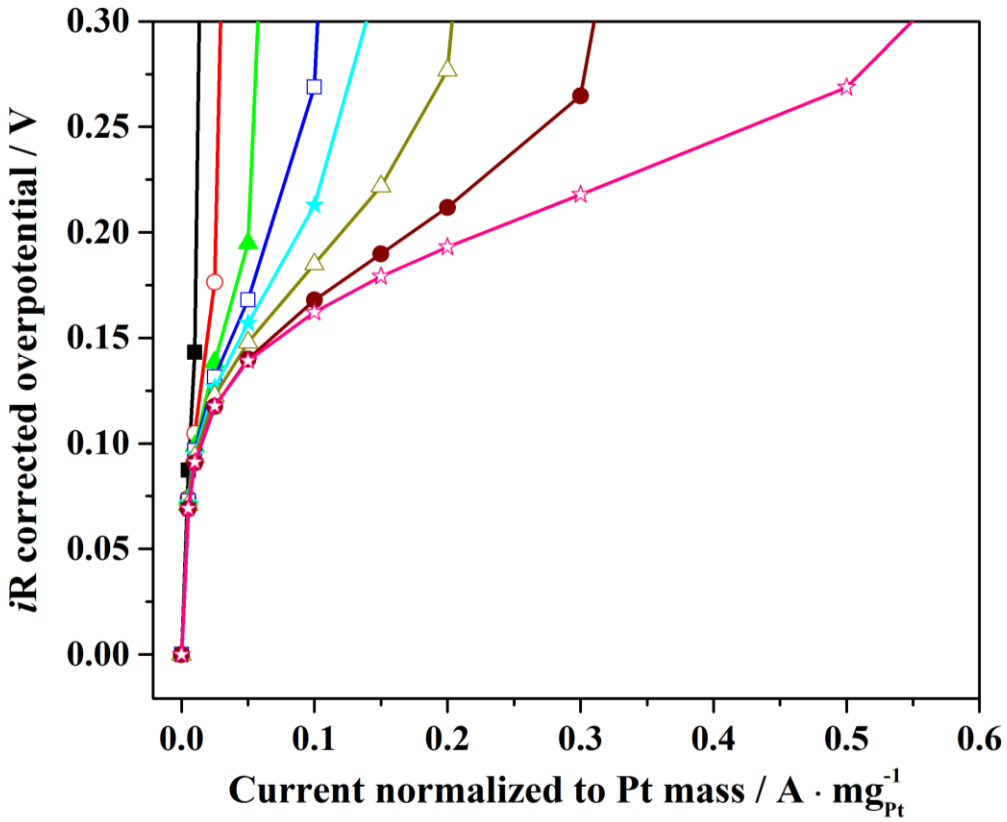

Figure 4.11 Current normalized to Pt mass plotted against *i*R corrected over potential at various O_2 solubility for GC coated with 5 $\mu g_{Pt} \cdot cm^{-2}$ rotating at 1600 rpm in 0.1 M KOH at 60 °C: $1.62 \cdot 10^{-8}$ mol · cm^{-3} (solid square); $3.25 \cdot 10^{-8}$ mol · cm^{-3} (empty circle); $6.5 \cdot 10^{-8}$ mol · cm^{-3} (solid triangle); $9.75 \cdot 10^{-8}$ mol · cm^{-3} (empty square); $13 \cdot 10^{-8}$ mol · cm^{-3} (solid star); $19.5 \cdot 10^{-8}$ mol · cm^{-3} (empty triangle); $32.5 \cdot 10^{-8}$ mol · cm^{-3} (solid circle); $65 \cdot 10^{-8}$ mol · cm^{-3} (empty star).

Once the limiting current is known for all the concentrations, i_k can be determined from Equation (1.13). Tafel plots for all concentrations are shown in Figure 4.12. From slope and intercept of these plots the charge transfer coefficient, α and exchange current, i_0 can be determined using Equation (2.16) as described in Section 2.1.3. Notice that intercept and slope of all the curves are similar, indicating exchange current and charge transfer value are nearly independent of O_2 concentration. Similar charge transfer coefficient values suggest that the reaction mechanism does not change for range of O_2 concentration used here. The invariance of exchange current with respect to O_2 concentration is explained as follows.

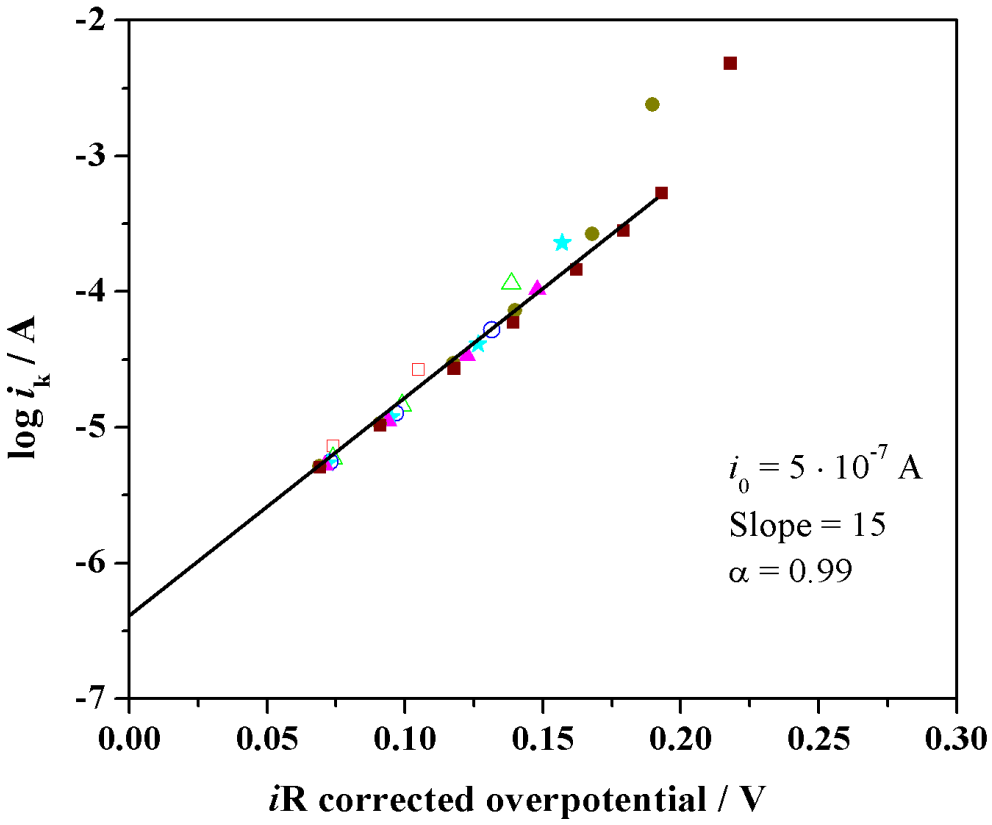

Figure 4.12 Tafel plot for GC coated with 5μg_{Pt} · cm^{-2} at 1600 rpm, 60 °C at various O_2 solubility: 1.62 · 10^{-8} mol · cm^{-3} (empty star); 3.25 · 10^{-8} mol · cm^{-3} (empty square); 6.5 · 10^{-8} mol · cm^{-3} (empty triangle); 9.75 · 10^{-8} mol · cm^{-3} (empty circle); 13 · 10^{-8} mol · cm^{-3} (solid star); 19.5 · 10^{-8} mol · cm^{-3} (solid triangle); 32.5 · 10^{-8} mol · cm^{-3} (solid circle); 65 · 10^{-8} mol · cm^{-3} (solid square).

ORR may proceed with involving one or more adsorbed intermediates and overall reaction rate is influenced by coverage of these intermediates. Depending on whether the rds is adsorption or desorption, the rate may be proportional either to blocked surface or free surface. Since here the rate is not a function of O_2 concentration and C_{H_2O} is kept constant for all the experiments, the rate is proportional to adsorbed oxygen, θ_{O_2}. By introducing a rate constant k_f with respect to C_{O_2}, according to Equation (2.12) the exchange current for ORR can be given as

$$i_0 = nFAk_f C_{e,H_2O}\, \theta_{e,O_2} e^{-\alpha_f f(E_{eq}-E^{o\prime})} \tag{4.2}$$

where C_{e,H_2O} and θ_{e,O_2} are equilibrium concentration of water and coverage of O_2 respectively. Since C_{H_2O} is in excess relative to C_{O_2}, C_{H_2O} ~C_{e,H_2O}. The coverage θ_{e,O_2} in Equation (4.2) can be defined in terms of Frumkin [99] or Temkin [100] [101] isotherm, as

both approach lead to similar equation. Temkin assumed that adsorbing molecules have no interaction between themselves and electrode has different planes with different energy of adsorption. Frumkin assumed that there is lateral interaction between adsorbing molecules and the tendency for adsorption reduces as the coverage increases. In this study polycrystalline Pt consisting of different crystalline planes is used and hence Frumkin-Temkin isotherm can be applied to get the values of θ. When 0.2< θ <0.8, Temkin isotherm is given by [102]

$$\theta_{O_2} = \frac{RT}{2g\Gamma_s} ln\left(KC_{O_2}\right) \tag{4.3}$$

where Γ_s is surface excess of O_2 at saturation, $\theta_{O_2} = \frac{\Gamma_{O_2}}{\Gamma_s}$, Γ_{O_2} is the surface excess, K is the equilibrium constant and g is a constant in J · mol^{-1} which defines the way heat of adsorption reduces linearly for particular system with increase in the coverage. According to Equation (4.3) at constant overpotential, θ_{O_2} is proportional to $ln(C_{O_2})$. This suggests that θ_{O_2} varies only 1.2 times for change in C_{O_2} by one order and explains the invariance of exchange current with oxygen concentration.

The determined value of α_f and i_0 from Tafel slope are 1 and 5 · 10^{-7} A respectively. Subsequently the exchange current density with respect to ECSA of Pt is 3.33 · 10^{-6} A · cm$_{\mathrm{Pt}}^{-2}$ and with respect to mass of Pt is 5 · 10^{-4} A · mg$_{\mathrm{Pt}}^{-1}$. The ECSA of Pt in alkaline media is 15 m^2 · g^{-1} obtained from CV of GC coated with 5μg$_{\mathrm{Pt}}$ · cm^{-2} in N_2 saturated electrolyte with procedure described in Section 2.2.2.

4.1.5 Rate expression

From Equation (1.13)

$$i = \frac{i_k i_L}{(i_k + i_L)} \tag{4.4}$$

Inserting $i_k = -i_0 e^{-\alpha_f f \eta_k}$ from Equation (2.15), $i_L = nFA\left(\frac{D}{\delta}\right)C_{O_2}$ from Equation (1.11) and defining$i'_L = nFAD/\delta$, Equation (4.4) becomes,

$$i = -\frac{i_0 e^{-\alpha_f f \eta_k} i'_L C_{O_2}}{(i'_L C_{O_2} - i_0 e^{-\vec{\alpha} f \eta_k})} \tag{4.5}$$

where $i_0 = nFAk_f \theta_{e,O_2} e^{-\alpha_f f (E_{eq} - E^{o\prime})}$ from Equation (4.2).

To check the validity of Equation (4.5), ORR curves are measured at various O_2 concentrations. Figure 4.13 shows a iR corrected plot of current versus O_2 concentration at various applied overpotential. Here the applied overpotential, $\eta = \eta_k + \eta_{mt}$ where η_{mt} can be given as

$$\eta_{mt} = \frac{1}{nf} ln\left(\frac{i_L - i}{i_L}\right) \tag{4.6}$$

For ORR on Pt, n = 4 and at 60 °C, f = 34.85 V^{-1}. The values of η_{mt} can be neglected for $\eta \geq 0.1$ V and when $i < 0.4\ i_L$ and hence $\eta \sim \eta_k$ for overpotential shown in Figure 4.13. Fitting curves according to Equation (4.5) are shown by solid lines. The fitting curves fit fairly well to the experimental data. The results from fitting are shown in

Table **4.1**. For all overpotential α_f = 1, f = 34.85 V^{-1}. It can be seen that the i_0 values at all overpotential and O_2 concentrations are nearly constant. The value of i'_L also agrees well with the limiting current found in earlier experiments as shown in Figure 4.7. For example, for experimental data shown in Figure 4.7, C_{O_2}= $65 \cdot 10^{-8}$ $mol^{-1} \cdot cm^3$ and i_L/C_{O_2}= i'_L = 680 ± 20 $A \cdot cm^3 \cdot mol^{-1}$ which is well within the range of data shown in

Table **4.1**. Hence Equation (4.5) can be used to represent the steady state ORR kinetics on Pt in alkaline media. Furthermore it can also be used to predict diffusion controlled limiting current when exchange current and charge transfer coefficient is known.

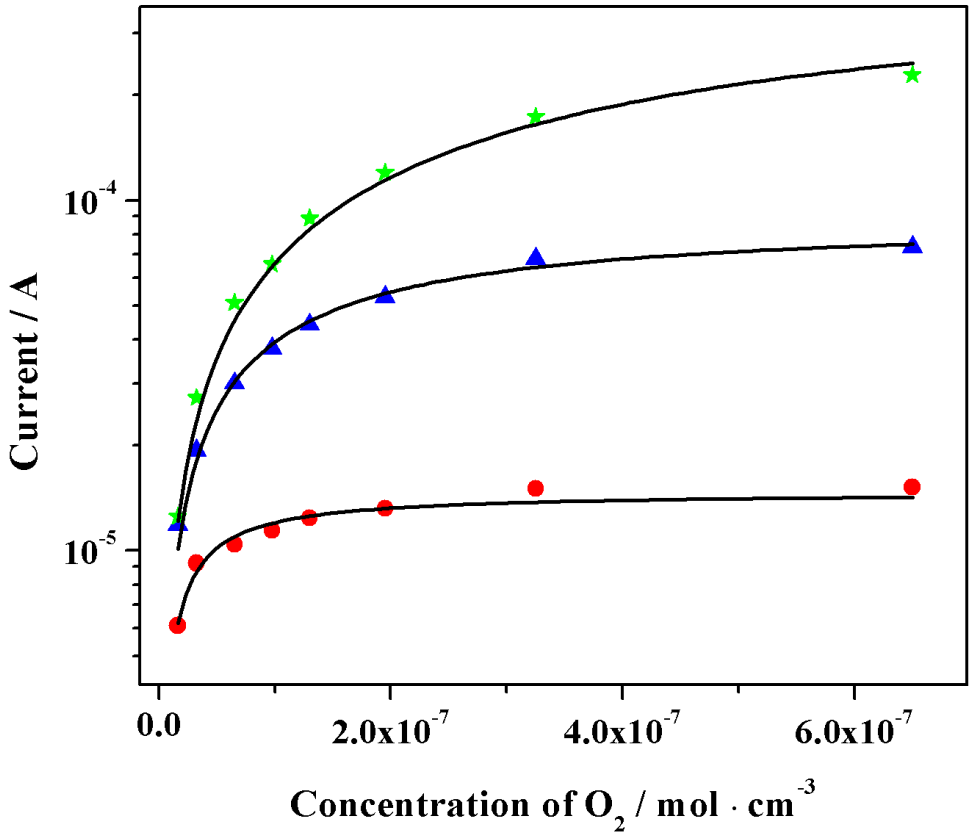

Figure 4.13 Current variations with respect to O_2 concentration at various overpotential 0.1 V (circle); 0.15 V (triangle); 0.2 V (star) for GC coated with 5 $\mu g_{Pt} \cdot cm^{-2}$ at 1600 rpm, 60 °C in 0.1 M KOH.

Table 4.1 Fitting parameter for curves according to Equation (4.5) as depicted in Figure 4.13

Overpotential / V	$i_0 \cdot 10^7$ /A	i'_L / A · cm^3 · mol^{-1}
0.1	4.5	660 ± 70
0.15	4.81	702 ± 47
0.20	4.6	764 ± 31

4.2 *Kinetic loss measured in AMFC*

As discussed in Section 1.2.1 the performance of H_2-O_2 AMFC is determined by combination of several losses such as kinetic loss, ohmic loss and mass transport loss of anode and cathode. As a first step, anode and cathode performance can be resolved to determine if either of these electrodes is much more limiting than other electrode. In literature attempts to resolve the AMFC performance into anode and cathode is scarce and there is no clear quantitative indication to show whether anode or cathode is the limiting electrode (see section 1.5). Moreover the AMFC and PEMFC have been compared at loadings > 0.5 $mg_{Pt} \cdot cm^{-2}$. At these loadings the currents in kinetic region can be a non-linear function of loading as pointed out is Section 4.1.2 due to difference in catalyst utilization. The evaluation procedure is more systematic when the performance is evaluated within the range of catalyst loading where the current increases linearly with loading. This ensures that the catalyst utilization is maximum and is unaffected by changes in the loading and then currents normalized to loadings can be used to infer further findings. Therefore in this study MEAs are prepared with low loadings of catalyst to resolve anode and cathode over potential.

Even with MEAs employing low loadings, the resolution may become difficult if the mass transport losses, for example anode flooding is dominant right from the beginning of the kinetic region. In AMFC water can accumulate in anode due to the anodic reaction and from electro-osmotic drag of water from cathode to anode. This may cause anode flooding even at very low currents. The dominancy of flooding in kinetic region can be inferred from the polarization curve by observing change in potential with respect to current i.e. dE/dI. It is well known from PEMFC literature [103] that flooding is characterized by sudden drop in polarization curve i.e. $|dE/dI|$ abruptly increases as the current increases. The kinetic region of polarization curve is characterized by gradual decrease in $|dE/dI|$ and ohmic region is characterized by constant $|dE/dI|$ as the current increases. If $|dE/dI|$ of a given region in the overall polarization curve decreases as the current increases, flooding effects can be assumed negligible in this region. Several research groups [36] [104] [28] observed abrupt drop in AMFC performance at low currents. Zeng *et al.* [36] and Zhang *et al.* [104] attributed this performance drop to flooding. Zhang *et al.* [104] showed that when AMFC is operated with 95% RH at anode and cathode, flooding can become dominant at currents as low as 0.022 $A \cdot cm^2$. However they also showed that this current limit can be further extended to 0.087 $A \cdot cm^2$ by employing a membrane with

better water transport. The determined water flux through their in-house prepared membrane at 25°C was ~110 mol · μm · m^{-2} · h^{-1}. On the contrary several other research papers [18] [19] [105] employing high gas flow rates ≥ 40 mL · cm^2 · min^{-1} at anode and cathode observed no abrupt drop in polarization curve for currents < 0.6 A · cm^{-2} even though RH of anodic and cathodic gas was ≥ 95%. This suggests that higher gas flow rates aid in removal of excessive water produced in anode and avoids drying out of cathode.

In all the following polarization curves flooding of electrodes was ruled out for at least until currents < 0.2 A · cm^2 because (a) very high gas flow rates (RH 80%) equal to 125 mL · cm^2 · min^{-1} was used at anode and cathode (see section 2.3.4) (b) we observed decrease in $|dE/dI|$ in the polarization curves (c) water flux through our membrane was ~ 49 times (see section 3.1) larger than reported by Zhang *et al.* [104].

4.2.1 HOR kinetic losses measured in AMFC

HOR kinetic analysis were carried out in AMFC with Type-1 MEAs (see Section 2.3.4) with low loadings 0.07 and 0.107 mg_{Pt} · cm^{-2}. No direct measurements of HOR kinetic losses have been made in AMFC until now. However, from HOR/HER measurements in RDE set up in 0.1M KOH at 80°C, Sheng *et al.* [37] predicted an overpotential of 0.15V for HOR in AMFC when current is equal to 1.5 A · cm^{-2}, loading is 0.05 mg_{Pt} · cm^{-2} and temperature is 80°C. Figure 4.14 shows the $i - E$ curve for two MEAs with varying catalyst loading at anode. Both curves are nearly identical and we observe an overall potential drop of 0.5V at 0.2 A · cm^{-2}. Using values reported by Sheng *et al.* [37] i.e. η_k = -0.15V, i_k = 1.5 A · cm^{-2}, we can predict the overpotential at 0.2 A · cm^{-2} due to HOR kinetics in our polarization curves.

At η_k = -0.15V, i_k = 1.5 A · cm^{-2} and α_f = 0.5, i_0 from Equation (2.15) is equal to 0.127 A · cm^{-2}. Since i_0 is directly proportional to loading when the catalyst utilization is complete, i_0 for 0.07 mg_{Pt} · cm^{-2} scales to 0.178 A · cm^{-2}. Substituting i_k = 0.2 A · cm^{-2} and i_0 = 0.178 A · cm^{-2} in Equation (2.15), η_k is equal to -0.0071V. So it can be seen that only 0.0071V of potential drop is expected from HOR when current is 0.2 A · cm^{-2} and loading is 0.07 mg_{Pt} · cm^{-2}. For higher loadings this potential drop would be even lower. Hence in our polarization curves the potential drop due to HOR kinetics is considered to be negligible at 0.2 A · cm^{-2}. Therefore it is assumed that HOR kinetics is fast and can be

considered as a dynamic reference electrode similar to PEMFC at least for current ≤0.2 A · cm^{-2}.

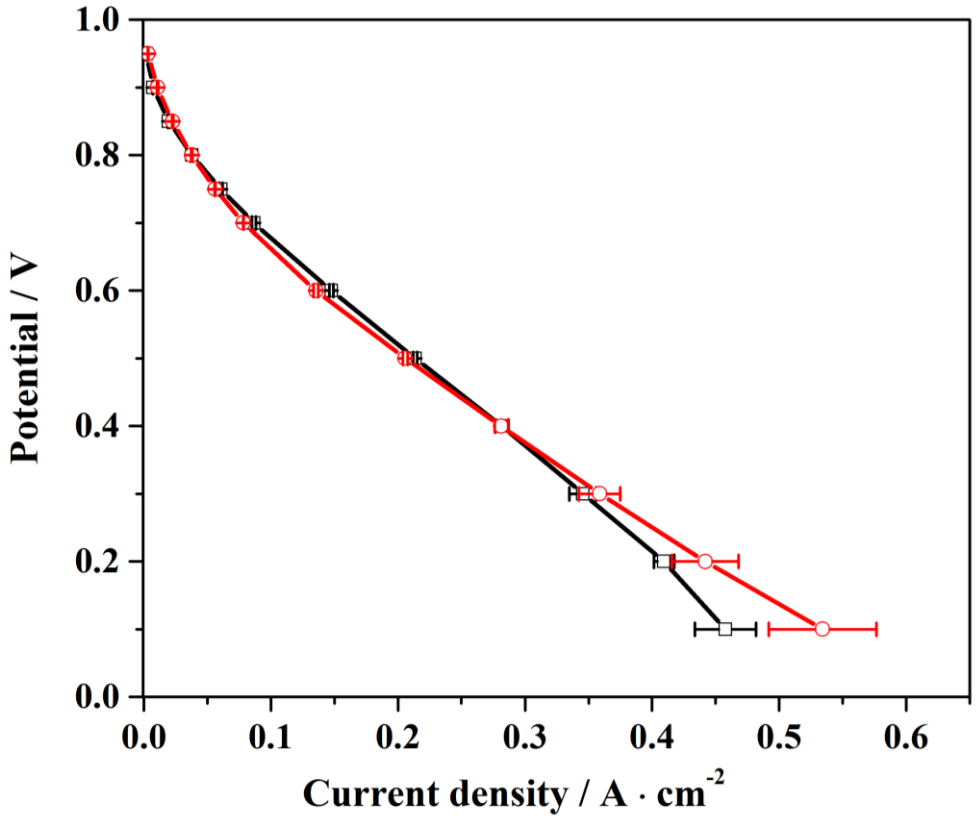

Figure 4.14 Polarization curves for Type-1 MEAs at 60°C with varying anode loading and cathode loading: anode-0.07 mg_{Pt} · cm^{-2}/ cathode-0.107 mg_{Pt} · cm^{-2} (empty square); anode - 0.107 mg_{Pt} · cm^{-2} / cathode - 0.107 mg_{Pt} · cm^{-2} (empty circle). Error bar represents deviation from two independent experiments.

4.2.2 ORR kinetic losses measured in AMFC

Unlike insensitivity of performance towards change in anode loading, the performance was found to be extremely sensitive to change in cathode loading as shown in Figure 4.15. The performance of MEAs differs from each other throughout the $i - E$ curve. To determine the catalyst utilization, these curves are normalized to mass of Pt as shown in Figure 4.16. The deviation of MEA with cathode loading of 0.07 mg_{Pt} · cm^{-2} to other MEAs (see inset) is most likely to be caused by in-complete catalyst utilization due to electrical isolation of some catalyst particles. At extremely low loadings the density of the catalyst particles is low which can lead to some of the catalyst particles to be electrically isolated from GDL or from the main CL network. However this issue is resolved when the cathode loading is

increased to 0.107 $mg_{Pt} \cdot cm^{-2}$. The normalized curve for MEAs with cathode loading 0.107 and 0.16 $mg_{Pt} \cdot cm^{-2}$ merge excellently until 0.5 V indicating complete utilization of catalyst.

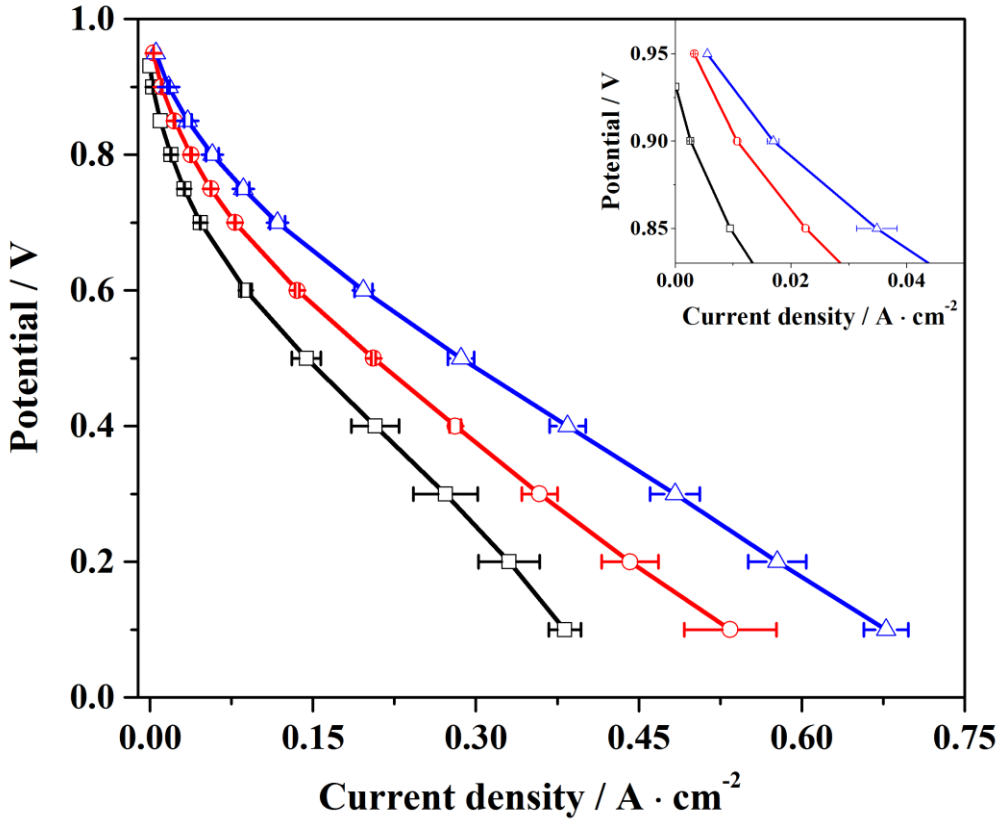

Figure 4.15 Polarization curves for Type-1 MEAs at 60 °C with varying cathode loading and constant anode loading: anode - 0.107 $mg_{Pt} \cdot cm^{-2}$ / cathode - 0.07 $mg_{Pt} \cdot cm^{-2}$ (square); Anode - 0.107 $mg_{Pt} \cdot cm^{-2}$ / cathode - 0.107 $mg_{Pt} \cdot cm^{-2}$ (circle); anode - 0.107 $mg_{Pt} \cdot cm^{-2}$ / cathode - 0.16 $mg_{Pt} \cdot cm^{-2}$ (triangle). Inset: enlarged view of the low overpotential region.

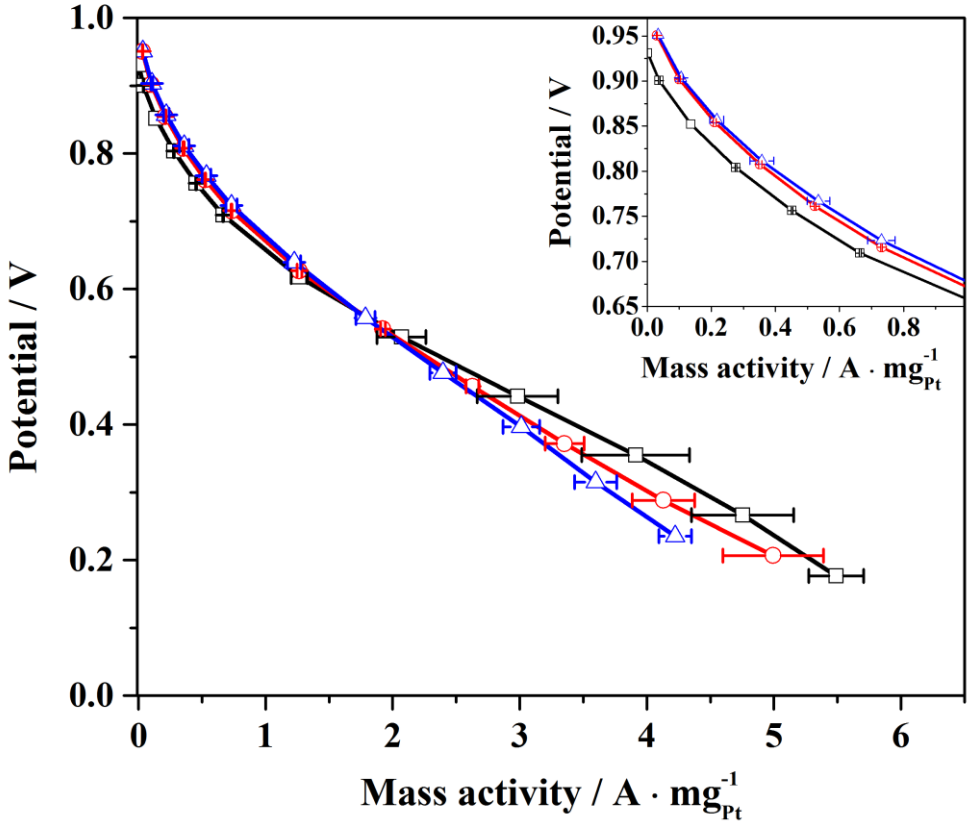

Figure 4.16 Normalized polarization curves for various Type-1 MEAs with varying cathode loading and constant anode loading: anode - 0.107 $mg_{Pt} \cdot cm^{-2}$ / cathode - 0.07 $mg_{Pt} \cdot cm^{-2}$ (square); anode - 0.107 $mg_{Pt} \cdot cm^{-2}$ / cathode - 0.107 $mg_{Pt} \cdot cm^{-2}$ (circle); anode - 0.107 $mg_{Pt} \cdot cm^{-2}$ / cathode - 0.16 $mg_{Pt} \cdot cm^{-2}$ (triangle). Inset: enlarged view of the low to medium overpotential region.

As complete utilization of catalyst is obtained with Pt loading 0.107 $mg_{Pt} \cdot cm^{-2}$, AMFC and PEMFC MEAs are evaluated for comparative purpose with this loading at similar operating conditions as shown in Figure 4.17. As it can be seen from inset, the AMFC performance is lower than the PEMFC performance at all overpotential. It was shown above that HOR kinetics are fast in AMFC, so this limitations must come from cathode. This observation is counter-intuitive when it is considered that ORR on Pt in alkaline media has better or similar reaction rate than in acidic media as often described in literature. This suggests that further investigation of ORR kinetics is required to find the limitations in AMFC.

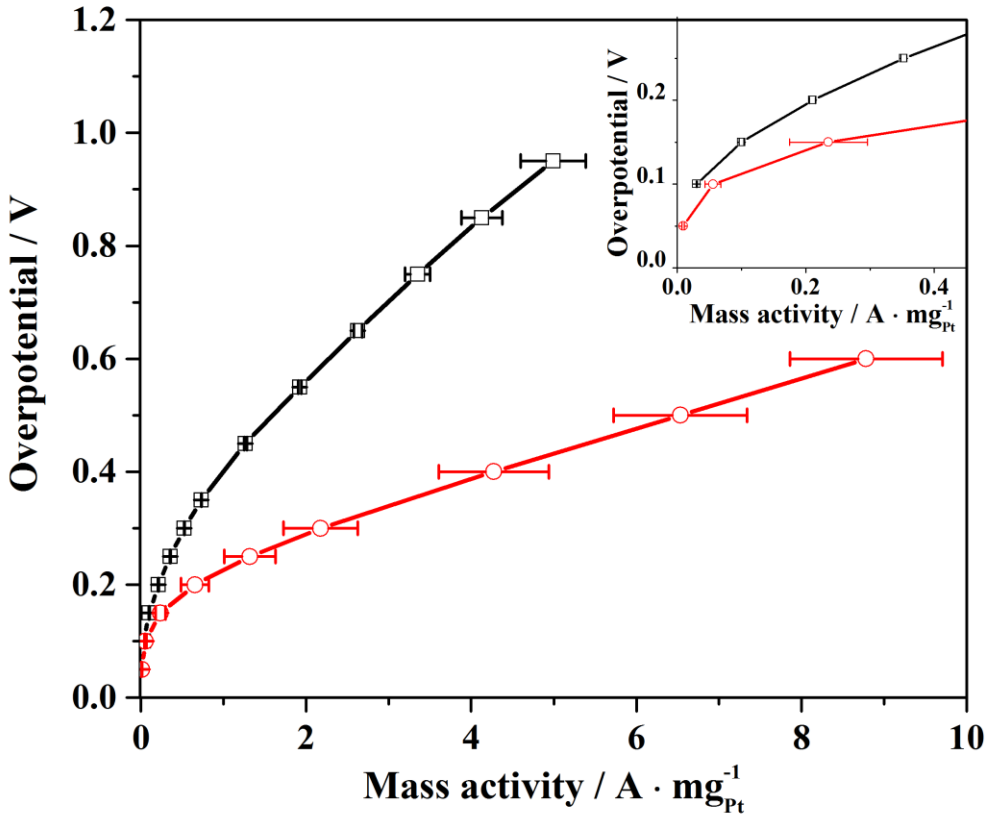

Figure 4.17 Comparative normalized $i - \eta$ curves of AMFC and PEMFC Type-1 MEAs measured a 60 °C with anode - 0.107 $mg_{Pt} \cdot cm^{-2}$/ cathode - 0.107 $mg_{Pt} \cdot cm^{-2}$ loadings: AMFC (square); PEMFC (circle). Inset: enlarged view of low overpotential region.

Figure 4.18 shows the Tafel plots for AMFC and PEMFC. Nearly similar intercept values are observed for both curves suggesting similar value of exchange current. However the charge transfer coefficient calculated from slope of Tafel plot is higher for PEMFC than AMFC. The values of exchange current and charge transfer coefficient for AMFC and PEMFC are tabulated in Table 4.2 together with values obtained at RDE.

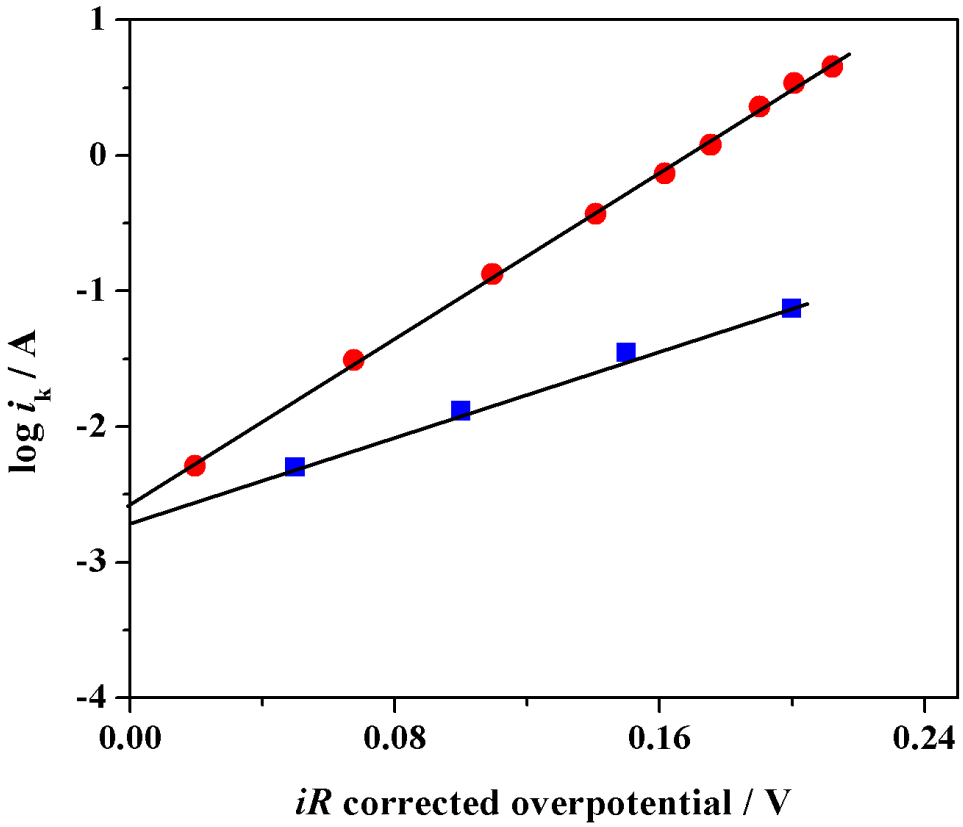

Figure 4.18 Tafel plot for AMFC and PEMFC Type-1 MEAs employing 0.107 $mg_{Pt} \cdot cm^{-2}$ loading at anode and cathode operating at 60 °C: AMFC (square); PEMFC (circle).

Table 4.2 Kinetic parameters of ORR on Pt measured in 0.1 M KOH, AMFC and PEMFC.

Parameter	0.1 M KOH	AMFC	PEMFC
i_0 / A	$5 \cdot 10^{-7}$	$2.2 \pm 0.6 \cdot 10^{-3}$	$3 \cdot 10^{-3}$
Normalized i_0 / $A \cdot mg_{Pt}^{-1}$	$5 \cdot 10^{-4}$	$5.1 \pm 1.4 \cdot 10^{-3}$	$7 \cdot 10^{-3}$
α	1	0.5	1

4.3 *Rate determining step and ORR pathway*

Table 4.2 shows the kinetics parameters for ORR in 0.1 M KOH, in AMFC and in PEMFC. The charge transfer coefficient for obtained at PEMFC and ORR measured in 0.1 M KOH is two times higher than what is measured in AMFC. As the kinetic current depends strongly on charge transfer coefficient due to exponential dependency, the kinetic current is significantly lower in AMFC compared to PEMFC. In literature often the value of charge transfer coefficient obtained from Tafel slope is used to find the possible rds. However, many possible interpretations with each value of α_f are possible. For example, for a multistep reaction, $\alpha_f = \frac{\gamma}{\lambda} + r\beta$ [44], where $\gamma + 1$ is the step number of rds, λ is the number of times rds is repeated and $r = 0$ for a chemical rds and $r = 1$ for a charge transfer rds. For $\alpha_f = 1$, $\beta = 0.5$ and $n = 4$, three rds can be postulated as follows a) 2nd chemical step b) 2nd charger transfer step repeated two times and c) 3rd chemical step repeated two times. Therefore such drastic possibilities leave much uncertainty in determining rds from mere α_f values. Hence the data from other experiments such as current behavior measured with respect to O_2 concentration allows one to understand more about the reaction pathway. In this work, these experiments revealed that the exchange current is independent of O_2 concentration suggesting the high probability of appearance of O_{2ad} in the rds. Yet despite these clues, there is still large number of ways in which reaction pathway might be represented, hence to find the actual reaction pathway, information from additional experiments such as experiments by spectroscopic methods are needed.

Chapter 5
Ohmic Losses[5]

The ohmic loss in fuel cell can arise from ionic resistance of membrane and CL, electronic resistance of CL and external wires connecting fuel cell to measuring device. Electronic resistance contribution is found to be much smaller than ionic resistance. Therefore the major portion of ohmic loss comes from ionic resistance of membrane and CL. While measurement of ionic resistance of membrane is quite simple with use of high frequency impedance, the measurement of ionic resistance of CL is not straight forward and is often calculated indirectly from impedance spectra, ex-situ CL or by modifying the MEA.

5.1 *Catalyst layer conductivity*

In order to find the contribution of catalyst layer ionic resistance to the overall polarization loss, CL conductivity was determined using the method employed by Boyer *et al.* [107]. Due to presence of ionomer and catalyst particles in CL, the CL exhibits mixed conductivity during the reaction which is often difficult to separate by conventional impedance spectroscopy. Therefore a modified IL-MEA was prepared (see Section 2.3.4) by sandwiching an inert layer (reaction-free) of carbon-ionomer composite between the cathode and membrane to form Anode-Membrane-Inert layer-Cathode assembly as shown in Figure 2.7 (right).

[5] Part of the results in this Chapter published in P.S. Khadke, U. Krewer, *Electrochem. Comm*. 51 (**2015**) 117-120.

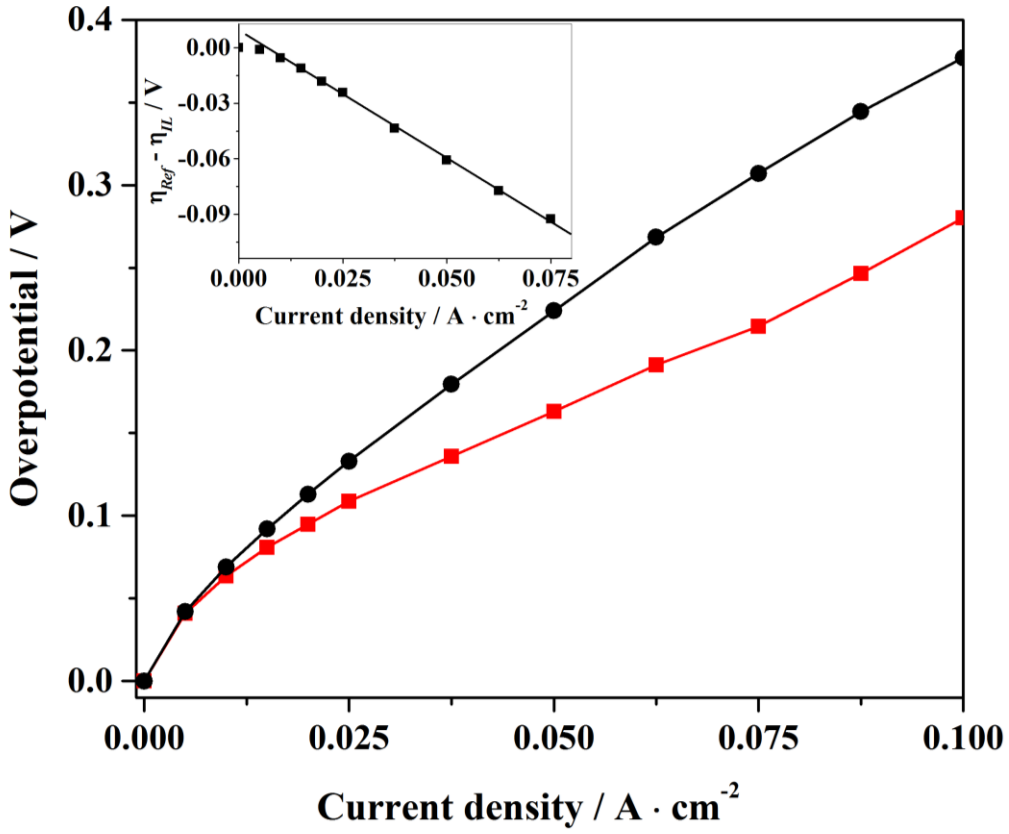

Figure 5.1 Polarization curves with anode - 0.86 $mg_{Pt} \cdot cm^{-2}$ / cathode - 0.86 $mg_{Pt} \cdot cm^{-2}$ loadings: Type-2 Ref-MEA (square) and Type-2 IL-MEA (circle). Inset: linear fit of over-potential difference of Ref-MEA and IL-MEA, $(\eta_{Ref} - \eta_{IL})$ *vs* current density.

The ionomer in inert layer adds resistance to the ionic conduction path between cathode and anode, whereas the function of carbon is to establish a comparable morphology as in the catalyst layer. The effect of inert layer on the performance is evaluated and CL ionic resistance can be determined from polarization curves. Figure 5.1 shows performance curves for MEAs with (IL-MEA) and without inert layer (Ref-MEA). The performance of IL-MEA is clearly lower than the Ref-MEA. In general the low performance of IL-MEA can be attributed to additional ionic resistance offered by inert layer since other losses such as kinetic and mass transport losses in both these MEAs are expected to be similar. From the slope of this plot the ionic conductivity of inert layer can be calculated as,

$$\sigma = \frac{l_{Ref} - l_{IL}}{m} \tag{5.1}$$

where m is the slope in $\Omega \cdot cm^{-2}$, l_{Ref} is the thickness of CL of Ref-MEA and l_{IL} is the thickness of CL plus inert layer of IL-MEA in cm, and σ is the conductivity in $mS \cdot cm^{-1}$.

The measured thickness difference between the Ref-MEA and IL-MEA was 51.2 μm and the determined conductivity of the inert layer is 3.9 $mS \cdot cm^{-1}$.

Table 5.1 Ionic conductivity values for catalyst layer and membrane employed in AMFC and PEMFC.

Composite	Conductivity $mS \cdot cm^{-1}$	Operating conditions	Reference
50 % AS-4 : 50% carbon	3.9	Fuel cell mode: 60 ºC	This work
33 % Nafion : 67% carbon	13	Fuel cell mode: 50 ºC	[107]
60 % Nafion : 40% carbon	18	Fuel cell mode: 50 ºC	[107]
Recast 25 % Nafion : 75% silica	10	80 ºC	[32]
Recast AS-4	13	40 ºC	[17]
Recast Nafion	100	80 ºC	[108]
A201 membrane	15	Fuel cell mode: 60 ºC	This work
A201 membrane	42	23 °C	[17]
Nafion membrane	80 - 100	25 ºC	[109]

Table 5.1 shows the ionic conductivity values of other composite layers available in the literature. The ionic conductivity of inert layer comprising cation Nafion ionomer is ~ 4 times higher than inert layer comprising of AS-4 anion ionomer at fairly similar operating conditions. Assuming, the ionic conductivity of the AMFC CLs is similar to the obtained conductivity of inert layer in this work, the AMFC curves of Figure 4.17 are iR corrected for anode and cathode catalyst layer ionic resistance after iR correcting it for membrane resistance. The resultant curves are as shown in Figure 5.2. The iR correction for PEMFC is carried out by assuming the membrane and CL resistance values shown in Table 5.1.

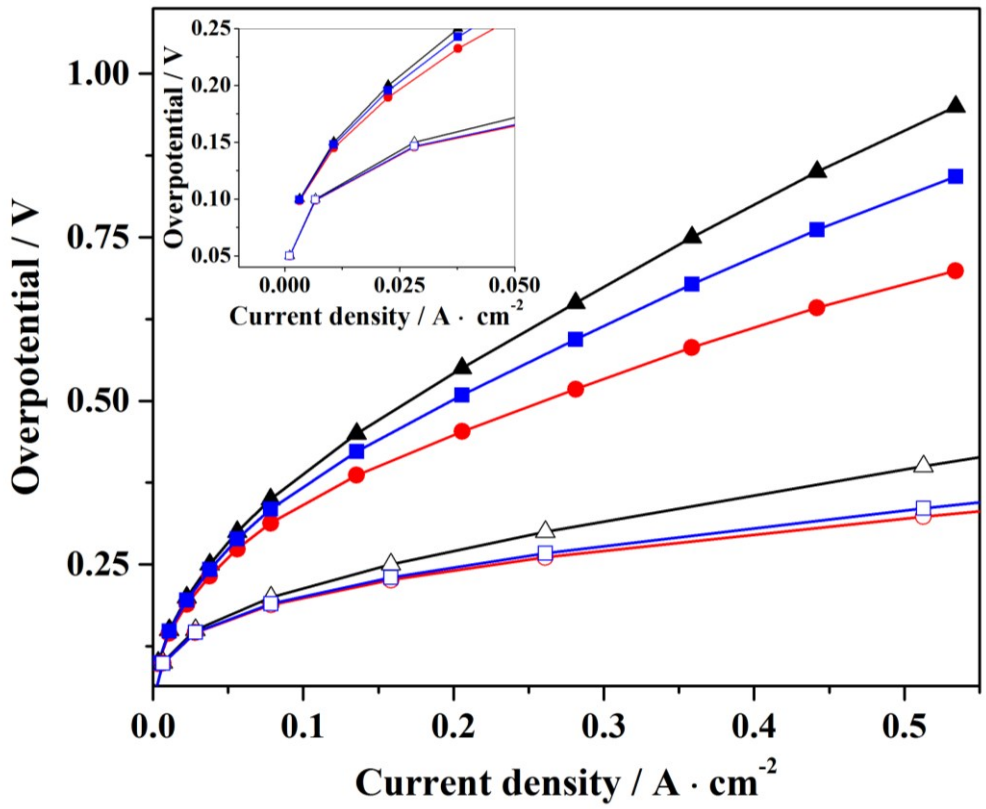

Figure 5.2 iR corrected polarization curves for AMFC and PEMFC Type-1 MEAs at 60 °C with anode - 0.107 $mg_{Pt} \cdot cm^{-2}$ / cathode - 0.107 $mg_{Pt} \cdot cm^{-2}$ loadings: measured AMFC $i - E$ curve (solid triangle); AMFC $i - E$ curve corrected for membrane resistance (solid square); AMFC $i - E$ curve corrected for catalyst layer and membrane resistance (solid circle): measured PEMFC $i - E$ curve (empty triangle); PEMFC $i - E$ curve corrected for membrane resistance (empty square); PEMFC $i - E$ curve corrected for catalyst layer and membrane (empty circle).

The performance of AMFC is lower than PEMFC throughout the $i - E$ curve even after iR correction for membrane and CL. It can be seen that the ohmic loss in the performance curve is significantly higher for AMFC compared to PEMFC. Despite 4.5 times thinner membrane used in AMFC the potential loss due to the membrane resistance in AMFC is 1.3 times higher than PEMFC. In addition, the potential loss due to CL resistance in AMFC is 9 times higher than potential loss in PEMFC due to the similar thickness of CL in both the MEAs. The performance loss due to CL resistance *i.e* the difference between the $i - E$ curve iR corrected for membrane resistance and $i - E$ curve iR corrected for membrane plus CL resistance, is the maximum possible loss. However, in reality this loss will be somewhere between this difference and zero depending on the location of reaction zone in CL..

Chapter 6
Summary, Conclusions and Perspective

In this Thesis, the performance limiting factors in AMFC is systematically evaluated for quantitative determination of contribution from kinetic, ohmic and mass transport losses. ORR studies in RDE, revealed the dependency of kinetic parameters with respect to catalyst loading and diffusion controlled limiting current. Towards this, a procedure for determining the limiting current with respect to Pt at low loadings of Pt/C is exposed by subtracting the influence of carbon activity. The separation of carbon activity is essential for precise extraction of kinetic parameters with respect to Pt. After the successful determination of kinetic parameters, a rate expression for ORR on Pt in alkaline media at elaborate concentration of O_2 is presented, which is shown to predict limiting current fairly well.

In AMFC the HOR kinetics are found to be fast and limitation to the overall polarization loss when compared to PEMFC mainly arises from lower ORR rate, larger ohmic loss from membrane and CL ionic resistance and much lower limiting current. The lower limiting current is due to high rate of water consumption at the cathode by cathodic reaction and water drag from cathode to anode. From these findings, the overall performance loss is successfully separated into individual contributions as shown in Figure 6.1 from the following relations,

$$\eta_{overall,AMFC} = \eta_{k,AMFC} + \eta_{iR,AMFC} + \eta_{mt,AMFC} \quad (6.1)$$

$$\eta_{k,AMFC} = \frac{1}{\alpha_f f} ln\left(\frac{i_k}{i_0}\right) \tag{6.2}$$

$$\eta_{iR,AMFC} = iR_{mem} + iR_{CL} \tag{6.3}$$

$$\eta_{mt,AMFC} = \frac{1}{nf} ln\left(\frac{i_L - i}{i_L}\right) \tag{6.4}$$

with values found in this work, α_f = 0.5, i_0 = 0.0022 A, f = 34.85 V^{-1}, R_{mem} = 0.05Ω, R_{CL} = 0.02Ω, n = 2/9 and i_L = 0.6 A.

$$\eta_{k,PEMFC} = \frac{1}{\alpha_f f} ln\left(\frac{i_k}{i_0}\right) \tag{6.5}$$

with α_f = 1, i_0 = 0.003 A, f = 34.85 V^{-1}

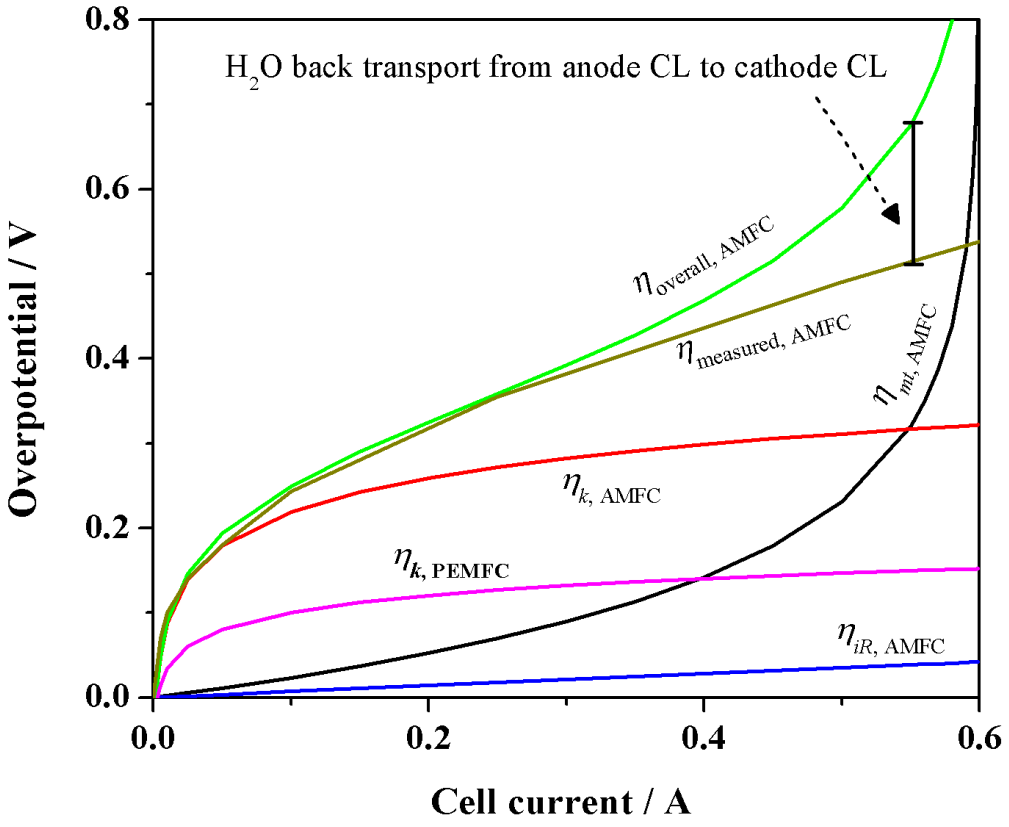

Figure 6.1 Overall performance loss in AMFC.

Even though the exchange current for AMFC and PEMFC are similar, $\eta_{k,AMFC}$ is higher than $\eta_{k,PEMFC}$ due to lower charge transfer coefficient. The ohmic loss due to ionic resistance of membrane and catalyst layer is also relatively lower compared to PEMFC

(not shown here), nonetheless it is significant only at higher currents and hence it is not an urgent issue. Another severe limitation is from water transport at the cathode which causes the performance to drop even at low over potential. Practically though, while operating AMFC the back transport of water from anode to cathode at medium to higher overpotential helps in improving the performance to some extent. Hence the two most important limiting factors in the present AMFC performance are low rate of ORR and low mass transport of water.

It may be possible to operate AMFC in self balance mode where the water back transport from anode is able to sustain the cathodic reaction. However the diffusion of water through Tokuyama membrane is significant only when water is present in liquid form at anode CL and control of AMFC performance at these conditions may be challenging due to flooding. Therefore best control of AMFC performance is expected when the water required for cathodic reaction and electro osmotic drag is directly supplied to cathode via cathodic inlet gas. To achieve this, AMFC may be operated at high temperature so that fully humidified gas contains more water concentration, although it requires a durable membrane which is stable at high temperature. Another way to improve AMFC performance is to increase the channel width. Hence as the operating temperature of AMFC increases, its performance is likely to come closer to PEMFC performance at least in medium to high overpotential region. Nonetheless, the AMFC performance is never expected to go higher than PEMFC at any temperature and operating conditions unless the catalyst used in AMFC has higher electro-activity than the catalyst used in PEMFC. Therefore the key to obtain higher AMFC performance is to employ a catalyst with higher ORR activity than the state of art catalyst and somehow keep the membrane hydrated with as much water as possible without creating flooding at the anode side.

Finally, the results obtained in this Thesis work can also be applied to Alkaline Direct Methanol Fuel cells. As it is shown in Chapter 3 there is significant flux of water from anode to cathode when anode is flooded with water equivalent to limiting current of $\sim 3.4\ A \cdot cm^{-2}$. Therefore in case of Alkaline Direct Methanol Fuel cells mass transport limitation of water at cathode is unlikely to cause any problem. At low overpotential the rate of ORR might get affected with methanol crossover, yet at medium to high overpotential the ORR kinetics parameters determined in this thesis and rate expression developed in this thesis may be applied.

References

[1] J. O. Bockris, A. K. Reddy and M. Gamboa-Aldeco, Modern Electrochemistry 2B; Electrodics in Chemistry, Engineering, Biology and Environmental Science, Second ed., vol. 2B, New York: Kluwer Academics/ Plenum Publishers, 2000, p. 1794.

[2] G. E. Evans and K. V. Kordesch, "Hydrazine-Air Fuel Cells," vol. 158, pp. 1148-1152, 1967.

[3] E. H. Yu, U. Krewer and K. Scott, "Principles and Materials Aspects of Direct AlkalineAlcohol Fuel Cells," *Energies,* vol. 3, pp. 1499-1528, 2010.

[4] E. H. Yu, X. Wang, U. Krewer, L. Li and K. Scott, "Direct oxidation alkaline fuel cells: from materials to systems," *Energy Environ. Sci,* vol. 5, p. 5668, 2012.

[5] G. F. Mc Lean, S. Prince-Richard and N. Djilali, "An assessment of alkaline fuel cell technology," *International Journal of Hydrogen Energy,* vol. 27, pp. 507-526, 2002.

[6] J. Brain, J. Kalinoski and K. Baum, 24 September 2008. [Online]. Available: http://energy.gov/sites/prod/files/2014/03/f11/dti_fc_cost_analysis_dfma.pdf. [Accessed 29 July 2014].

[7] G. Merle, M. Wessling and K. Nijmeijer, "Anion exchange membranes for alkaline fuel cells: A review," *Journal of Membrane Science,* vol. 377, pp. 1-35, 2011.

[8] A. J. Bard and L. R. Faulkner, Electrochemical Methods; Fundamentals and Applications, second ed., New York, 2001, p. 143.

[9] T. V. Karman, "Über laminare und turbulente Reibung," *Journla of Applied Mathematics and Mechanics,* vol. 1, no. 4, pp. 233-252, 1921.

[10] G. W. Cochran, "The flow due to a rotating disc," *Mathematical Proceedings of the Cambridge Philisophical Society,* vol. 30, no. 3, pp. 365-375, 1934.

[11] V. G. Levich, Physicochemical Hydrodynamics, Englewood Cliffs, New Jersey: Prentice-Hall, 1962.

[12] J. Koutecky and V. G. Levich, *Zh. Fiz. Khim,* vol. 32, p. 1565, 1956.

[13] D. A. Gough and J. K. Leypoldt, "Membrane-Covered, Rotated Disc Electrode," *Anal. Chem.,* vol. 51, pp. 439-444, 1979.

[14] K. B. Prater and A. J. Bard, *J. Electrochem. Soc.,* vol. 117, p. 207, 1970.

[15] R. E. Davis, G. L. Horvath and C. W. Tobias, "The solubility and diffusion coefficient of oxygen in pottasium hydroxide solutions," *Electrochimica Acta,* vol. 12, pp. 287-297, 1967.

[16] A. Filpi, M. Boccia and H. A. Gasteiger, "Pt-Free Cathode Catalyst Performance in H2/O2 Anion-Exchange Membrane Fuel cells (AMFCs)," *ECS Trans.,* vol. 16, no. 2, pp. 1835-1845, 2008.

[17] K. Fukuta and H. Yanagi, "Anion Exchange Membrane and Ionomer for Alkaline Membrane Fuel Cells (AMFCs)," *ECS Trans.,* vol. 16, no. 2, pp. 257-262, 2008.

[18] Y. Wu, C. Wu, J. R. Varcoe, S. D. Poynton, T. Xu and Y. Fu, "Novel silica/poly(2,6-dimethyl-1,4-phenylene oxide) hybrid anion-exchange membranes foralkaline fuel cells: effect of silica content and the single cell performance," *Journal of Power Sources,* vol. 195, pp. 3069-3076, 2010.

[19] J. R. Varcoe and R. C. Slade, "An electron-beam-grafted ETFE alkaline anion exchange membrane in metal-cation-free solid-state alkaline fuel cells,," *Electrochemistry Communications,* vol. 8, pp. 839-843, 2006.

[20] M. Aleskar, M. Page, M. Shviro, Y. Paska, G. Gershinsky, D. R. Dekel and D. Zitoun, "Palladium/nickel bifunctional electrocatalyst for hydrogen oxidation reaction in alkaline membrane fuel cell," *J. Power Sources 304 (2016),* vol. 304, pp. 332-339, 2016.

[21] M. Piana, M. Boccia, A. Filpi, E. Flammia, H. Miller and M. Orsini, "H2/air alkaline membrane fuel cell performance and durability, using novel ionomer and non-platinum groupmetal cathode catalyst," *J Power Sources,* vol. 195, pp. 5875-5881, 2010.

[22] Y. Luo, J. Guo, C. Wang and D. Chu, "Fuel cell durability enhancement by crosslinking alkaline anion exchange membrane electrolyte," *Electrochem. Comm.,* vol. 16, pp. 65-68, 2012.

[23] S. Gottesfeld, 2011. [Online]. Available: http://www1.eere.energy.gov/hydrogenandfuelcells/pdfs/amfc_050811_gottesfeld_cellera.pdf. [Accessed 11 June 2015].

[24] S. Lu, J. Pan, A. Huang, L. Zhuang and J. Lu, "Alkaline polymer electrolyte fuel cells completely free from noble metal catalysts," in *Proceedings of the National Academy of Sciences of the United States of America*, 2008.

[25] P. S. Khadke and U. Krewer, "Performance losses at H2/O2 alkaline membrane fuel cell," *Electrochem. Comm.,* vol. 51, pp. 117-120, 2015.

[26] Y. Wan, B. Peppley, K. Creber, V. T. Bui and E. Halliop, "Preliminary evaluation of an alkaline chitosan-based membrane fuel cell," *Journal of Power Sources,* vol. 162, pp. 105-113, 2006.

[27] S. D. Poynton, J. P. Kizewski, R. C. Slade and J. R. Varcoe, "Novel electrolyte membranes and non-Pt catalysts for low temperature fuel cells," *Solid State Ionic,* vol. 181, p. 219–222, 2010.

[28] Y. Luo, J. Guo, C. Wang and D. Chu, "Quaternized poly(methyl methacrylate-co-butyl acrylate-co-vinylbenzyl chloride) membrane for alkaline fuel cells,," *Journal of Power Sources,* vol. 195, pp. 3765-3771, 2010.

[29] Y. Wan, B. Peppley, K. A. Creber, V. T. Bui and E. Halliop, "Quaternized-chitosan membranes for possible applications in alkaline fuel cells," *Journal of Power Sources,* vol. 185, pp. 183-187, 2008.

[30] J. Pan, S. Lu, Y. Li, A. Huang, L. Zhuang and J. Lu, "High-performance alkaline polymer electrolyte for fuel cell applications," *Advanced Functional Materials,* p. 312–319, 2010.

[31] J. S. Park, S. H. Park, S. D. Yim, Y. G. Yoon, W. Y. Lee and C. S. Kim, "Performance of solid alkaline fuel cells employing anion-exchange membranes," *J. Power Sources,* vol. 178, p. 620−626., 2008.

[32] T. E. Springer, M. S. Wilson and S. Gottesfeld, "Modeling and Experimental Diagnostics in Polymer Electrolyte Fuel Cells," *J. Electrochem. Soc.,* vol. 140, pp. 3513-3526, 1993.

[33] J. Ihonen, F. Jaouen, G. Lindbergh, A. Lundblad and G. Sundholm, "Investigation of mass-transport limitations in the solid polymer fuel cell cathode: II experimental," *J. Electrochem. Soc.,* vol. 149, pp. A448-A447, 2002.

[34] W. He and T. Nguyen, "Edge Effects on reference electrode measurements in PEM fuel cells," *J. Electrochem. Soc.,* vol. 151, pp. A185-A195, 2004.

[35] Z. Liu, J. S. Wainright, W. Huang and R. F. Savinell, "Positioning the reference electrode in proton exchange membrane fuel cells: calculations of primary and secondary current distribution," *Electrochim. Acta,* vol. 49, pp. 923-935, 2004.

[36] R. Zeng, S. D. Poynton, J. P. Kizewski, R. C. Slade and J. R. Varcoe, "A novel reference electrode for application in alkaline polymer electrolyte membrane fuel cells," *Electrochem. Comm.,* vol. 12, no. 6, pp. 823-825, 2010.

[37] W. Sheng, H. A. Gasteiger and Y. Shao-Horn, "Hydrogen Oxidation and evolution reaction kinetics on platinum: Acid vs Alkaline electrolytes," *J. Electrochem. Soc.,* vol. 157, pp. B1529-B1536, 2010.

[38] N. Ramaswamy and S. Mukerjee, "Fundamental Mechanistic Understanding of Electrocatalysis of Oxygen Reduction on Pt and Non-Pt Surfaces: Acid versus Alkaline Media," *Adv. Phys. Chem.,* vol. 2012, p. 1−17., 2012.

[39] L. Genies, R. Faure and R. Durand, "Electrochemical Reduction of Oxygen on Platinum Nanoparticles in Alkaline Media," *Electrochim. Acta 1998,* vol. 44, pp. 1317-1327, 1998.

[40] C. Weinzierl and U. Krewer, "Model-based analysis of water management in alkaline direct methanol fuel cells," *J. Power Sources,* vol. 268, pp. 911-921, 2014.

[41] A. J. Bard and L. R. Faulkner, Electrochemical methods: Fundamentals and applications, Second ed., John Wiley & Sons, Inc., 2001, pp. 52-53.

[42] J. A. Butler, "Studies in heterogeneous equilibria. Part II.—The kinetic interpretation of the nernst theory of electromotive force," *Trans. Faraday Soc.,* vol. 19, p. 729, 1924.

[43] T. G. Erdey and M. Volmer, *Z. Physikal Chemie,* vol. 203, p. 250, 1930.

[44] J. O. Bockris, A. K. Reddy and M. Gamboa-Aldeco, Modern Electrocheistry 2A; Fundamentals of Eltrodics, Second ed., vol. 2A, New York: Kluwer Academics / Plenum Publishers, 2000, pp. 1176-1187.

[45] A. J. Bard and L. R. Faulkner, Electrochemical methods: Fundamentals and applications, 2nd ed., John Wiley & Sons, Inc., 2001, p. 143.

[46] F. G. Cottrell, *Z. Physik. Chem.,* vol. 42, p. 385, 1902.

[47] A. J. Bard and L. R. Faulkner, Electrochemical methods: Fundamentals and applications, 2nd ed., John Wiley & Sons, Inc., 2001, pp. 166-168.

[48] A. J. Bard and L. R. Faulkner, Electrochemical methods: Fundamentals and applications, second ed., John Wiley & Sons, Inc., 2001, p. 163.

[49] J. O. Bockris, A. K. Reddy and M. Gamboa-Aldeco, Modern Electrocheistry 2A; Fundamentals of Electrodics, second ed., vol. 2A, New York: Kluwer Academics / Plenum Publishers, 2000, pp. 1427-1428.

[50] S. Trasatti and O. A. Petri, "Real surface area measurements in electrochemistry," vol. 63, no. 5, pp. 711-734, 1991.

[51] P. S. Khadke and U. Krewer, "Mass-Transport Characteristics of Oxygen at Pt/Anion Exchange Ionomer Interface," *J. Phys. Chem. C,* vol. 118, pp. 11215-11223, 2014.

[52] Y. Garsany, O. A. Baturina, K. E. Swider-Lyons and S. S. Kocha, "Experimental methods for quantifying the activity of platinum electrocatalysts for the oxygen reduction reaction," *Anal. Chem.,* vol. 82, p. 6321, 2010.

[53] H. A. Gasteiger, S. S. Kocha, S. Sompalli and F. T. Wagner, "Activity Benchmarks and Requirements for Pt, Pt-Alloys, and Non-Pt Oxygen Reduction Catalysts for PEMFCs," *Appl. Catal. B: Env.,* vol. 56, pp. 9-35, 2005.

[54] T. J. Schmidt, H. A. Gasteiger, G. D. Stäb, P. M. Urban, D. M. Kolb and R. J. Behm, "Characterization of High-Surface-Area Electrocatalysts Using a Rotating Disk Electrode Configuration," *J. Electrochem. Soc.,* vol. 145, no. 7, pp. 2354-2358, 1998.

[55] N. M. Markovic, H. A. Gasteiger and P. N. Ross, "Oxygen reduction on platinum low-index single-crystal surface in alklaine solution: Rotating ring disk studies," *J. Phys. Chem.,* vol. 100, pp. 6715-6721, 1996.

[56] D. M. Kolb, J. Lipkowski and P. N. Ross, Structure of Electricfied Interfaces, New York: VCH, 1993.

[57] K. J. Mayrhofer, G. K. Wiberg and M. Arenz, "Impact of Glass Corrosion on the Electrocatalysis on Pt Electrodes in Alkaline Electrolyte," *J. Electrochem. Soc. ,* vol. 155, pp. P1-P5, 2008.

[58] K. J. Mayrhofer, A. S. Crampton, K. H. Wiberg and M. Arenz, "Analysis of the Impact of Individual Glass Constituents on Electrocatalysis on Pt Electrodes in Alkaline Solution," *J. Electrochem. Soc.,* vol. 155, pp. P78-P81, 2008.

[59] R. Subbaraman, N. Danilovic, P. P. Lopes, D. Tripkovic, D. Strmcnik and V. R. Stamenkovic, "Origin of Anomalous Activities for Electrocatalysts in Alkaline Electrolytes," *J. Phys. Chem. C,* vol. 116, p. 22231−22237, 2012.

[60] S. D. James, "The Electrochemical Activation of Platinum Electrodes," *J. Electrochem. Soc,* vol. 114, pp. 1113-1119, 1967.

[61] A. J. Bard and L. R. Faulkner, Electrochemical methods: Fundamentals and applications, Second ed., John Wiley & Sons, Inc., 2001, p. 569.

[62] A. Botti, F. Bruni, S. Imberti, M. A. Ricci and A. K. Soper, "Solvation shell of OH- ions in water," *Journal of Molecular Liquids,* vol. 117, pp. 81-84, 2005.

[63] T. Yamanaka, T. Takeguchi, H. Takahashi and W. Ueda, "Water transport during ion conduction in anion-exchange and cation-exchange membranes," *J. Electrochem. Soc.,* vol. 156, pp. 831-835, 2009.

[64] J. M. LaManna and S. G. Kandlikar, "Determination of effective water vapor diffusion coefficient in pemfc gas diffusion layers," *International Journal of Hydrogen Energy,* vol. 36, pp. 1-9, 2011.

[65] T. R. Marrero and E. A. Mason, "Gaseous Diffsuion Coefficients," *J. Phys. Chem. Ref. Data,* vol. 1, pp. 3-118, 1972.

[66] W. J. Massman, "A Review of the Molecular Diffusivities of H2O, CO2, CH4, CO, O3, SO2, NH3, N2O, NO and NO2 in air, O2 and N2 near STP," *Atmospheric Environment ,* vol. 32, pp. 1111-1127, 1998.

[67] J. A. Schetz and A. E. Fuhs, "Fundamentals of Fluid Mechanics," Third ed., J. A. Schetz and A. E. Fuhs, Eds., Wiley-Interscience, 1999, p. 203.

[68] A. E. Kharouf, T. J. Mason, D. J. Brett and B. G. Pollet, "Ex-situ characterisation of gas diffusion layers for proton exchange membrane fuel cells," *J. Power Sources,* vol. 218, pp. 393-404, 2012.

[69] K. T. Jeng, S. F. Lee, G. F. Tsai and C. H. Wang, "Oxygen mass transfer in PEM fuel cell gas diffusion layers," *J. Power Sources,* vol. 138, pp. 41-50, 2004.

[70] W. Sun, B. A. Peppley and K. Karan, "Modeling the influence of GDL and flow-field plate parameters on the reaction distribution in the PEMFC cathode catalyst layer," *J. Power Sources,* vol. 144, pp. 42-53, 2005.

[71] X. D. Wang, X. X. Zhang, W. M. Yan, D. J. Lee and A. Su, "Determination of the optimal active area for proton exchange membrane fuel cells with parallel, interdigitated or serpentine designs," *International Journal of Hydrogen Energy,* vol. 34, pp. 3823-3832, 2009.

[72] X. D. Wang, Y. Y. Duan and W. M. Yan, "Numerical study of cell performance and local transport phenomena in PEM fuel cells with various flow channel area ratios," vol. 172, pp. 265-277, 2007.

[73] Q. Zhao, P. Majsztrik and J. Benziger, "Diffusion and Interfacial Transport of Water in Nafion," *J. Phys. Chem. B,* vol. 115, p. 2717–2727, 2011.

[74] D. R. Lawson, L. U. Whiteley, C. R. Martin, M. N. Szentirmay and J. I. Song, "Oxygen Reduction at Nafion® Film-coated Platinum Electrodes: Transport and Kinetics," *J. Electrochem. Soc,* vol. 135, pp. 2247-2253, 1988.

[75] A. Parthasarathy, S. Srinivasan and A. Appelby, "Pressure Dependence of the Oxygen Reduction Reaction at the Platinum Microelectrode/Nafion Interface − Electrode Kinetics and Mass Transport," *J. Electrochem. Soc.,* vol. 139, pp. 2856-2862, 1992.

[76] A. Parthasarathy, S. Srinivasan, A. J. Appleby and C. R. Martin, "Temperature Dependence of the Electrode Kinetics of Oxygen Reduction at the Platinum/Nafion Interface - A Microelectrode Investigation.," *J. Electrochem. Soc,* vol. 139, pp. 2530-2537, 1992.

[77] A. Parthasarthy and C. R. Martin, "Investigations of the O2 reduction reaction at the Platinum/Nafion Interface using a solid-state electrochemical cell," *J. Electrochem. Soc.,* vol. 138, pp. 916-921, 1991.

[78] T. Lehtinin, G. Sundholm, S. Holmberg, S. Sundholm, P. Bjornbom and M. Bursell, "Electrochemical Characterization of PVDF Based Proton Conducting Membranes for Fuel Cells," *Electrochim. Acta,* vol. 43, pp. 1881-1890, 1998.

[79] Z. Ogumi, Z. Takehara and S. Yoshizawa, "Oxygen permeation through nafion and neosepta," *J. Electrochem. Soc.,* vol. 131, pp. 769-773, 1984.

[80] L. Zhang, C. Ma and S. Mukerjee, "Oxygen permeation studies on the alternative proton exchange membranes designed for elevated temperature operation," *Electrochem. Acta,* vol. 48, pp. 1845-1859, 2003.

[81] Y. Takamura, E. Nakashima, H. Yamada, A. Tasaka and M. Inaba, "Effects of Temperature and Relative Humidity on Oxygen Permeation in Nafion and Sulfonated Poly(Arylene Ether Sulfone)," *ECS Trans.,* vol. 16, pp. 881-889, 2008.

[82] A. T. Haug and R. E. White, "Oxygen Diffusion Coefficient and Solubility in a New Proton Exchange Membrane," *J. Electrochem. Soc.,* vol. 147, pp. 980-983, 2000.

[83] I. Gunasekara, M. Lee, D. Abbott and S. Mukerjee, "Mass Transport and Oxygen Reduction Kinetics at An Anion Exchange Membrane Interface: Microelectrode Studies on Effect of Carbonate Exchange," *ECS Electrochemistry Letters,* vol. 1, pp. F16-F19, 2012.

[84] L. Jiang, A. Hsu, D. Chu and R. Chen, "Oxygen Reduction Reaction on Carbon Supported Pt and Pd in Alkaline Solutions," *J. Electrochem. Soc.,* vol. 156, pp. B370-B376, 2009.

[85] R. J. Taylor and A. A. Humffray, "Electrochemical Studies on Glassy Carbon Electrodes: II. Oxygen Reduction in Solutions of High pH (pH > 10)," *J. Electroanal. Chem.,* vol. 64, pp. 63-84, 1975.

[86] K. Vaik, U. Maeorg, F. C. Maschion, G. Maia, D. J. Schiffrin and K. Tammeveski, "Electrocatalytic Oxygen Reduction on Glassy Carbon Grafted with Aanthraquinone by Anodic Oxidation of a Carboxylate Substituent," *Electrochim. Acta,* vol. 50, pp. 5126-5131, 2005.

[87] E. Yeager, "Dioxygen electrocatalysis: mechanism in relation to catalyst structure," *J. Mol. Catal.,* vol. 38, pp. 5-25, 1986.

[88] C. Song and J. Zhang, "Electrocatalytic Oxygen Reduction Reaction," in *PEM Fuel Cell Electrocatalysts and Catalyst Layers*, J. Zhang, Ed., London, Springer London, 2008, pp. 89-134.

[89] V. B. Baez and D. Pletcher, "Preparation and characterization of carbon/titanium dioxide surfaces — the reduction of oxygen," *J. Electroanal. Chem.,* vol. 382, pp. 59-64, 1995.

[90] C. P. Winlove, K. H. Parker and R. K. Oxenham, "The measurement of oxygen diffusivity and concentration by chronoamperometry using microelectrodes," *J. Electroanal. Chem. Interfacial Electrochem.,* vol. 170, pp. 293-304, 1984.

[91] J. P. Pamela and A. J. Bard, "Polymer films on electrodes Part II. Film structure and mechanism of electron transfer with electrodeposited poly(vinylferrocene)," *J. Electroanal. Chem.,,* vol. 112, pp. 97-115, 1980.

[92] R. S. Yeo and J. McBreen, "Transport Properties of Nafion Membranes in Electrochemically Regenerative Hydrogen/Halogen Cells," *J. Electrochem. Soc.,* vol. 126, pp. 1682-1687, 1979.

[93] K. E. Gubbins and R. D. Walker, "The solubility and diffusivity of oxygen in electrolytic solutions," *J. Electrochem. Soc.,* vol. 112, pp. 469-471, 1965.

[94] K. J. Mayrhofer, D. Strmcnik, B. B. Blizanac, V. Stamenkovic, M. Arenz and N. M. Markovic, "Measurement of oxygen reduction activities via rotating disc electrode method: Fom Pt model surfaces to carbon-supported high surface area catalysts," *Electrochim. Acta,*

vol. 53, pp. 3181-3188, 2008.

[95] T. Gueshi, K. Tokuda and H. Matsuda, "Voltammetry at partially covered electrodes: Part I. Chronopotentiometry and chronoamperometry at model electrodes," *J. Electroanal. Chem.,* vol. 247, pp. 247-260, 1978.

[96] A. Caprani, C. Deslouis, S. Robin and B. Tribollet, "Transient mass transfer at partially blocked electrodes: A way to charecterize topography," *J. Electroanal. Chem.,* vol. 238, pp. 67-91, 1987.

[97] S. S. Kocha, "Principles of MEA preparation," in *Handbook of Fuel cells - Fundamentals technlogy and applications*, vol. 3, Chichester, Wiley, 2003, p. 538.

[98] T. R. Ralph, G. A. Hards, J. E. Keating, S. A. Campbell, D. P. Wilkinson, M. Davis, J. St-Pierre and M. C. Johnson, "Low Cost Electrodes for Proton Exchange Membrane Fuel Cells: Performance in Single Cells and Ballard Stacks," *J. Electrochem. Soc.,* vol. 144, p. 3485, 1997.

[99] A. N. Frumkin, "Über die Beeinflussung der Adsorption von Neutralmolekülen durch ein elektrisches Feld," *Z. Physik.,* vol. 35, pp. 792-802, 1926.

[100] M. I. Temkin, "Kinetics of heterogeneous catalysis," *J. Phys. Chem. (U. S. S. R.) ,* vol. 14, p. 1153, 1940.

[101] M. I. Temkin, "Adsorption equilibrium on heterogeneous surfaces," *J. Phys. Chem. (U.S.S.R.),* vol. 20, p. 1441, 1946.

[102] A. J. Bard and L. R. Falukner, Electrochemical methods: Fundamentals and applications, Second ed., John Wiley & Sons, Inc., 2001, pp. 566-567.

[103] H. Li, Y. Tang, Z. Wang, Z. Shia, S. Wu, D. Song, J. Zhang, K. Fatih, J. Zhang and H. Wang, "A review of water flooding issues in the proton exchange membrane fuel cell," *J. Power Sources,* vol. 178, pp. 103-117, 2008.

[104] H. Zhang, H. Ohashi, T. Tamaki and T. Yamaguchi, "Water Movement in a Solid-State Alkaline Fuel Cell Affected by the Anion-Exchange Pore-Filling Membrane Properties," *J.*

Phys. Chem. C 2013, vol. 117, pp. 16791-16801, 2013.

[105] K. Matsumoto, T. Fujigaya, H. Yanagi and N. Nakashima, "Very High Performance Alkali Anion-Exchange Membrane Fuel Cells," *Adv. Funct. Mater.,* vol. 21, pp. 1089-1094, 2011.

[106] J. R. Varcoe, R. C. Slade, G. L. Wright and Y. Chen, "Steady-State dc and Impedance Investigations of H2/O2 Alkaline Membrane Fuel Cells with Commercial Pt/C, Ag/C, and Au/C," *J. Phys. Chem. B,* vol. 110, pp. 21041-21049, 2006.

[107] C. Boyer, S. Gamburzev, O. Velev, S. Srinivasan and A. J. Appleby, "Measurements of proton conductivity in the active layer of PEM fuel cell gas diffusion electrodes," *Electrochimica Acta,* vol. 43, pp. 3703-3709, 1998.

[108] T. A. Zawodzinski, C. Derouin Jr., S. Radzinski, R. J. Sherman, V. T. Smith, T. E. Springer and S. Gottesfeld, "Water Uptake by and Transport Through Nation | 117 Membranes," *J. Electrochem. Soc.,* vol. 140, pp. 1041-1047, 1993.

[109] T. A. Zawodzinski Jr., M. Neeman, L. O. Sillerud and S. Gottesfeld, "Determination of water diffusion coefficients in perfluorosulfonate ionomeric membranes," *J. Phys. Chem.,* vol. 95, pp. 6040-6044, 1991.